

Final Technical Report

Project Title: Manufacturing of Low Cost, Durable Membrane Electrode Assemblies Engineered for Rapid Conditioning

Report Number: DOE-GORE-18052

Date of Report: 5/23/2017

Dates of Project: 9/1/2008 – 6/30/2015

Recipient: W.L. Gore & Associates, Inc.

Award Number: DE-FC36-08GO18052

Working Partners: W.L. Gore & Associates, Inc., University of Delaware, University of Tennessee at Knoxville

Cost-Sharing Partners: W.L. Gore & Associates, Inc., University of Delaware, University of Tennessee at Knoxville

Contacts:

PI: F. Colin Busby, 410-506-7773, cbusby@wlgore.com

Business Contact: Laura Keough, 410-506-7546, lkeough@wlgore.com

DOE Managers: DOE HQ Technology Manager: Nancy Garland, DOE Field Project Officer: Jesse Adams

Contents

Executive Summary	2
Project Objectives	3
Tasks and Results	3
Phase 1	3
Task 1: Characterization of Existing Process and Product	3
Task 2: Model Development	10
Task 3: Equipment Procurement and Qualification	11
Phase 2	12
Section 1	12
Section 2	47
Section 3	76
Conclusions	116
References	117
Appendix A: Publications and Patent Applications	119
Appendix B: SA's 2016 Re-evaluation of Gore Direct-Coated MEA Fabrication	120

Executive Summary

Over the past 20 years significant progress in membrane-electrode assembly (MEA) technology development for polymer electrolyte fuel cells (PEMFCs) has resulted in the PEMFC technology approaching a commercial reality for transportation applications. However, there remain two primary technical challenges to be addressed in the MEA. First and foremost is meeting the automotive cost targets: Producing a fuel cell stack cost competitive with today's internal combustion engine. In addition to the material cost, MEA (and other components) and stack assembly production methods must be amenable for use in low cost, high speed, automotive assembly line. One impediment to this latter goal is that stack components must currently go through a long and tedious conditioning procedure before they produce optimal power. This so-called "break-in" can take many hours, and can involve quite complex voltage, temperature and/or pressure steps. These break-in procedures must be simplified and the time required reduced if fuel cells are to become a viable automotive engine. The second challenge is to achieve the durability targets in real-world automotive duty cycle operations.

Significant improvements in cost, break-in time, and durability for the key component of fuel cell stacks, MEAs were achieved in this project. Advanced modeling was used to guide design of the new MEA to maximize performance and durability. A new, innovative process and manufacturing approach utilizing direct in-line coating using scalable, cost-competitive, continuous high volume 3-layer rolled-good manufacturing processes was developed and validated by single cell and short stack testing. In addition, the direct coating methods employed were shown to reduce the cost for sacrificial films. Furthermore, Gore has demonstrated a 10 μm reinforced membrane that is used in the new low-cost process and can meet automotive power density and durability targets. Across a wide range of operating conditions, the direct-coated MEA outperformed the commercial baseline MEA, and did so through a process that delivers MEAs at \$92.35/m² at a volume of 500,000 systems per year, according to Strategic Analysis (SA) estimates.

Note:

This report was prepared as an account of work sponsored by an agency of the United States Government. Neither the United States Government nor any agency thereof, nor any of their employees, makes any warranty, express or implied, or assumes any legal liability or responsibility for the accuracy, completeness, or usefulness of any information, apparatus, product, or process disclosed, or represents that its use would not infringe privately owned rights. Reference herein to any specific commercial product, process, or service by trade name, trademark, manufacturer, or otherwise does not necessarily constitute or imply its endorsement, recommendation, or favoring by the United States Government or any agency thereof. The views and opinions of authors expressed herein do not necessarily state or reflect those of the United States Government or any agency thereof.

Project Objectives

The objective of this program is to evaluate unique, high volume manufacturing processes that will produce low-cost, durable, high power density MEAs that require little or no stack conditioning. The manufacturing processes will be scalable to fuel cell industry MEA volumes in 2015 (estimate 100,000 m² / year), and will be consistent with achieving the 2010 DOE automotive stack cost target of \$25 / kW_e. The product made in the manufacturing process should be at least as durable as the MEA made in the current process (as per protocols referenced in task 1.1) and should demonstrate power density greater or equal to that of the MEA made by the current process (as per protocol referenced in task 1.1). The stack break-in time should be reduced to 4 hours or less, and the break-in strategies employed must be consistent with achieving high volume manufacturing cost targets.

TASKS AND RESULTS

Phase 1

Task 1: Characterization of Existing Process and Product

Characterize Break-In And Performance Testing Of The MEA Made In The Current Commercial Manufacturing Process.

MEA performance was characterized in fuel cell performance tests designed to be relevant to the DOE automotive targets, which is consistent with DOE's primary focus of developing fuel cells for transportation applications. This portion of evaluation is limited to Gore's baseline commercial MEA technology using preexisting Gore MEA manufacturing process.

- MEA power density was characterized in fuel cell performance tests that were designed to be relevant to a variety of fuel cell applications (see Figure 1). Polarization curves were generated using the following operating conditions:

Condition	Description	Tcell (C)	Inlet RH (Anode/Cathode)	Stoich (Anode/Cathode)	Pressure (psig)
1	Stationary	80	100/100%	1.3 H2/2.0 Air	0
2	Wet	70	152/152%	1.3 H2/2.0 Air	0
3	Current Auto	80	33/33%	1.3 H2/2.0 Air	7
4	Future Auto	95	19/19%	1.3 H2/2.0 Air	7

RH – relative humidity

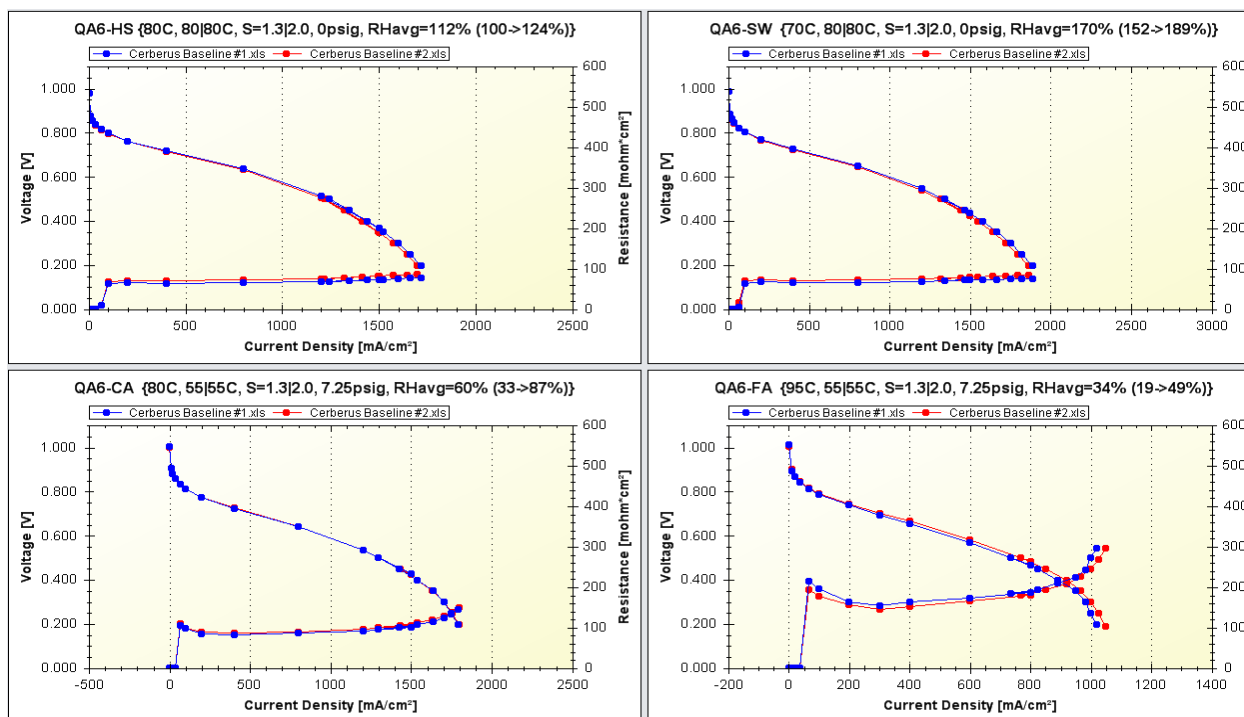


Figure 1. Power Density Characterization of the MEA Made in the Current Commercial Process

- Break-in was characterized using the following protocol. Gore's current commercial MEAs achieved break-in within 2 hours of cycling.

Tcell (C)	Pressure (psig)	Inlet (Anode/Cathode)	Stoich (Anode/Cathode)
80	25	100/100%	1.2 H ₂ /2.0 Air

Step cycle between 0.6V, open-circuit voltage (OCV), 0.3V, OCV, 0.6V, OCV, etc. for 2 hours.

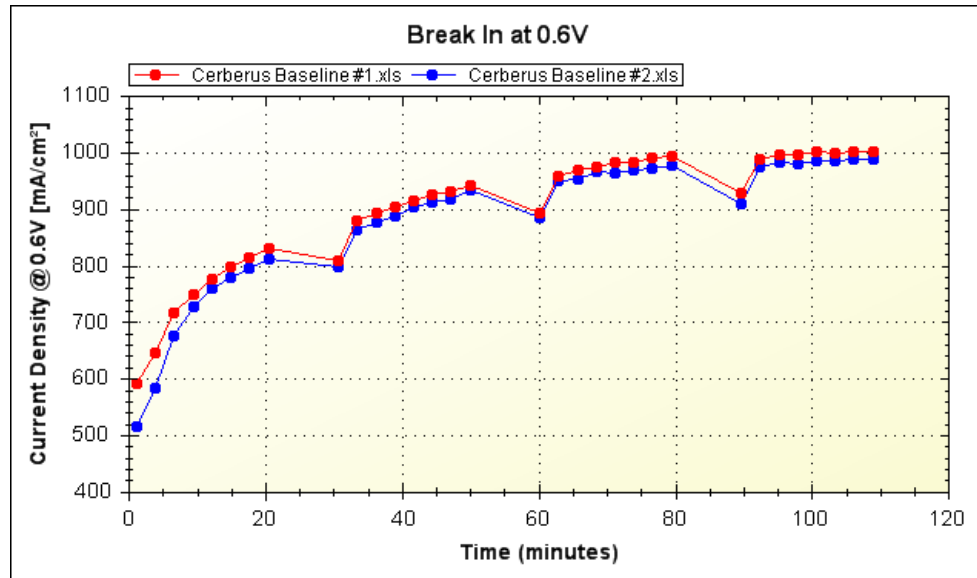


Figure 2. Break-in Characterization of the MEA Made in the Current Commercial Process

- Replicate Gore MEAs exceeded 2,000 hours of single-cell accelerated mechanical durability testing using the cycle given below, which has been equated to achieving 9,000 hours of membrane durability in an 80°C automotive duty cycle. This result exceeds the DOE 2015 membrane durability target of 5,000 hours.

Tcell (C)	Pressure (kPa)	Flow (Anode/Cathode, cc/min)
80	270	500 N2/1,000 N2

Cycle between dry feed gas and humidified feed gas
(sparger bottle temp = 94°C)
Dry feed gas hold time: 15 seconds
Humidified feed gas hold time: 5 seconds

For further protocol information, see: W. Liu, M. Crum, ECS Transactions **3**, 531-540 (2007).

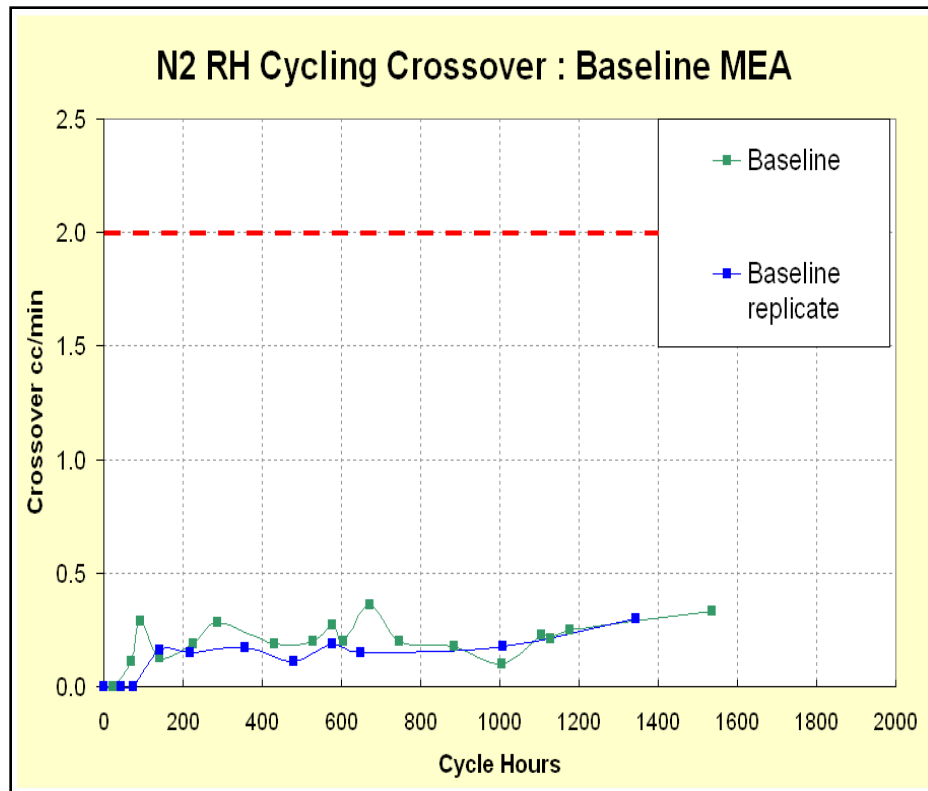


Figure 3. Mechanical Durability Characterization of the MEA Made in the Current Commercial Process

- Chemical durability (in OCV hold testing) was characterized using the protocol given below. After 300 hours of testing, replicate Gore MEAs maintained low degradation as evidenced by fluoride release rates under $5.18 \times 10^{-8} \text{ g F/hr cm}^2$ using CNW10A gas diffusion media (GDM) on the W1 protocol listed below.

Tcell (C)	I (mA cm ²)	Inlet (Anode/Cathode)	RH	Pressure (kPa)	Flow (Anode/Cathode, cc/min)
95	0	50/50%		270	100/200 cc/min

For further protocol information, see: W. Liu, M. Crum, ECS Transactions **3**, 541-550 (2007).

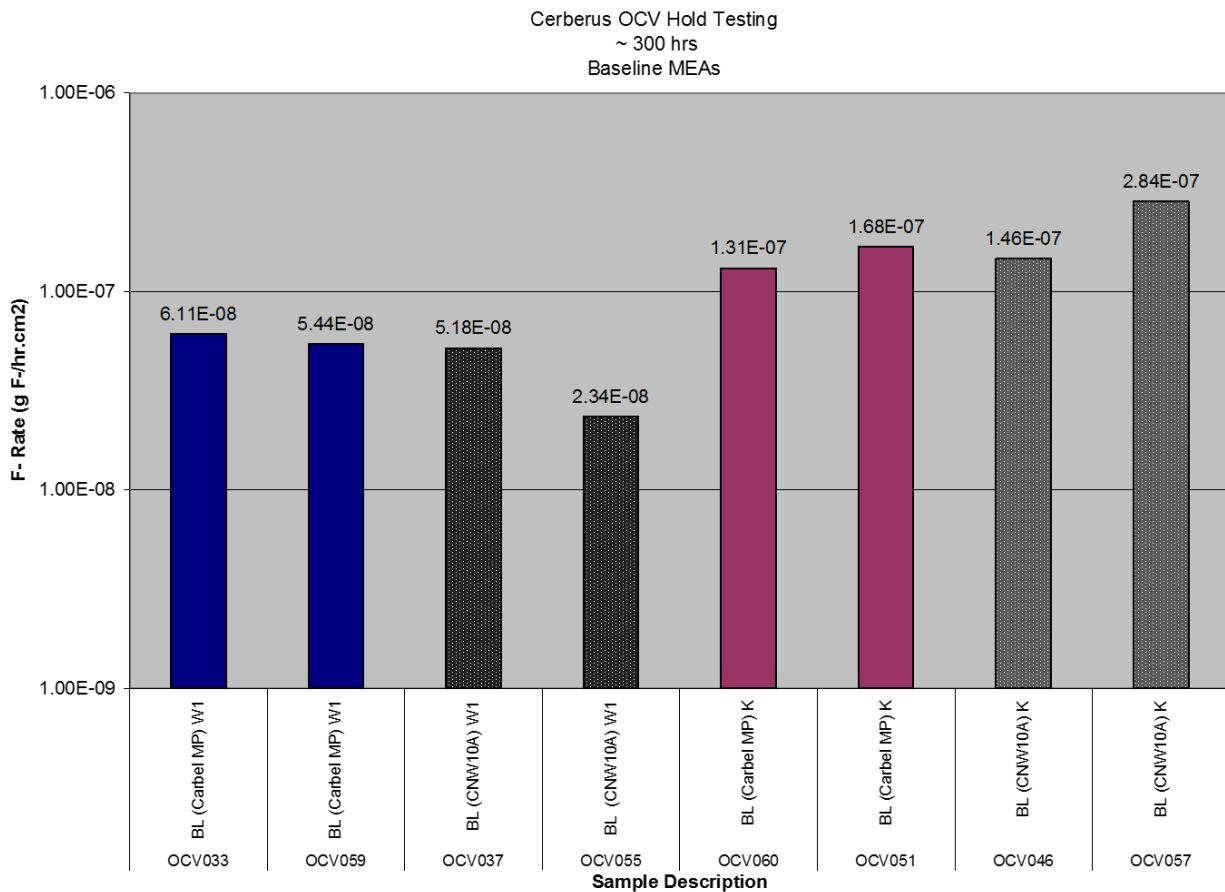


Figure 4. Chemical Durability Characterization of the MEA Made in the Current Commercial Process

Cost Modeling of the MEA Made In The Current Commercial MEA Manufacturing Process

Key inputs for the cost model were determined. Many of the input assumptions were aligned with the 2005 TIAx NREL Subcontractor report NREL/SR-560-39104.

GORE		
Category	Inputs	Description
Catalyst	900	Pt cost (\$ per Troy Ounce)
	20%	Catalyst process markup
	34.72	Processed Pt cost (\$ per gram)
	0.40	Total loading (mg Pt/cm ²)
	92%	Pt reclaim value from scrap
Ionomer	80	Ionomer cost (\$/lb)
Coating	2.31	Membrane 2 pass coating process cost (\$ per m ²)
	3.47	Combined anode & cathode coating process cost (\$ per m ² of CCM)

**Sales
Volume**

323	AA per cell (cm ²)
85	% utilization of CCM
231	cells per stack
2	stacks per vehicle
17.56	CCM per vehicle (m ²)
500,000	vehicles per year
8,778,000	CCM production per year (m ²)

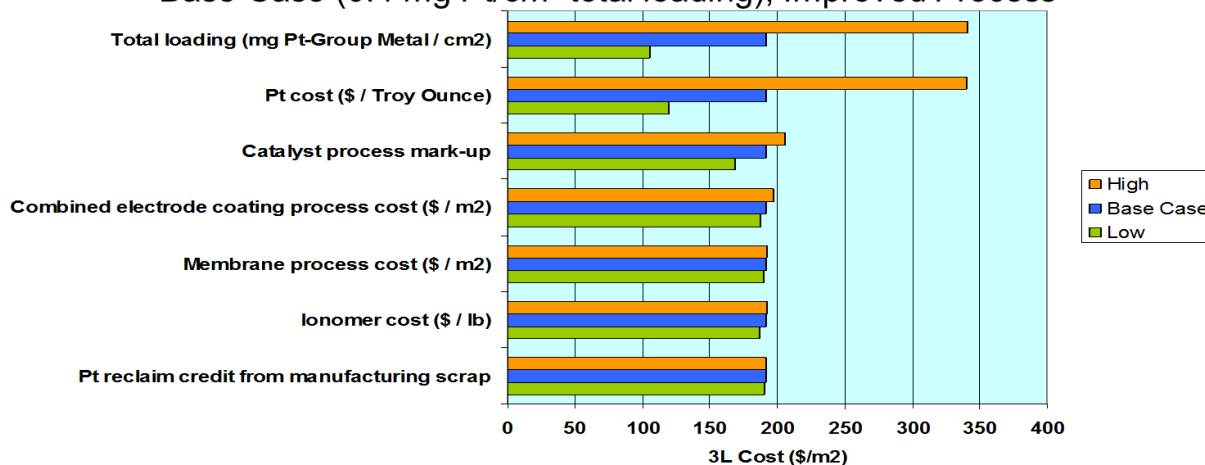
A Process Waste Map was created to identify potential cost reductions and selected improvements were used to develop the cost model. Model results indicate that a 17% reduction in the cost of the high volume base case 3-layer MEA is attainable given the potential process improvements within the scope of this project. See Figure 5 for process waste map and key improved process assumptions. In addition, sensitivity analysis was executed to evaluate which components of the MEA and which processes could have the most significant impact on the overall MEA cost.

Process Waste Map

Membrane Coating		
Process Costs	Primary forms of waste	Modeled Process Improvements
Ionomer solution	line losses, edge trim, membrane thickness	Membrane thickness reduction
ePTFE	edge trim, thread-up	
Backers	all backers	Reusable backer
Solvent/disposables	all	
Process/MOH	time	
DL	time	
Other		
Electrode Coating		
Process Costs	Primary forms of waste	Modeled Process Improvements
Catalyst	line losses, edge trim, electrode residuals	Reduce scrap with better coating process
Backers	all backers	No backers
Solvent/disposables	all	
Process/MOH	time	
DL	time	
Other		
3 Layer Roll-Good Finishing Operations		
Process Costs	Primary forms of waste	Modeled Process Improvements
Electrodes	edge trim	Eliminate this process
Membrane	edge trim	Eliminate this process
Process/MOH	time	Eliminate this process
DL	time	Eliminate this process
		These were included in the improved process cost model

Figure 5. 3-Layer MEA Manufacturing Process Waste Map

Single-Variable Sensitivity Analysis Base Case (0.4 mg Pt/cm² total loading), Improved Process



Key Input Assumptions and Justification

Category	Description	Base Case	Sensitivity Range	Sensitivity notes
Catalyst	Pt cost (\$ / Troy Ounce)	1100	640 - 2060	Min: mean real price ³ Max: 2008 monthly avg maximum ⁴
	Catalyst process mark-up	20%	5 - 30%	Based on Gore interactions with catalyst suppliers
	Total loading (mg Pt-Group Metal / cm²)	0.40	0.2 - 0.75	Min: DOE 2015 target ⁵ , table 3.4.12 Max: 2005 TIAX Report ² Table 14
	Pt reclaim credit from manufacturing scrap	95%	90 - 98%	Based on Gore interactions with catalyst suppliers
Ionomer	Ionomer cost (\$ / lb)	88	22 - 110	2005 TIAX Report ² Table 20 (\$20 - \$100/lb in 2005 dollars)
Coating	Membrane process cost (\$ / m²)	2.18	1.00 - 4.00	Gore assumption, MOH & DL only, adapted from TIAX methodology
	Combined electrode coating process cost (\$ / m²)	6.00	3.00 - 12.00	Gore assumption, MOH & DL only, adapted from TIAX methodology

References

- 2008 TIAX Tech Team Review "Direct Hydrogen PEMFC Manufacturing Cost Estimation for Automotive Applications" DE-AD36-06GO26044
- 2005 TIAX Report "Cost Analysis of PEM Fuel Cell Systems for Transportation" NREL/SR-560-39104
- 2004 TIAX "Platinum Availability and Economics for PEMFC Commercialization" DE-FC04-01AL67601
- http://www.platinum.matthey.com/prices/price_charts.html
- http://www1.eere.energy.gov/hydrogenandfuelcells/mypp/pdfs/fuel_cells.pdf

Task 2: Model Development

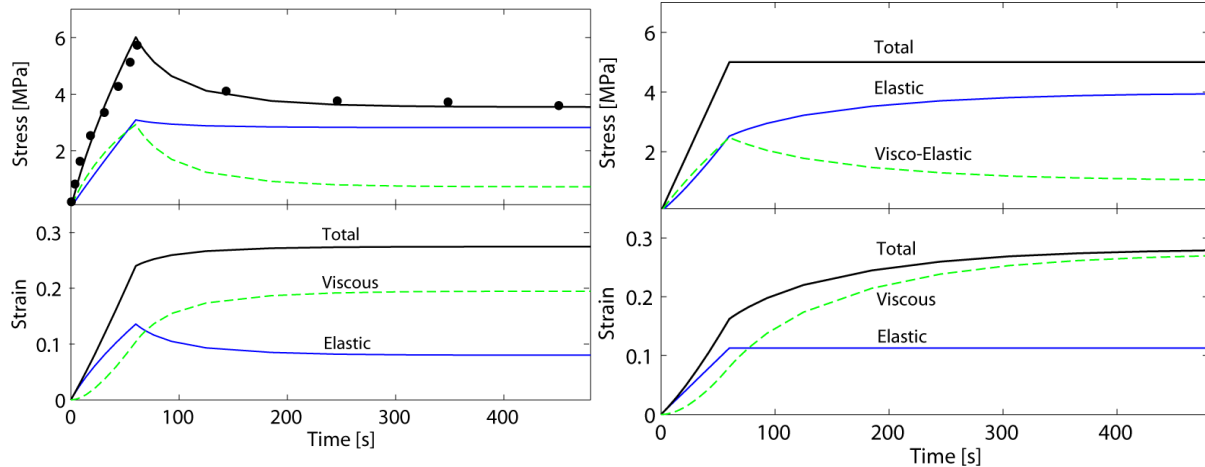
2.1 Mechanical Modeling

Possible paths for establishing time dependent mechanical properties were investigated.

Methods to characterize ionomer membrane visco-elastic and visco-plastic properties were investigated using a TMA (thermal mechanical analyzer) modified for humidity control. As a pilot investigation, small samples (1/8" diameter discs) of Nafion® 112 membrane were mounted onto the custom-built stage equilibrated within the test chamber at selected temperature humidity combinations (25°C and 30% RH; 50% and 90% RH). A 0.01 Newton preload was applied to hold the specimen flat on the loading stage while allowing 30 minutes for the sample and chamber to equilibrate. The sample was then loaded compressively with a 1 Newton load (corresponding to 0.125 MPa pressure) and held for 15 minutes before releasing the load. During this loading, three distinct phases of deformation were observed. During the application of the compressive load, the specimen thickness decreased rapidly, corresponding to an elastic stress-strain response. As the load was held, the specimen continued to compress, indicating a creep response. When the load was released, the specimen slowly began to regain thickness in a recovery response. For these pilot investigations, the load cycle was held constant. Full equilibrium and recovery were not realized at any stage in the test. Consequently, in future studies, an optimum load-time cycle will be established and used to collect the relevant time-dependent data.

Existing numerical model was extended to include time dependent (visco-elastic/plastic) properties.

The applicability of ABAQUS finite element modeling was investigated for simulating the time-dependent response of ionomer membrane by constructing a small axisymmetric model. Data from a previous study in which the University of Delaware conducted a preliminary investigation of time-dependent properties of Nafion® 112 membrane in a water environment. In the model, a load sequence corresponding to the sequence used in the experimental investigation (load-hold at constant displacement) was applied. The time-dependent deformation was calculated for this load sequence and compared to the experimental results (see Figure 6). The results show that a simple Maxwell model with nonlinear strain is adequate to capture the experimental response. This material model was later implemented in numerical simulations of stresses in fuel cell operation.



(A) (B)
 Figure 6. (A) Experiment conducted via loading and hold at constant strain. Markers indicate experimental values; solid black line indicates the deformation using a Maxwell model for viscoelastic response. (B) Using the extracted material parameters for the Maxwell model, the graphs show the predicted response for a case of loading followed by holding at constant force.

Task 3: Equipment Procurement and Qualification

Laboratory scale equipment with capabilities to achieve the cost reductions determined in Task 1.2 was researched, specified, and procured.

Task 4: Project Management and Reporting

- All project management and reporting obligations were fulfilled.

Phase 2

Section 1

Baseline Testing of the Current Commercial MEA to Understand Interactions with Different Gas Diffusion Layer (GDL) Properties

Performance and durability interactions between 3-layer MEA's and different gas diffusion layers have been known to exist. Interactions between the baseline MEA and critical GDL properties (hydrophobicity, in-plane permeability, through-plane permeability, porosity, and cost) in both the macro and micro layers provided valuable insight for prototype design and evaluation in Task 6.1. Direct coated electrodes were later paired with the best GDL materials to complement the water, heat, and gas transfer needs of the low cost MEA.

In this task, 7 microporous layer (MPL) materials with different thickness, hydrophobicity, thermal conductivity and pore morphology were extensively investigated *in-situ* and *ex-situ*. In *ex-situ* studies, their physical, chemical and thermal properties were characterized in detail. Each material was also tested *in-situ* using fuel cell test systems with an extended range of diagnostics. Both experimental and computational programs were completed.

Experimental Test Cell

A coolant controlled fuel cell built by Dynak, Inc., and designed by General Motors was selected for *in-situ* testing. (See Figures 1 and 2). It can be easily scaled up with a design allowing fuel/oxidant/coolant in and out at the two ends. In addition, there are 6 metallic tips for current/voltage collection in each flow field/bipolar plate. As shown in Figure 2, there are 22 parallel wavy channels at cathode (left part) and 11 parallel wavy channels (right part) at the anode, respectively. Between them, there is cross-section view of the flow field, which indicates the coolant channel locations. All the channels have a depth of 0.4 mm with a rectangular shape. At the cathode, the widths of channels and lands are 0.7 mm and 0.5 mm, respectively. At the anode side, both are 0.7 mm and 1.7 mm, respectively. The cell active area in this study is 50 cm² (2.5 cm in width x 20 cm in length), which was determined by the catalyst coated membranes (CCMs). In all experiments, hydrogen of ultra-high purity (>99.999%) from compressed gas cylinders and standard dry air or Heliox (21% oxygen with the balance made of helium (79%), Airgas, Inc.) were used.



Figure 7 Assembled fuel cell with an active area of 50 cm².

Net water transport across MEAs was measured based on the difference of accumulated water content in anode and cathode sides. The water contents on both sides was measured at the fuel cell outlets and before back pressure unit, as shown in Figure 8. Since these tests were run under both the historic standard and future automotive test conditions, and FA test condition incorporates a 50 kPa backpressure to the fuel cell, the setup was designed to collect water from

the exhaust with the expected magnitude of backpressure. Testing was initiated at steady state and concluded when enough water was collected to yield a statistically high signal to noise ratio. The three way valves, V1 and V2, as indicated in Figure 8, allows the system to bypass the water collection site until the moment that water measurement begins. The collection sites consist of a hollow, air tight, plastic cylinder filled with indicating Drierite to absorb water. On each of the outlets of the water collection sites is a one way valve to ensure Drierite collectors remain isolated until water management tests are to begin. Past the valve, the water collection sites' outlets reconnect to the bypass route which, in turn, leads to the backpressure unit. Between fuel cell and collector, the temperatures of all the pipelines were controlled to vaporize all the liquid water.

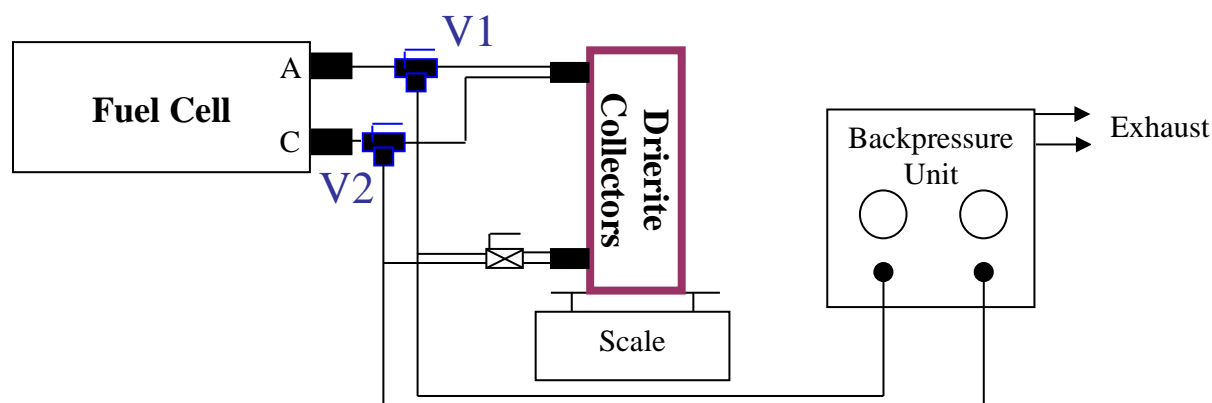


Figure 8: Test system schematic

A set of 7 MPL materials, along with standalone DM were characterized with a TM3000 Scanning Electron Microscope (SEM). Each sample was characterized with both top view and cross-section view images, which was shown in Figure 9 (A) and (B), respectively. The thickness of each sample and associated MPL, were derived from the cross-section view SEM images.

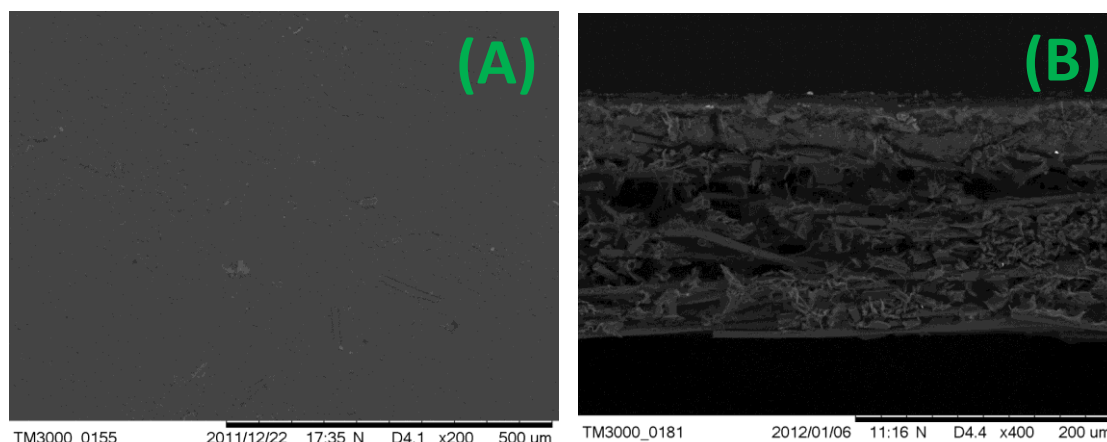


Figure 9 Typical results of SEM and EDSA characterization with MPL 40 100C.

All samples were measured with Thermal Analyzer TPS 2500 as shown in Figure 11. This device can be used to measure a film with a thickness of 20 μm to 600 μm and a range of thermal conductivity of 0.05 W/m K to 2 W/m K. The system was modified in-house by addition of a compression unit with a capacity of up to 2 MPa. The equipment and system were validated with polytetrafluoroethylene (PTFE) sheet and conventional DMs with good agreements between the results with the manufacture of the equipment. During the test, the loading pressure was set to a nominal value of 2.5 bar for all the measurements.

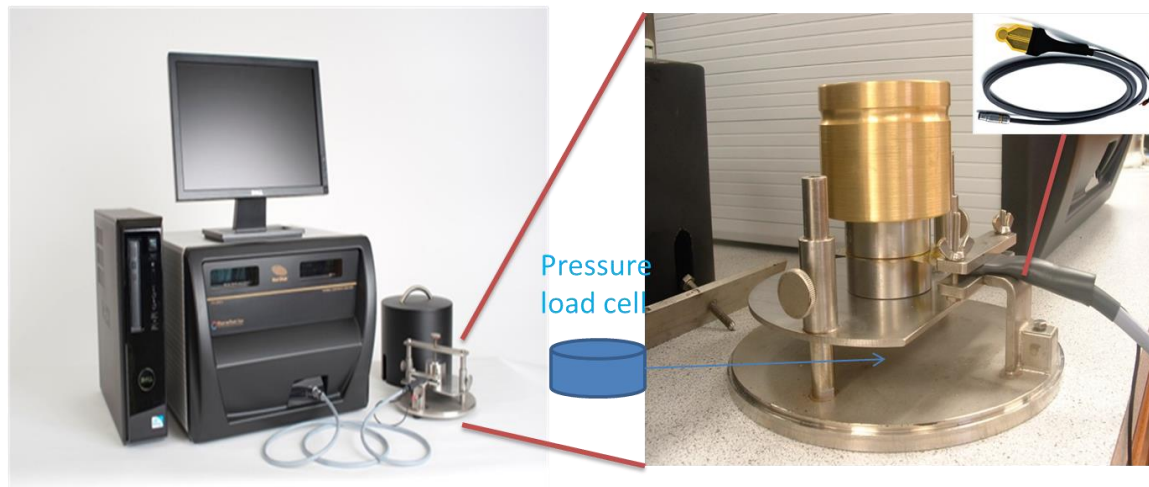


Figure 11 Thermal Analyzer TPS 2500

Fuel cell testing with MPL 100, assembled at 45 inch•lb, was repeated 3 times at all operating conditions for the HS, SW, CA and FA, and no significant changes in performance were observed. Figures 12 and 13 showed a typical repeatability result with error bars of both 5% of voltage and current density (CD) at HS and CA condition, respectively. The error rates of voltage were less than 2% at low current density range, and less than 5% even at higher current density range.

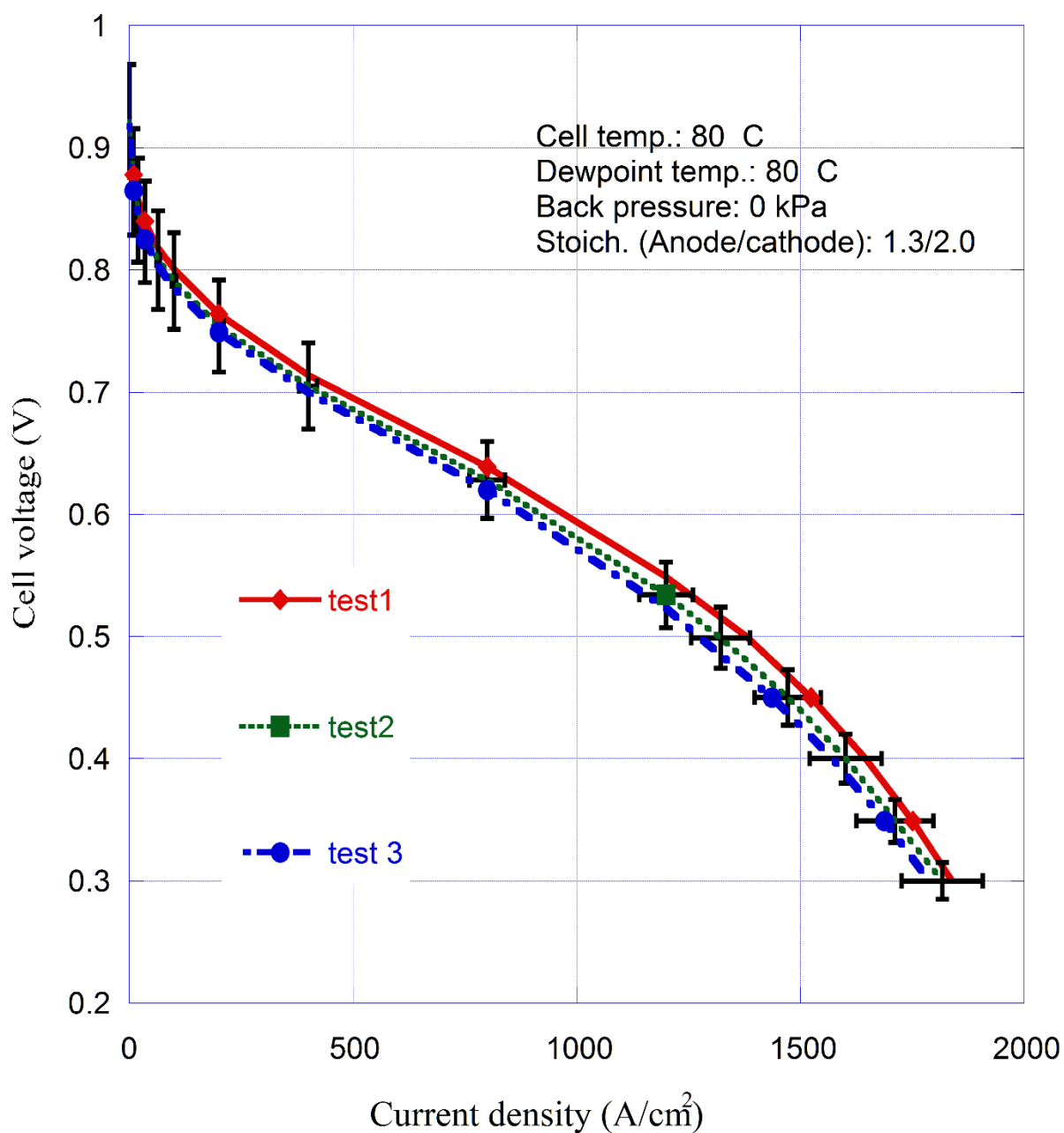


Figure 12 Test results at HS condition for repeatability.

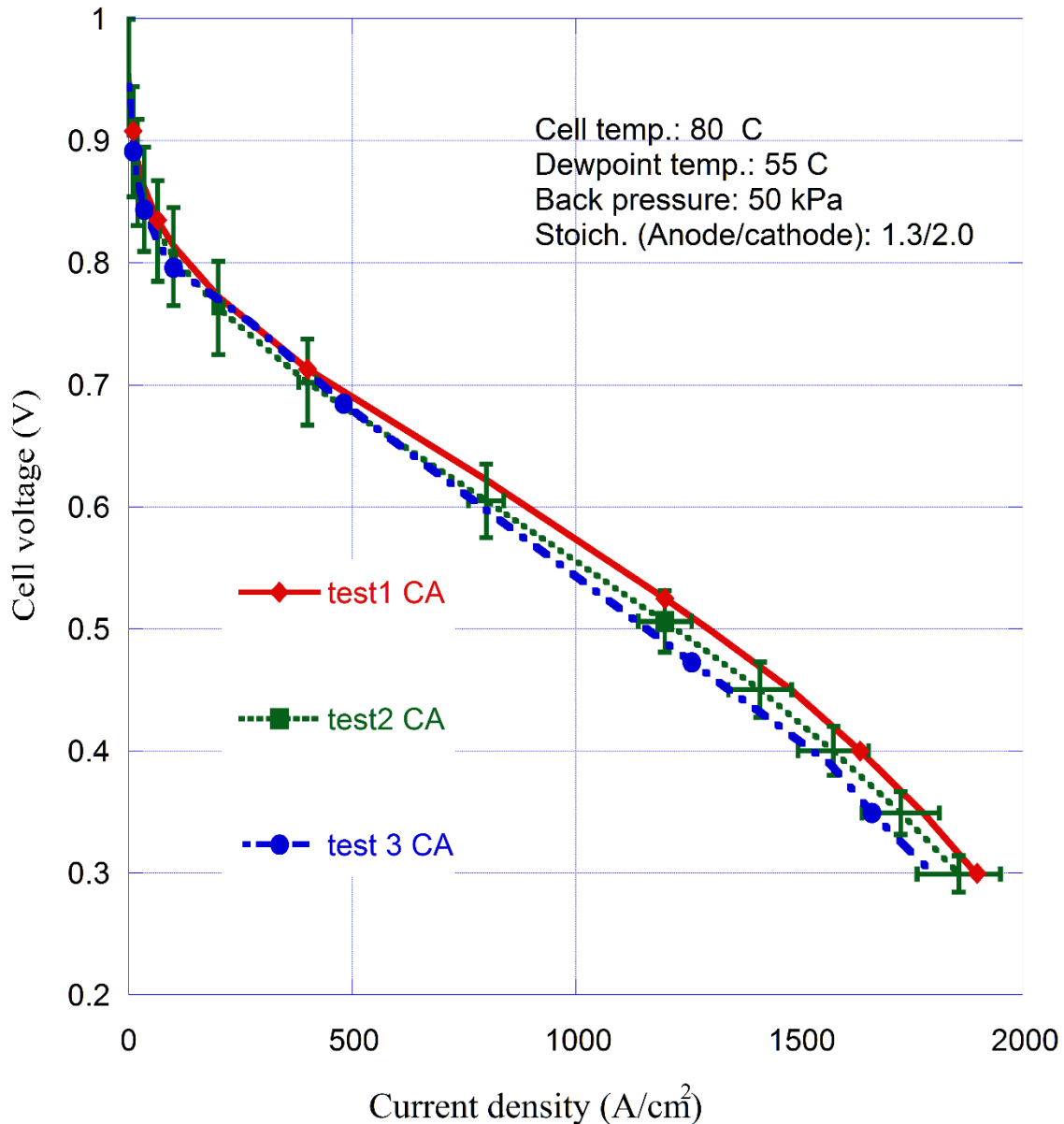


Figure 13 Test results at CA condition for repeatability.

All 7 MPL materials were tested in the fuel cell with an active area of 50 cm². The cell temperature was controlled at 80 °C with RH of 100% under 0 backpressure, and its anode/cathode stoichiometry was kept at 1.3/2.0. Figure 14 shows the fuel cell performance curves with different MPL materials at FA condition. It can be seen that there is virtually no difference between them at low current density range. And the performance difference is only observed at large current range, which is mainly due to transport limitation at wet condition. At wet condition, high permeability and hydrophobicity/ low thickness helps reduce flow resistance and concentration losses, thus improving the cell performance. This is also concluded from computational simulation results.

MPL 50 with the highest relative permeability, low thickness and reasonable thermal conductivity and hydrophobicity generally performed the best. MPL 100 has much lower permeability and higher thickness than MPL 50, which results in poorer performance, as suggested by model simulations as well. MPL 50 GK performed the worst due to its hydrophilic feature caused by the addition of some hydrophilic materials, as indicated in EDSA result. The hydrophilic materials result in local flooding, and hampered the fuel/oxidant transport and catalyst activity.

It should be noted that MPL 40/100C/C90 has the lowest relative permeability and highest thermal conductivity. And it also shows good performance. This might partially be due to its unique pore morphology and composition with highest carbon and lowest fluorine, as detailed in Table 5, which might benefit from the micro-scale pore distribution and higher saturation vapor pressure, which lowered local flooding in MPL and its interface with catalyst layer (CL).

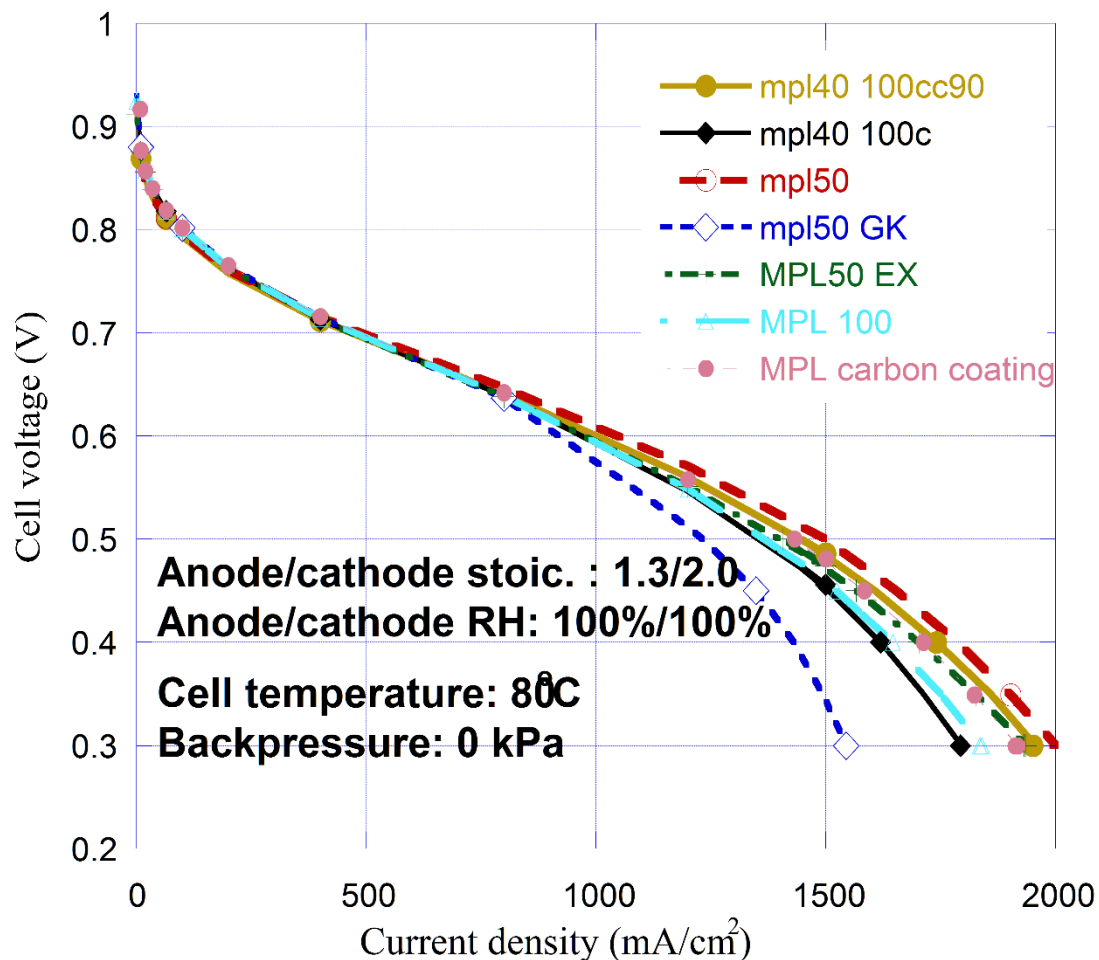


Figure 14 Fuel cell performances with different MPL materials at HS conditions.

All 7 MPL materials were also tested under superwet condition with a RH of 152% and similar performance difference between the MPL materials were found. Please note that the original proposal contained 6 materials, but an extra one was added to provide more complete data with the MPL carbon coating material. Their performances are better than ones at HS condition due to the large stoichiometry of 2.5/2.5 at both sides, which improved liquid water removal and H₂/Oxidizer concentration. Again, the 50GK performed the worst in wet conditions.

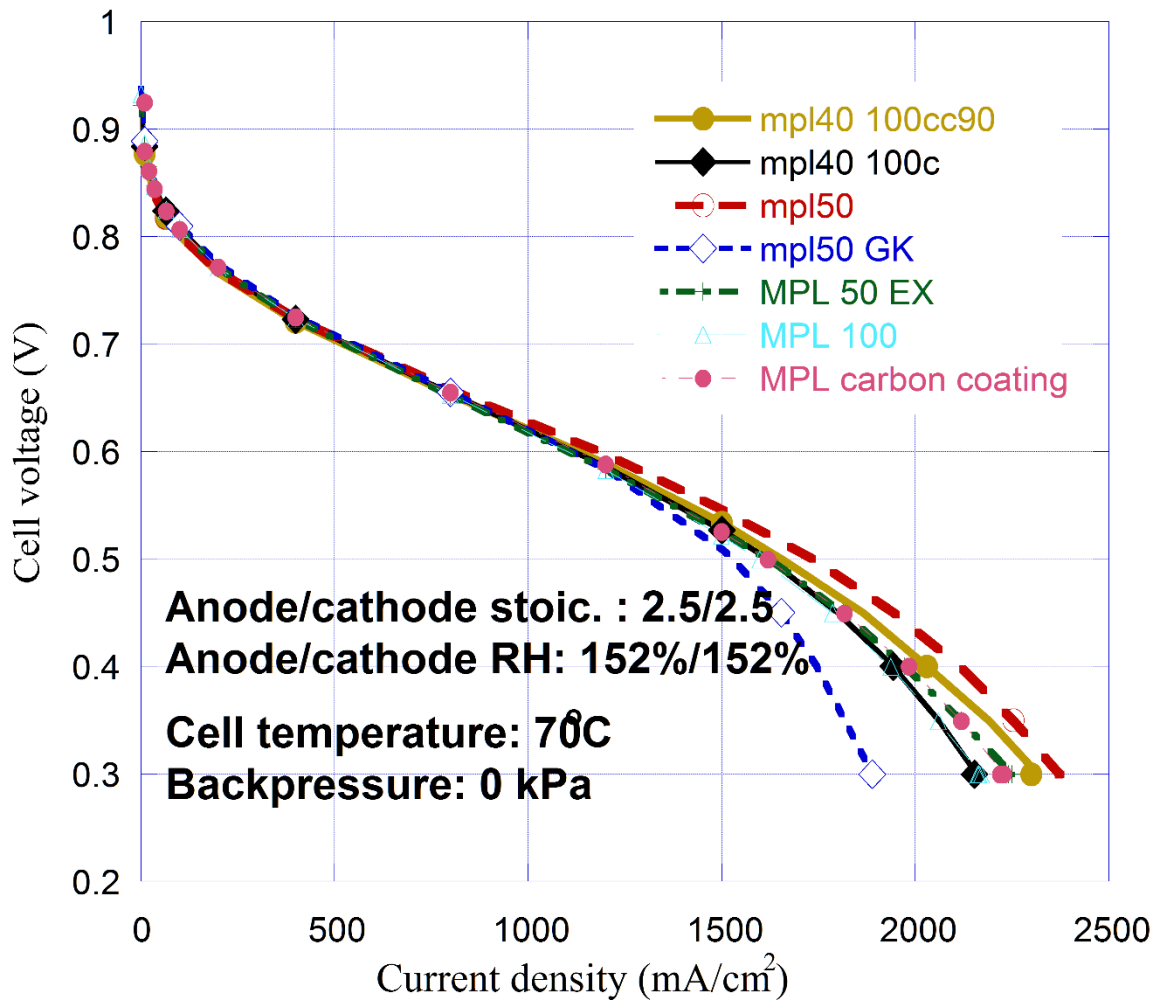


Figure 15 Fuel cell performances with different MPL materials at SW conditions.

The set of 7 MPL materials were also tested in the fuel cell with dry conditions of Current Automotive (CA) and Future Automotive (FA) under a back pressure of 50 KPa. At CA dry condition, the cell temperature was controlled at 80 °C with RH of 33%, while the RH is only about 19% at FA condition. Figure 16 shows the performance results of MPL materials at CA dry conditions. Differing from wet conditions, no big difference in all the ranges was found among MPLs, which indicates macro DM control of the thermal profile, as simulated computationally. At dry conditions, little liquid water were expected to be saturated in the diffusion media, including MPLs and DMS, thus the effects of mass transport resistance due to the flooding in diffusion media on fuel cell performances could be very minimal. The fuel cell performances are mainly dominated by their ohmic losses and the impact of evaporative losses which are controlled mainly from the macro DM thermal resistance as described in the computational section of this report.

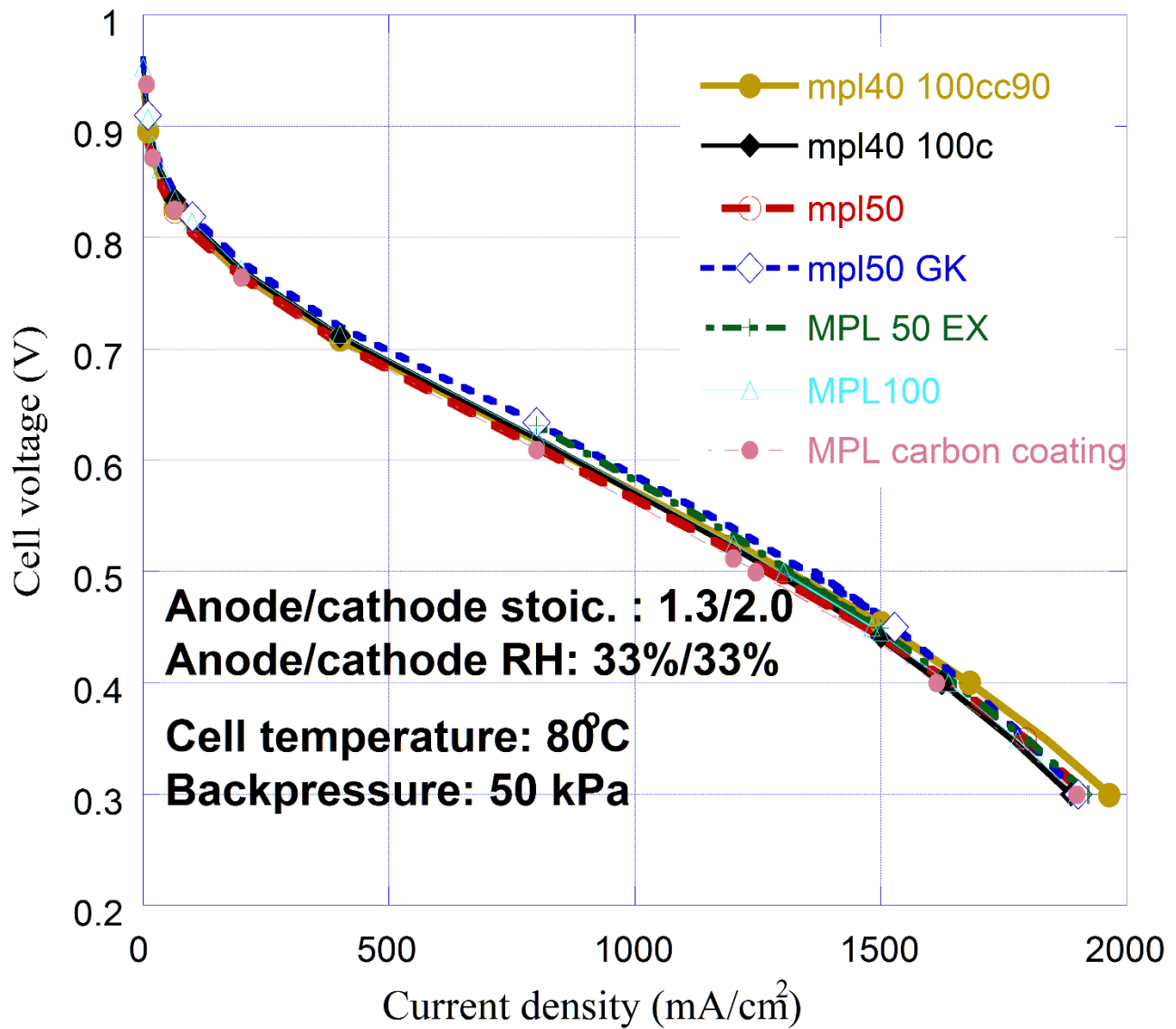


Figure 16 Fuel cell performances with different MPL materials at CA conditions.

Fuel Cell Performance at FA Condition

Similar to CA condition, no significant performance difference between the MPL materials were obtained in FA conditions. As shown in Figure 17, the fuel cell performance was significantly worse at super dry operating condition.

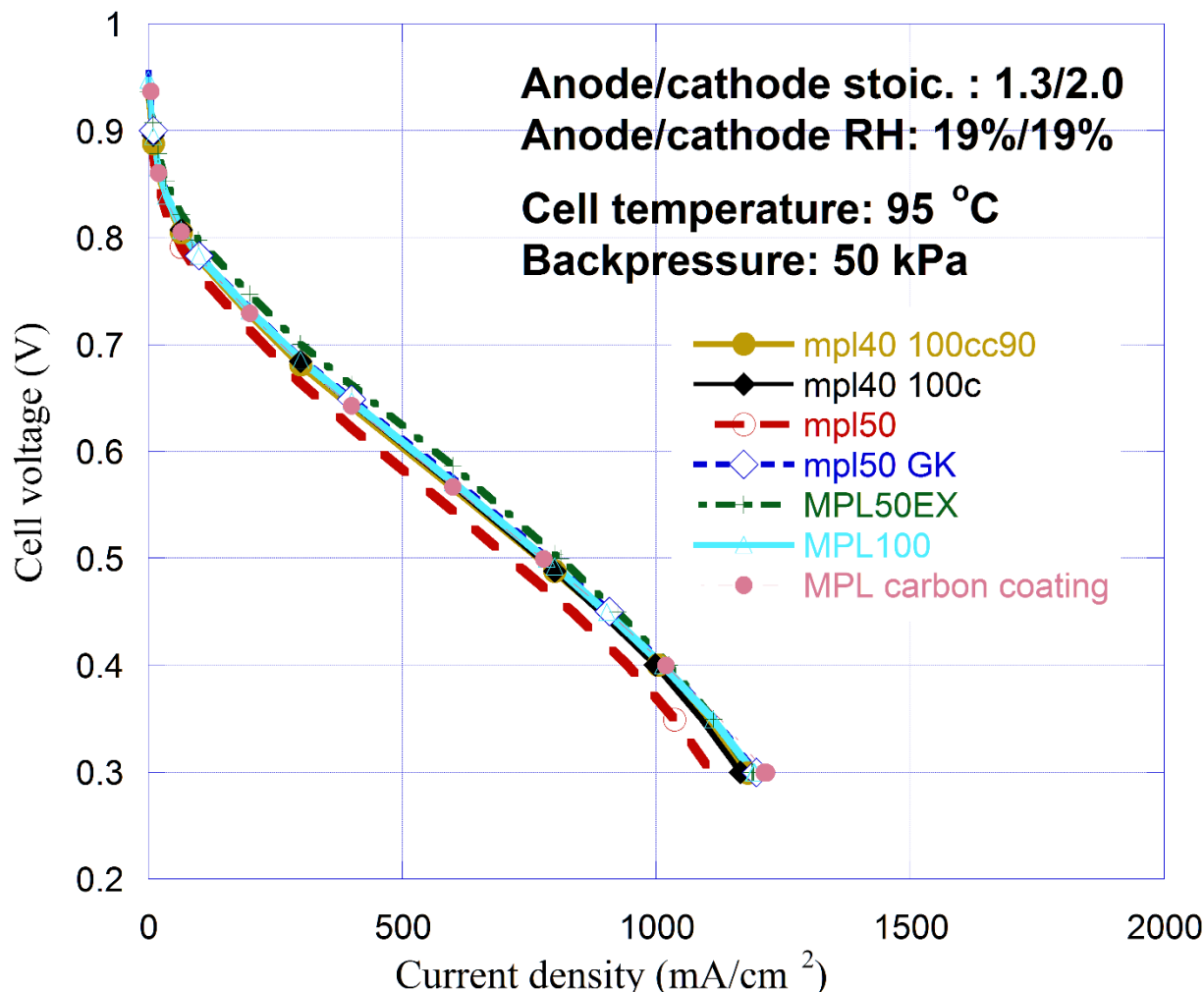


Figure 17 Fuel cell performances with different MPL materials at FA conditions.

Electrochemical Impedance Spectroscopy Investigation at Wet Conditions

For better understanding of the major loss effects on fuel cell performance, electrochemical impedance spectroscopy (EIS) was employed to provide in-depth characterization of the resistances. Figure 18 shows the Nyquist plots of all 7 MPLs with a fixed current density of 1.2 A/cm² at wet conditions. Over the whole frequency range from 1 Hz to 3000 Hz, only one depressed semi-arc was obtained in all the ac-impedance spectra, which showed three features: high-frequency resistance (HFR when >300 Hz), medium-frequency resistance (MFR at 300Hz ~ 12 Hz), and low-frequency resistance (LFR at <12 Hz).

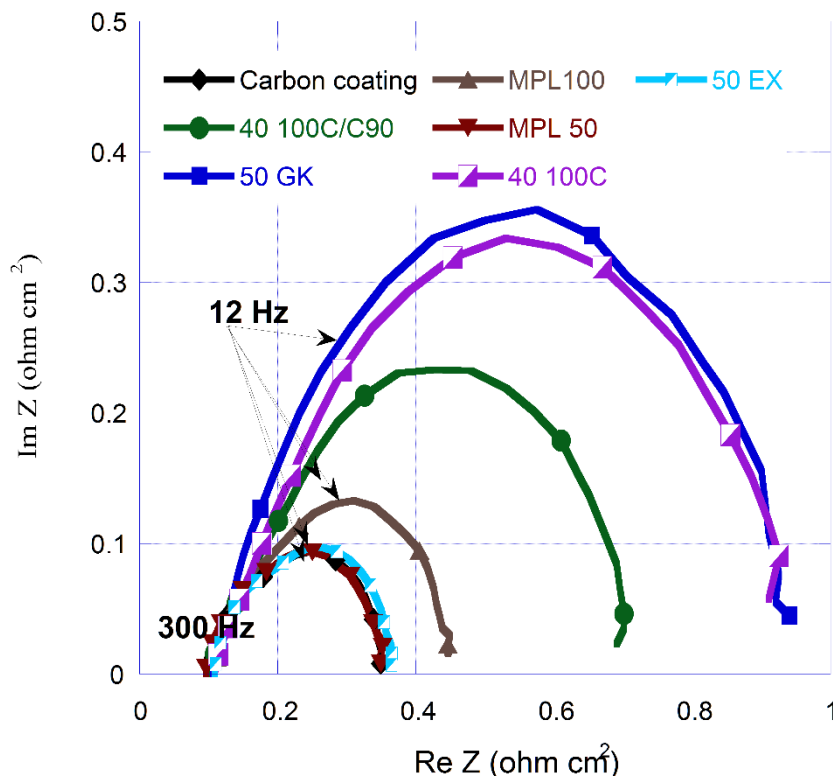


Figure 18 EIS results with air and heliox at wet condition (high frequency range: >300 Hz, middle frequency range: 300 Hz – 12 Hz; Low frequency range: 12 Hz – 1 Hz).

The intercept of the single depressed arc with the real axis at the high-frequency end is the high-frequency resistance (HFR), which mainly represents total ohmic resistance. It includes the ohmic resistances of all cell components, including bipolar plates, diffusion media, electrodes and membranes, and the associated interfacial resistances between them. The medium-frequency range (1000 Hz ~ 12 Hz) and low frequency range (<12 Hz) provided estimates of the charge-transfer resistances and the mass transport resistances, respectively. As shown in the figure, under the same operating conditions, HFRs hardly changed among MPL materials, while LFRs were greatly dependent on MPL properties. MPLs of carbon coating, 50 and 50 EX showed the smallest value, about $0.35 \Omega \bullet \text{cm}^2$, while MPLs of 50 GK and 40 100C gave the largest one, $0.93 \Omega \bullet \text{cm}^2$. The MPLs of 40 100C/C90 and MPL 100 were between them. Mass transport resistances were associated with many mechanisms, including oxidant concentration or diffusion rate reduction (such as oxygen, heliox, air), non-uniform current distribution on electrodes, and oxidant transport resistance caused by liquid water blockage in electrodes and/or diffusion media due to flooding. The different MPLs contributed to the flooding variations in MPLs, electrodes, and their interfaces, thus the changes of oxidant diffusion rate in the associated components. Thicker MPL (as MPL 100) increased the transport resistance of water flow from the cathode electrode to the DM substrate and flow channels due to its longer flow pathway. Less hydrophobic MPLs (as MPL 50 GK) resulted in much more flooding than other MPLs due to its more hydrophilic features, which showed the worst fuel cell performance among all 7 MPLs. Please note MPL 40 100C and 40 100C/C90 were very unique. They showed a relative larger LFRs, while with good performances. This may mainly be due to their unique pore distributions, which promote evaporation.

Electrochemical Impedance Spectroscopy Investigation at Dry Conditions

Differing from the EIS results at HS conditions, all of the ac-impedance spectra for all 7 materials at FA condition consisted of two separated arcs, which were separated at the frequency of 12 Hz, as shown in Figure 19. All 7 materials had similar HFRs, while LFRs depended on the MPL materials. MPL 50 GK gave the largest one, followed by MPL 40 100C. The rest of them showed similar values. Their ac-impedance spectra were almost overlapped. At FA condition, the fuel cell performances are mainly limited by the HFRs, as discussed before.

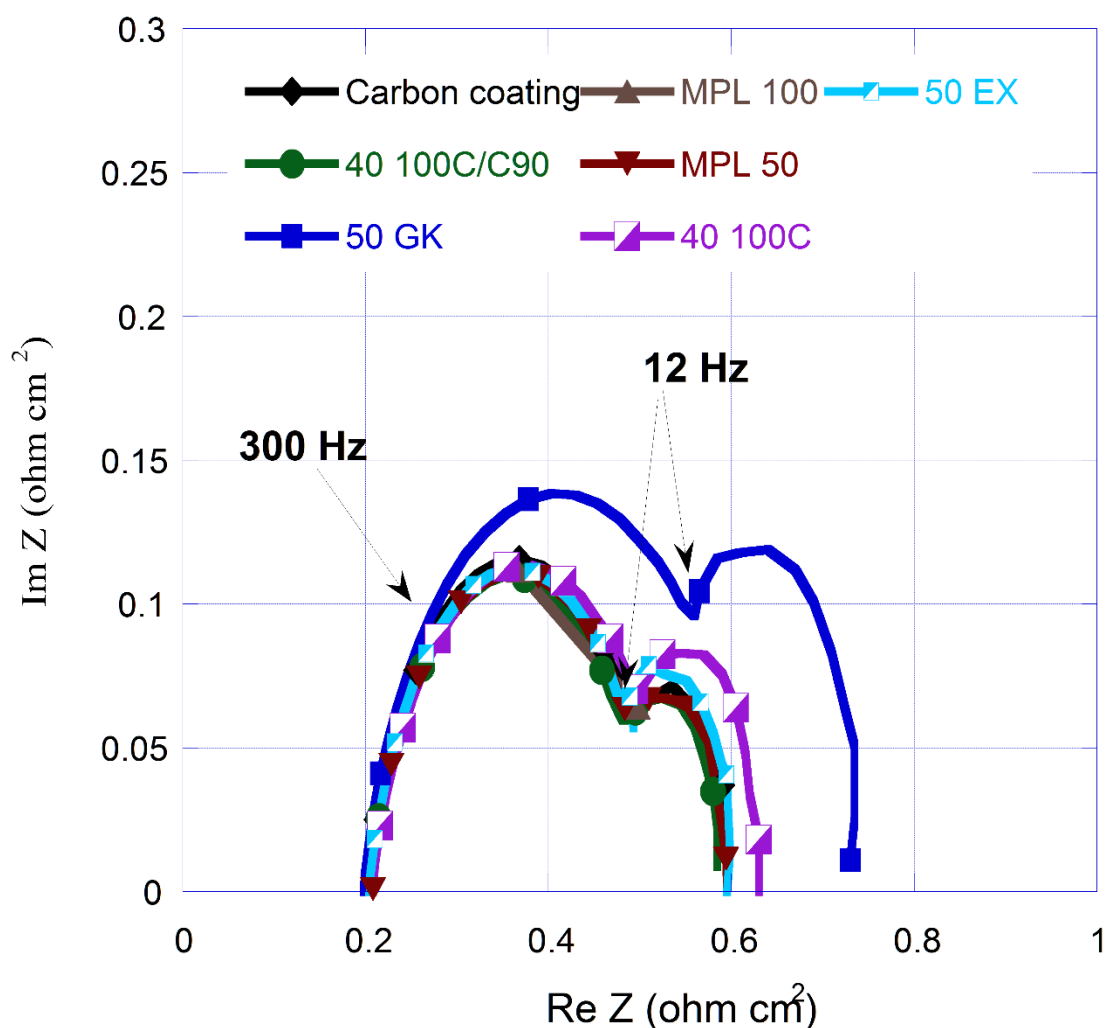


Figure 19 EIS results with air and heliox at FA condition (high frequency range: >300 Hz, middle frequency range: 300 Hz – 12 Hz; Low frequency range: 12 Hz – 1 Hz).

Effects of Flow Stoichiometry on Fuel Cell Performance at Wet Conditions

All 7 MPL materials were also investigated to distinguish their sensitivities with flow stoichiometries at wet conditions. At anode side, the stoichiometry was changed from 1.1, 1.3 to 2.0 with a fixed stoichiometry of 2.0 at cathode side, while at cathode side it was from 1.3, 1.5, 2.0 to 2.5 with a fixed stoichiometry of 1.3 at anode side. Figure 20 shows a typical fuel cell performance with MPL 50 GK. In the figure, solid lines were for the results due to the stoichiometry change at anode side, and dash line were for the ones at cathode side. Generally, for all 7 materials, an increase of anode stoichiometry from 1.1 to 2.0 did not lead to considerable performance change, and all the performance curves were overlapped in the figure. On the other hand, as anticipated, the change of cathode stoichiometry from 1.3 to 2.5 significantly increase fuel cell performance at large current density range and promote current limitations. This indicates that for the cell and conditions tested, hydrogen transport was not limiting while oxygen transport at the cathode was.

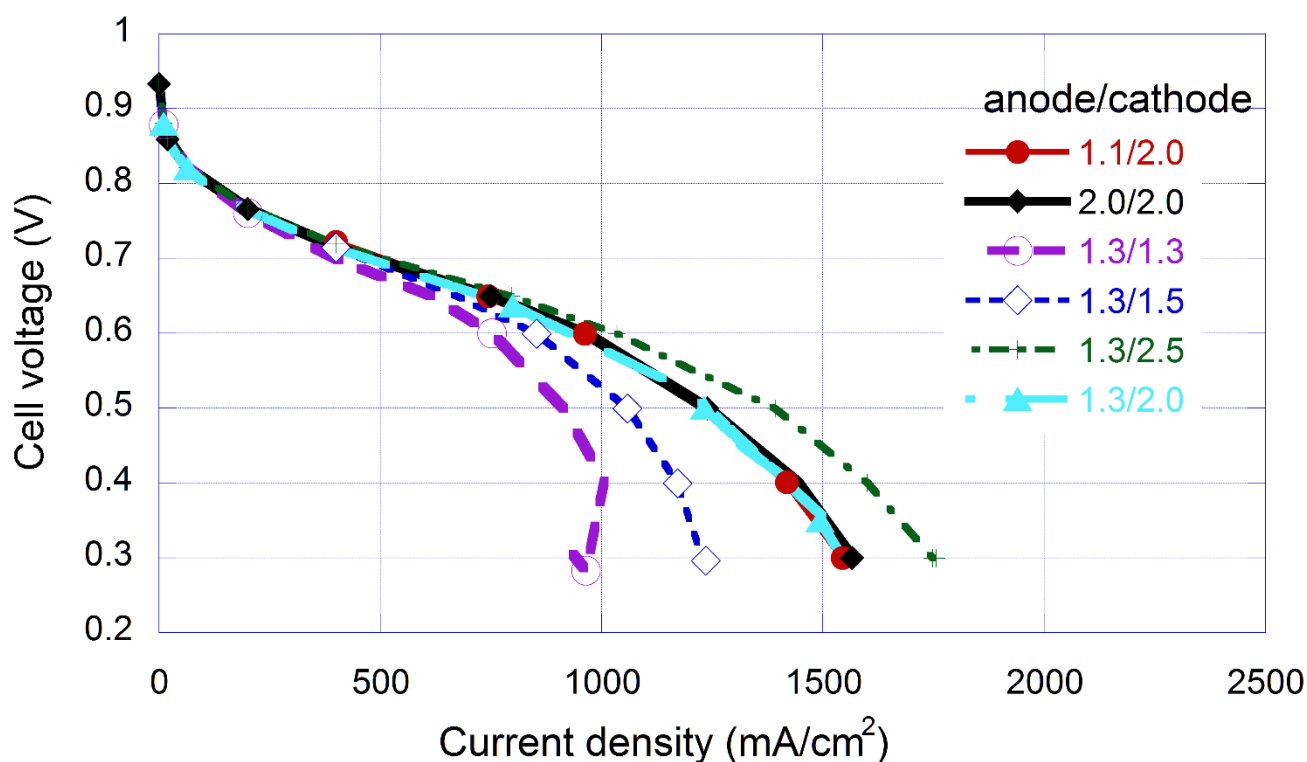


Figure 20 A typical cell performance sensitivities of MPLs with flow stoichiometry at wet conditions, MPL 50 GK.

Figure 21 shows cross comparison results among 7 materials with a stoichiometry at cathode side as X-axis. The cell voltage was fixed at 0.3 V. The increase of flow stoichiometry at cathode side significantly improves mass transport, thus the performance, which could mainly be due to the following benefits: lower flooding, reducing oxygen depletion along channels, and higher aggregate oxygen concentration.

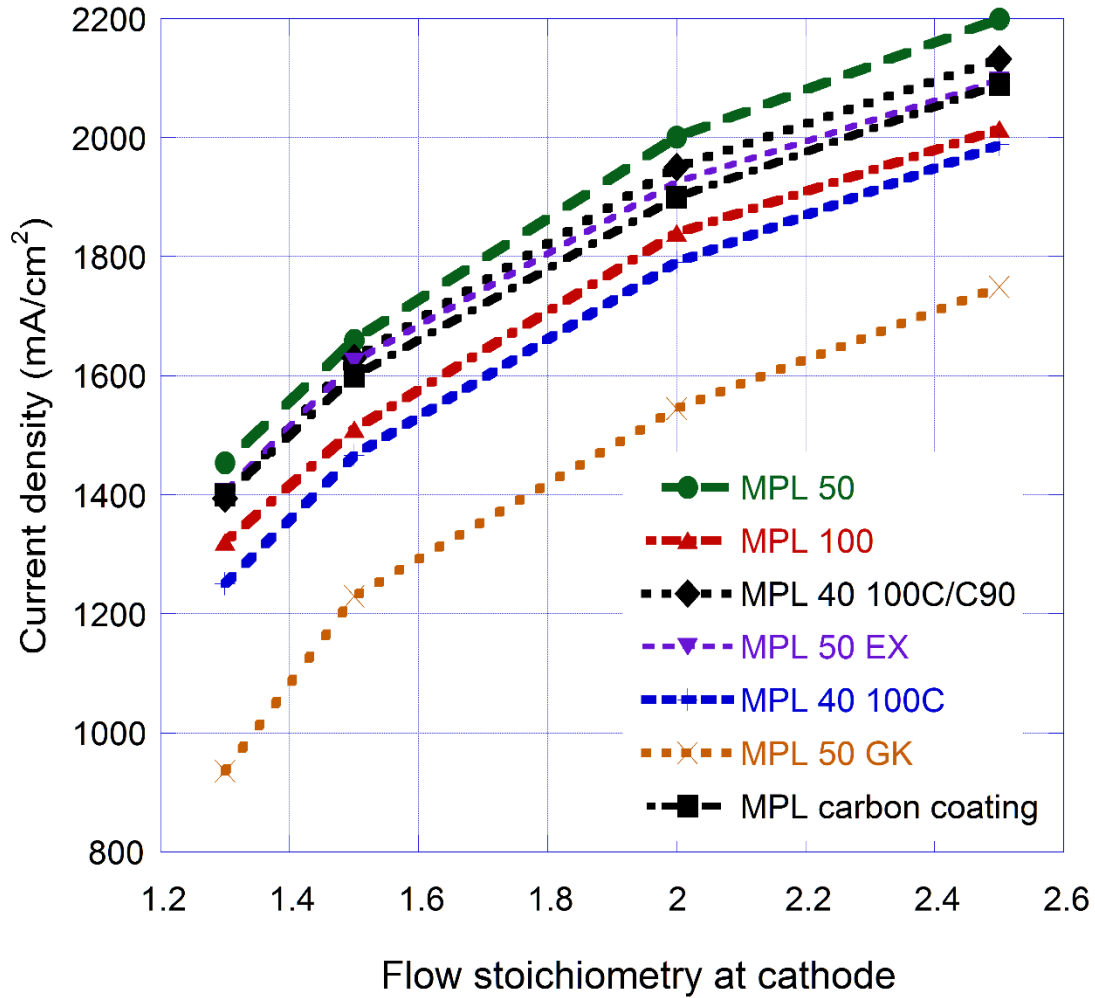


Figure 21 Cross comparison results of all 7 materials under HS condition at a voltage of 0.3 V.

At wet condition with fully humidity, excessive water due to water production and transport from anode will be saturated, and cause severe flooding in diffusion media and flow channels. At low flow stoichiometry and parallel flow channel design of up to 22 channels, liquid water slugs are formed in some of flow channels and blocked the downstream part of the channels, thus resulted in oxygen starvation at the reaction site, reduction of reaction area and reduction in performance. The flow velocities in flow channels will be greatly increased with increasing flow stoichiometry. The larger shear force will remove more liquid water out of flow channel, thus prevent water slug formation. More importantly, higher oxygen concentration at cathode reaction sites were maintained at larger flow stoichiometries, since the oxygen transport through the diffusion media were enhanced because of better convection. In addition, the oxygen distribution along the cathode flow channel with up to 200 mm changed considerably, which caused oxygen concentration depletion along the flow channel, especially at low flow stoichiometries.

To quantitatively investigate the sensitivities of MPL materials to flow stoichiometries, the variabilities, i_{sen} , were introduced, as defined below:

$$i_{sen} = \sqrt{\frac{\sum_{k=1}^n (i_k^2 - i_m^2)}{N}}$$

where i_m is the mean current density with a certain MPL material at a fixed voltage of 0.6 V or 0.3 V. At a low variability, all the current densities are close to the mean one, which indicates a low sensitivity. On the other hand, with a high variability, the data points of the current densities spread away over a large regime, which means a high sensitivity. As shown in Table 6, MPL 50 GK and MPL 50 have larger sensitivity to flow stoichiometry, flowed by MPLs 40 100C and 40 100 C /C90. In addition, the sensitivity was normalized to the value of MPL 50. With larger percentage than 100%, only MPL 50 GK showed more sensitive to the flow stoichiometry at wet condition than MPL 50.

At wet condition with fully humidity, excessive water due to water production and transport from anode will be saturated, and cause severe flooding in diffusion media and flow channels. At low flow stoichiometry and parallel flow channel design of up to 22 channels, liquid water slugs are formed in some of flow channels and blocked the downstream part of the channels, thus resulted in oxygen starvation at the reaction site, reduction of reaction area and reduction in performance. The flow velocities in flow channels will be greatly increased with increasing flow stoichiometry. The larger shear force will remove more liquid water out of flow channel, thus prevent water slug formation. More importantly, higher oxygen concentration at cathode reaction sites were maintained at larger flow stoichiometries, since the oxygen transport through the diffusion media were enhanced because of better convection. In addition, the oxygen distribution along the cathode flow channel with up to 200 mm changed considerably, which caused oxygen concentration depletion along the flow channel, especially at low flow stoichiometries.

To quantitatively investigate the sensitivities of MPL materials to flow stoichiometries, the variabilities, i_{sen} , were introduced, as defined below:

$$i_{sen} = \sqrt{\frac{\sum_{k=1}^n (i_k^2 - i_m^2)}{N}}$$

where i_m is the mean current density with a certain MPL material at a fixed voltage of 0.6 V or 0.3 V. At a low variability, all the current densities are close to the mean one, which indicates a low sensitivity. On the other hand, with a high variability, the data points of the current densities spread away over a large regime, which means a high sensitivity. As shown in Table 6, MPL 50 GK and MPL 50 have larger sensitivity to flow stoichiometry, flowed by MPLs 40 100C and 40 100 C /C90. In addition, the sensitivity was normalized to the value of MPL 50. With larger percentage than 100%, only MPL 50 GK showed more sensitive to the flow stoichiometry at wet condition than MPL 50.

Table 6 Sensitivity results with Stoichiometry and RH.

Sensitivities at 0.3V	With stoichiometry at HS		with RH		With stoichiometry at CA	
	i_{sen}	$\frac{i_{sen}}{i_{sen}(MPL50)}$	i_{sen}	$\frac{i_{sen}}{i_{sen}(MPL50)}$	i_{sen}	$\frac{i_{sen}}{i_{sen}(MPL50)}$
MPL 100	313	94%	458	79%	142	120%
MPL 50	334	100%	580	100%	118	100%
MPL 50 GK	357	107%	392	68%	227	192%
MPL 50 EX	308	92%	493	85%	139	118%
MPL 40 100C/C90	329	99%	500	86%	128	108%
MPL 40 100C	328	98%	502	87%	163	138%
MPL carbon coating	307	92%	475	82%	119	101%

Effects of Flow Stoichiometry on Fuel Cell Performance at Dry Conditions

All 7 MPL materials were also investigated to distinguish their sensitivities with flow stoichiometries at dry conditions. Similarly, the stoichiometry at anode side was changed from 1.1, 1.3 to 2.0 with a fixed stoichiometry of 2.0 at cathode side, while at cathode side it was from 1.3, 1.5, 2.0 to 2.5 with a fixed stoichiometry of 1.3 at anode side. Figures 20 showed a typical fuel cell performance with MPL 50 GK. In the figure, solid lines were for the results due to the stoichiometry change at anode side, and dash line were for the ones at cathode side. Similar to wet condition for all 7 materials, an increase of anode stoichiometry from 1.1 to 2.0 did not lead to considerable performance change, and all the performance curves were overlapped in the figure. The larger of cathode stoichiometry from 1.3 to 2.5, the better fuel cell performance depending on the materials.

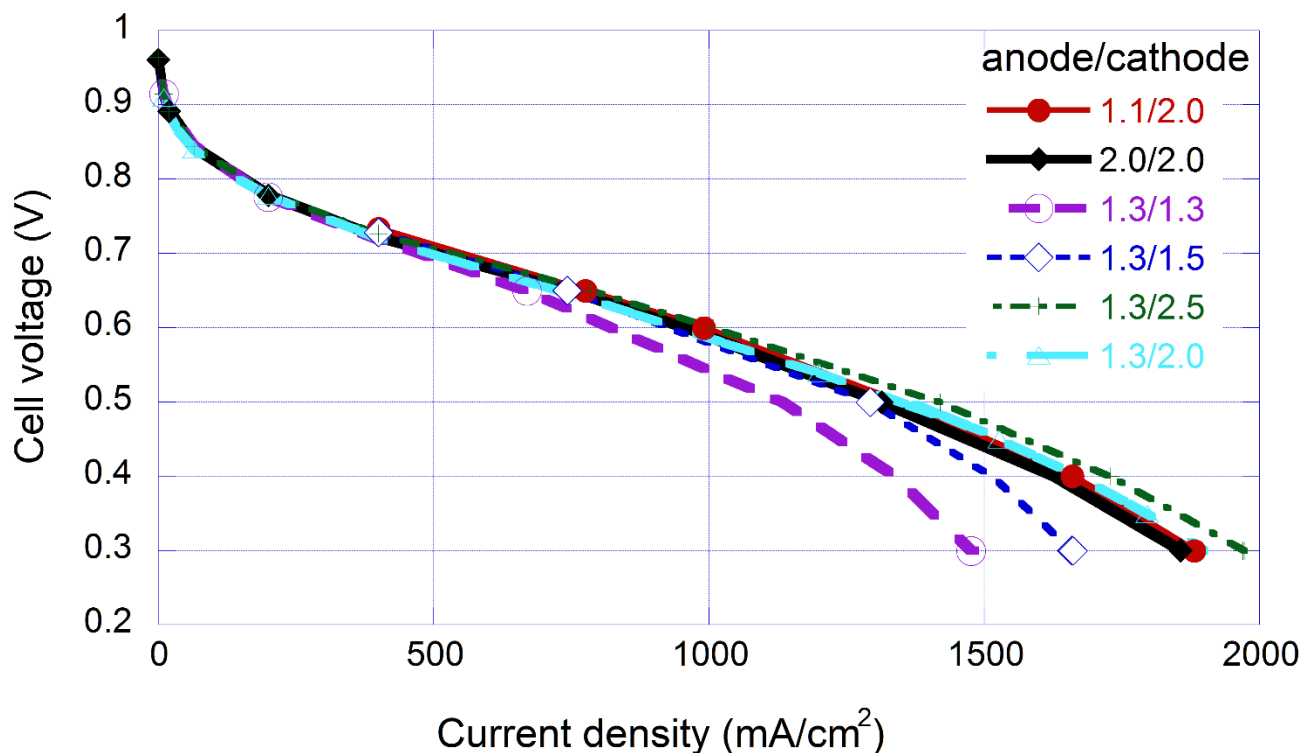


Figure 22 Typical cell performance sensitivities of MPLs with flow stoichiometry at dry conditions with MPL 50 GK.

Figure 23 shows a cross comparison of fuel cell current densities of all 7 MPLs at 0.3 V. The current densities increased with flow stoichiometries, while the changes were different from the materials. Differing from the wet conditions, the current density changes of all MPLs were much less under dry conditions, and their performance variabilities were considerably smaller than ones at wet conditions, as detailed in Table 6. Especially, a little difference was found with MPLs 40 100C and 40 100C/C90 from 2.0 to 2.5. As shown in Table 6, MPL 50 GK still has the largest sensitivity to flow stoichiometry at dry condition, likely a result of the Si inclusion. MPL 50 is the least sensitive one in this condition.

As previously discussed, at dry conditions, the performance is mainly dominated by ohmic drop and oxygen concentrations at reaction sites. There was a tradeoff between them at dry conditions. Higher flow stoichiometry at cathode side promoted liquid water removal and oxygen concentrations due to both diffusion and convection, while causing membrane dryout across MEAs, thus increased ohmic loss. In MPL 50 GK, the hydrophilic features maintained better water uptake in fuel cells through the test conditions and minimized their effects on HFR, showed a positive response to the increase of flow stoichiometry from 1.3 to 2.5. In hydrophobic MPLs, promotion of liquid water removal and oxygen concentrations were more dominant than HFRs due to MEA dryout at low flow stoichiometry range from 1.3 to 2.0. After that, MEA dryout had greater impacts than on fuel cell performance.

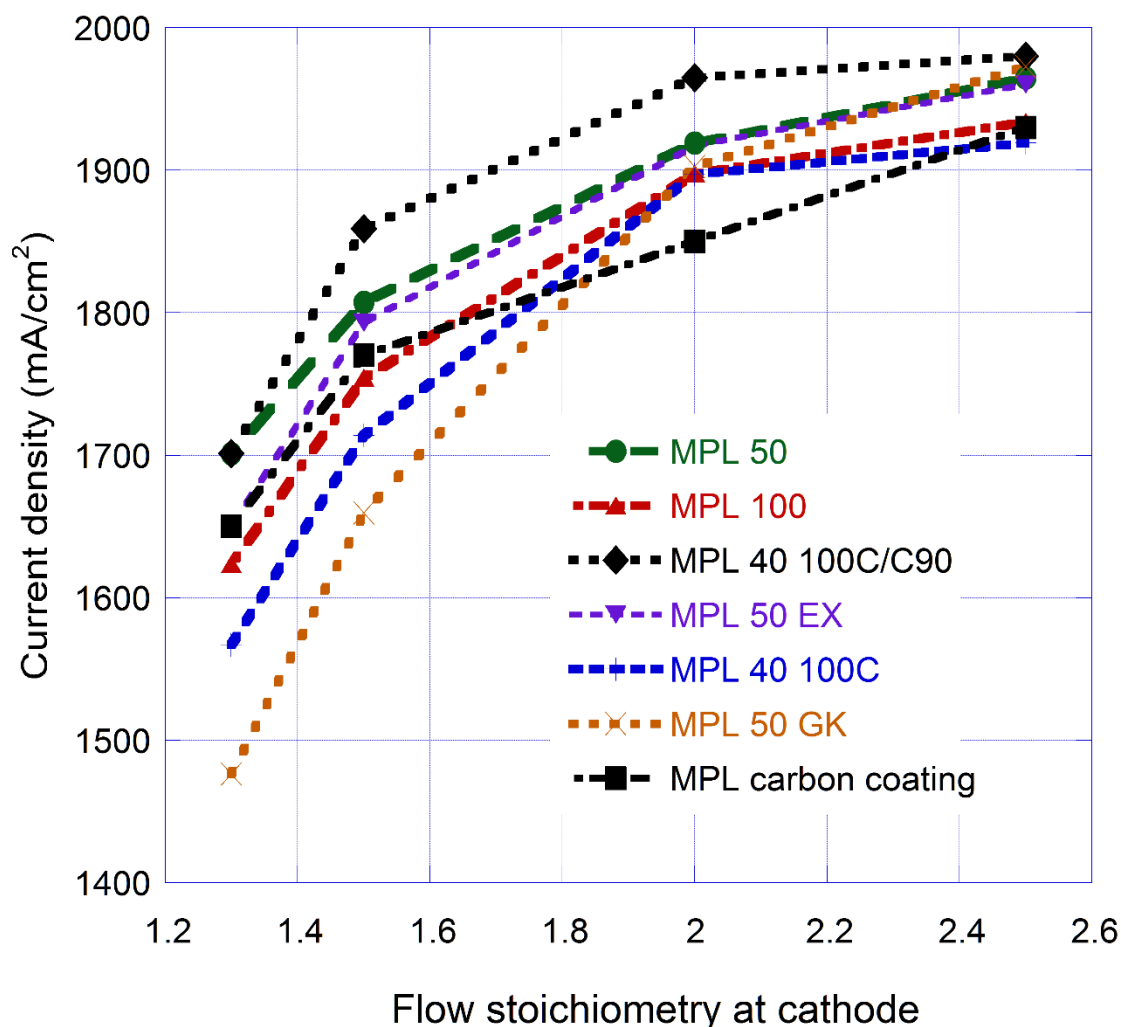


Figure 23 Cross comparison results of all 7 materials under FA condition at a voltage of 0.3 V.

Effects of Relative Humidity on Fuel Cell Performance

With a fixed stoichiometry of 1.3/2.0, the sensitivities of MPL materials to relative humidities (RHs) with a wide range from 19% to 79% were investigated. The dew point temperatures at both anode and cathode sides were kept at a fixed point of 55 °C, the cell temperature was increased from 60, 70, 80, 87, 95 °C to desired RHs. Figures 24 and 25 showed a typical fuel cell performance and cross comparison results, respectively. Differing from the effects of flow stoichiometry on fuel cell performance, the relative humidity had significant impacts over a wide current density range from low to high. The fuel cell performances of all materials were basically increased with RHs at test range due to the improvement of membrane conductivity, reaction thermodynamics and kinetics, thus reducing their resistances. It should be noted that the decreases of reactant (O_2 and H_2) partial pressures due to higher RH had a very limited impact on fuel cell performance.

At the higher end of RHs, mass transport becomes more important. As shown in Figure 24, less hydrophobic MPL 50 GK reached its current limitation at a RH of 51% and did not extent its performance even with higher RH of 79%. As shown in Table 6, MPL 50 GK had the least sensitivity to RHs.

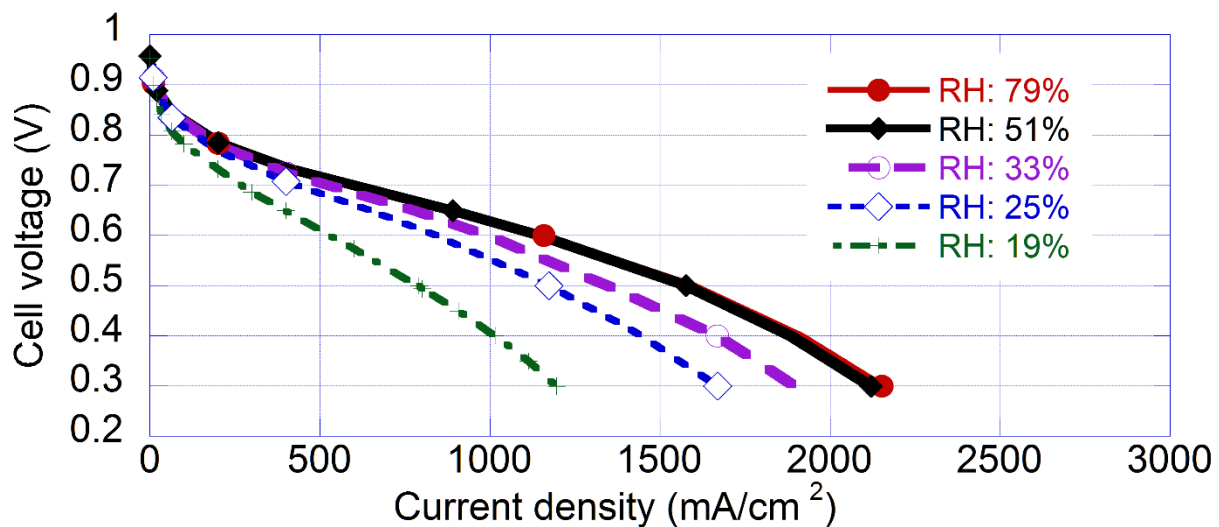


Figure 24 Typical Cell performance with different RHs under different relative humidities with MPL 50 GK.

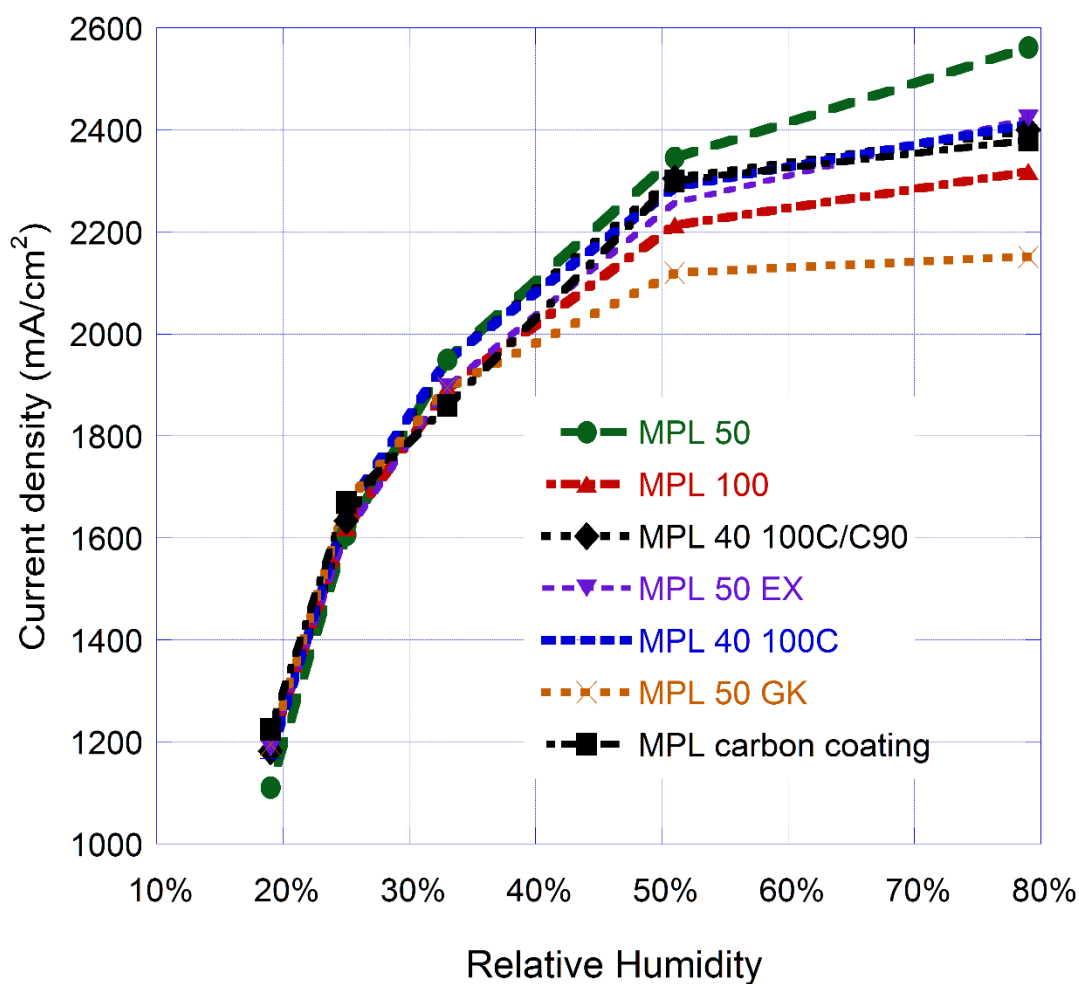


Figure 25 Cross comparison results of all 7 materials with RHs at a voltage of 0.3 V.

Tests with Heliox

Heliox was introduced to investigate the gas phase transport behavior at both wet and dry conditions for better understanding of all MPL materials. Figure 26 shows a typical test result with MPL40 100C C90 at the same operating condition, which indicates larger current limitation with heliox at wet condition, and worse performance at dry condition. These are confirmed with all other MPL materials. The helium in heliox replaces nitrogen in air, resulting in enhanced oxygen and water vapor diffusion (about 3 or 4 times. This results in reduced oxygen limitations, but rapid dryout in dry conditions, as shown in Figure 26.

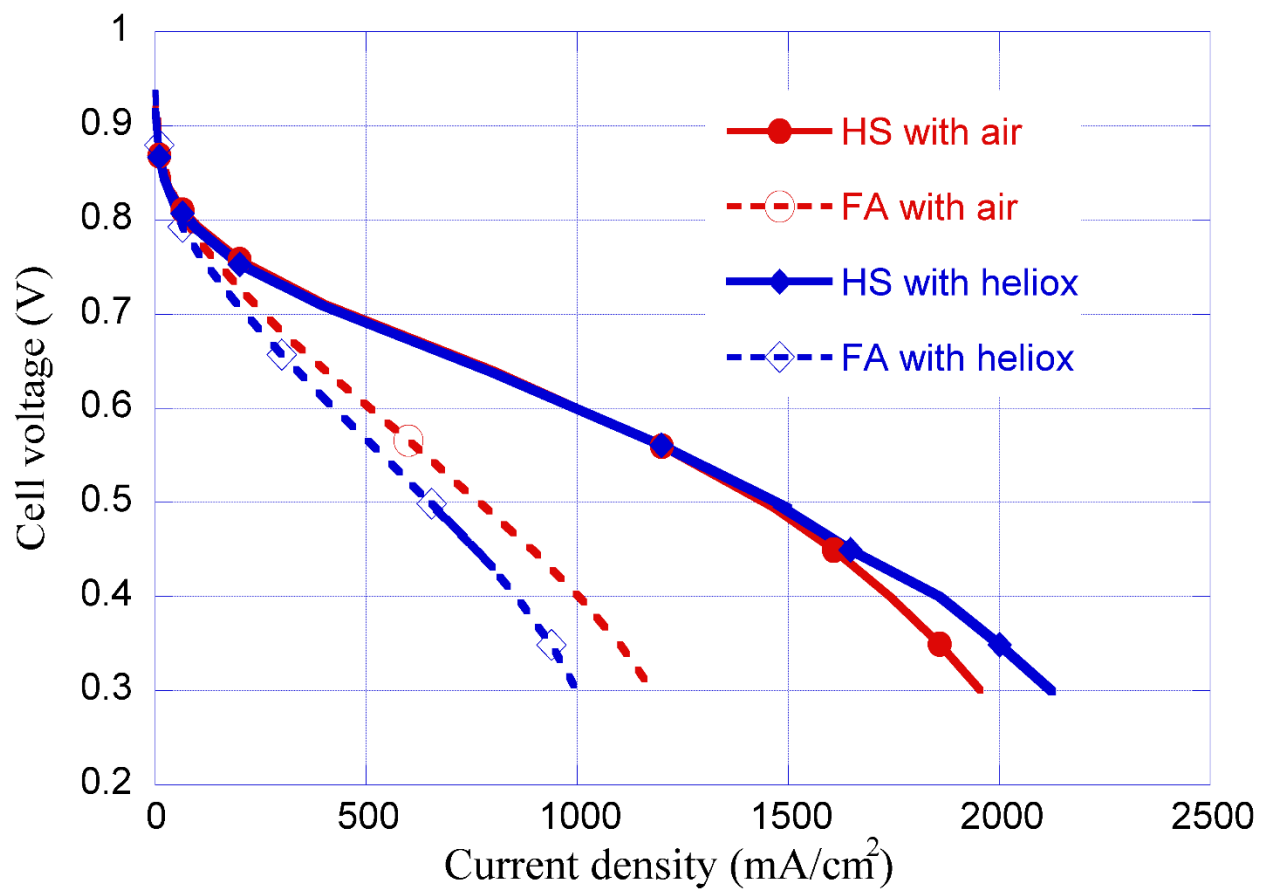


Figure 26 Performance results with air and heliox at wet and dry conditions.

Net Water Drag Measurements

The net water transport across the MEA has been investigated by deriving the difference of water content in anode and cathode sides at dry and wet operating conditions. The water contents on both sides were measured with desiccant collections right after the fuel cell outlets and before the back pressure unit, as addressed in previous reports. Table 7 shows a typical result of water content at dry FA condition with a collection time of 60 minutes at a constant current of 40 A. The net water drag coefficient was calculated based on water transport value from anode to cathode. All the MPL materials have a very small net water drag coefficient, which ranged from 0.023 to 0.049. The cell with MPL 50 GK had the smallest value, which indicated less water was needed from anode to maintain the same current with more hydrophilic MPL, which retained more water in MEAs. *Interestingly, the changes in MPL properties did not have large changes in net drag measured, although we believe the 50GK differences are at least statistically meaningful.*

Table 7 Water measurement results of MPL materials at dry condition

MPL	Condition	Cathode [g]	Anode [g]	Total [g]	Calculated net drag coefficient
MPL-50	HS: 60A, 15 min.	24.7	2.2	26.9	0.374
	FA: 40A, 60 min.	20.2	0.70	20.9	0.049
MPL-100	HS: 60A, 15 min.	24.4	2.6	27.0	0.334
	FA: 40A, 60 min.	20.6	1.2	21.8	0.030
MPL 40 100 C/C90	HS: 60A, 15 min.	24.2	2.5	26.7	0.344
	FA: 40A, 60 min.	20.9	1.0	21.8	0.038
MPL 50 G K	HS: 60A, 15 min.	24.2	2.7	26.9	0.324 (Smallest)
	FA: 40A, 60 min.	20.9	1.4	22.3	0.023 (Smallest)
MPL 40 100C	HS: 60A, 15 min.	24.3	2.3	26.6	0.364
	FA: 40A, 60 min.	21.4	0.8	22.2	0.045

4. Results and Discussion (Computational)

To complement the experimental component of the research, a computational simulation study was conducted with the objective of understanding the fundamentals involved in the observed differences in performance and water management with the tailored MPL surfaces. To achieve this, several tasks were completed:

- 1) A single-phase computational parametric study of the MPL thickness, porosity, permeability, and thermal conductivity for symmetric material sets in PEFCs was exercised to define the key controlling parameters in performance.
- 2) A multi-phase flow capability was integrated into an existing 2-D computational PEFC model framework. Main assumptions of the model are given below, further details of the model development and most recent implementation are given elsewhere in published work, most recently in Gandomi et al, JES 2016. In the work discussed here, the computational framework was applied to a 2-D control volume (see Figs 27 and 28) to study W. L. Gore specific materials.
- 3) A multi-phase computational parametric study of the materials was executed at high and low current, under a wide range of operating conditions, to predict and understand the observed trends.
- 4) A multi-phase flow parametric (Taguchi) study on the impact of MPL thickness, porosity, permeability, and thermal conductivity for symmetric material sets in PEFCs was completed to define the key controlling parameters in performance, all else being equal.
- 5) A multi-phase flow computational study was executed to understand the limits of thermal control with MPL and DM thermal properties and the limits of asymmetric material sets for future application.

Basic assumptions of the model include:

- Steady-state operation.
- The product water of the electro-chemical reaction is in liquid form and then phase change process such as evaporation and condensation occurs until phase equilibrium is achieved.
- Material properties are homogeneous within an individual layer, but can be anisotropic.
- Knudsen diffusion is considered only in micro-porous layer and catalyst layer considering the pore size. Knudsen diffusion and bulk diffusion are treated as resistance in series.
- The agglomerate in the catalyst layer is an isothermal and equipotential sphere.
- The water dissolved into the ionomer phase is calculated by the equilibrium water sorption.

The model contains the following basic physics:

- Agglomerate model of electrodes with published kinetics used
- Knudsen diffusion in the CL and MPL
- Capillary flow in PM with internally measured relationship for DM

- Phase change induced flow via thermodynamics
- Multi-component diffusion via Stefan-Maxwell relationships
- Convection of heat and mass via gas and liquid phases
- Non-adiabatic boundary condition to allow heat transfer to coolant

The model used for this research has been developed over the years in various different research programs. For this program, the model was upgraded and tailored in several ways:

- 1) Temperature gradient driven multi-phase transport in the form of Phase-Change-Induced flow in the porous media (catalyst layer, MPL, and DM) was included.
- 2) Capillary flow in the porous media (CL, MPL, and DM), derived from direct measurement of capillary flow in standard DM materials was included.
- 3) Updated electrode model based on agglomerate transport description and most up-to-date electrode description available.

The model used is a 2-D model built on the framework of a 2-D and 2-D + 1 model developed in the lab with various other projects. Those other projects have included extensive and continual validation, are well published, and are the best available predictors of PEFC performance within the ranges of parameters and test protocol evaluated.

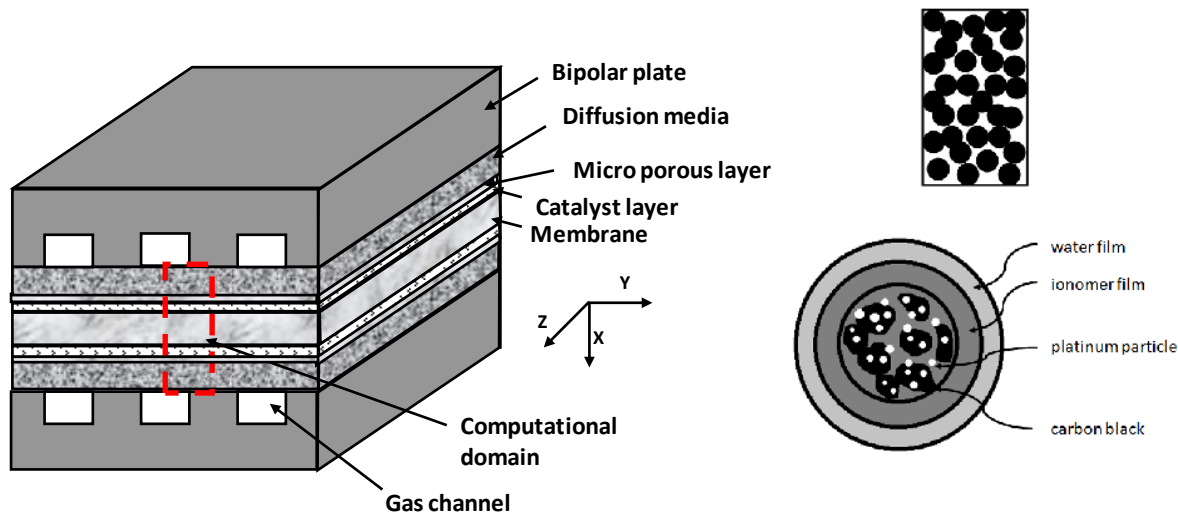


Figure 27 Schematic of 2-D domain applied (left) and agglomerate model of the electrodes utilized in the computational model.

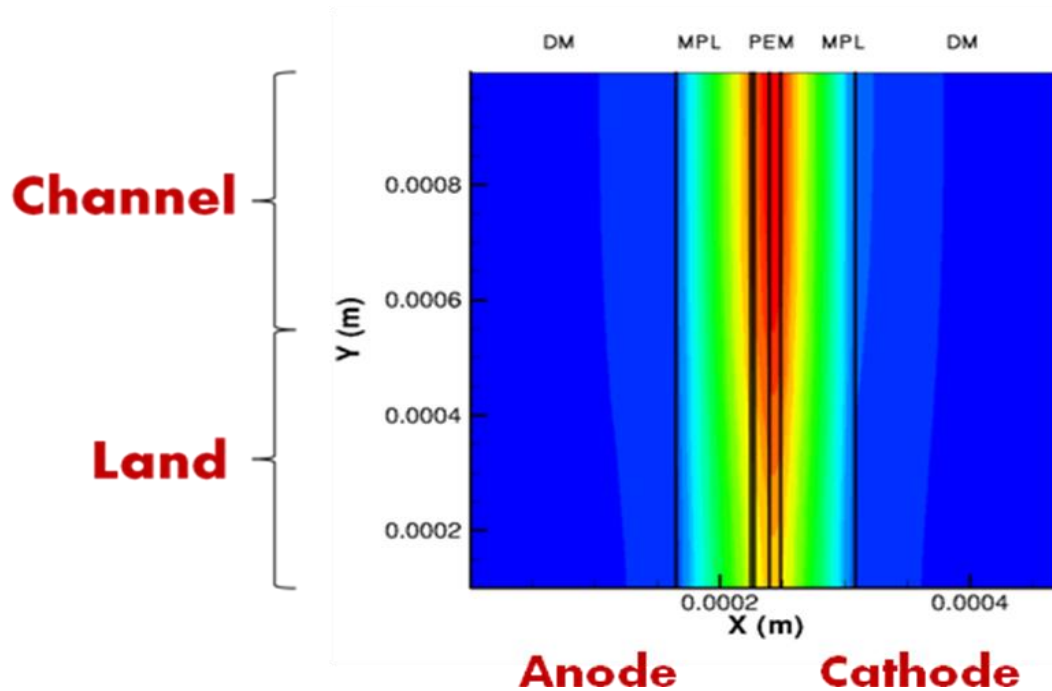
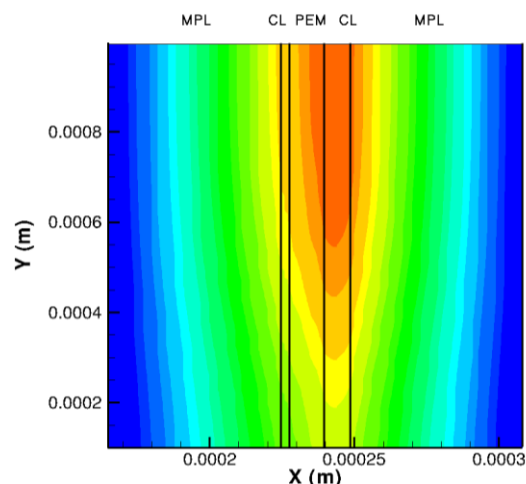


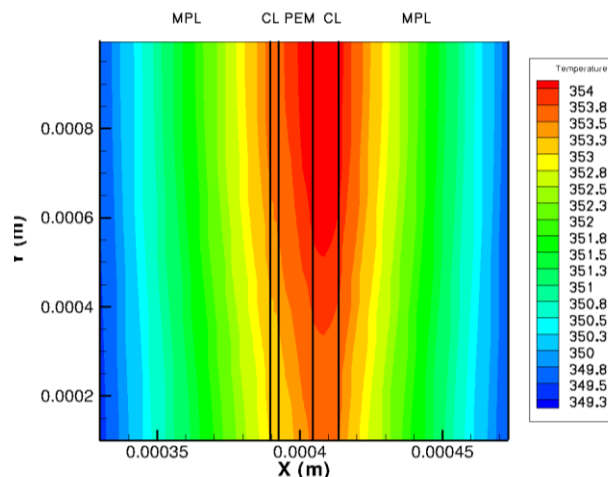
Figure 28 Typical temperature contour plot of the 2-D domain simulated including channel, land and anode-to-cathode DM structure.

A summary of these results is as follows:

- The difference in temperature drop from the CL to the edge of the DM is significant (see Fig. 29). Control of the temperature gradient is critical in dry and high temperature operation, where evaporative removal (Phase change induced PCI flow) can be critical, and is not included in this single-phase situation.
- Based on the results, if the macro DM has a high relative thermal conductivity, control of the temperature gradient (and hence water removal) can be accomplished with the MPL thickness or k^{th} .
- Anode/cathode MPL and/or DM asymmetry can potentially protect anode from dryout and promote removal at cathode, since it can be used to alter predicted temperature levels and gradients.
- Membrane thickness variation has little impact in terms of internal temperature gradient variation, ohmic and cross-over impacts are far more dominant.



Case1



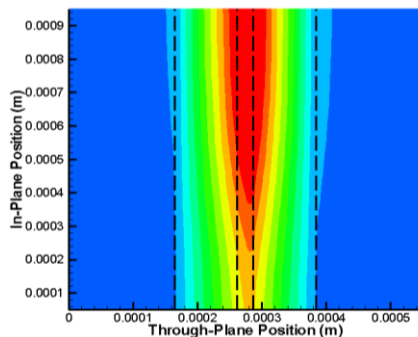
Case 2

Figure 29 Temperature contour plot of the 2-D domain simulated including channel, land and anode-to-cathode DM structure for Case 1 and Case 2 from Table 2.

Multi-Phase Computational Parametric Study of the Materials Tested

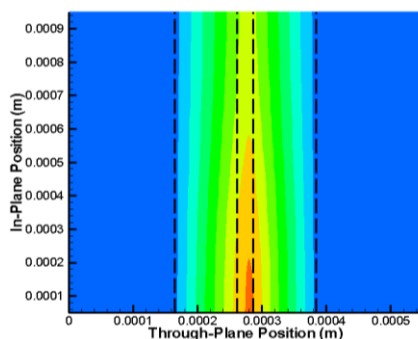
In this portion of the study, a parametric study of the performance and internal temperature, potential, and mass profiles was conducted to simulate the materials provided by W. L. Gore for the experimental portion of the program. Test conditions considered were also the same range as those investigated experimentally. This was accomplished following upgrade and partial validation of the computational model to include multi-phase physics and transport in the porous media as described. The key parameters investigated included the MPL thickness, porosity, thermal conductivity, and permeability. All simulations were of a symmetric configuration with similar materials on the anode and cathode.

Results indicated that there is a temperature inversion phenomenon with conventional channel/land architecture, as seen in Fig. 30. In a wet condition, due to flooding under the lands, the hottest location becomes that under the channel due to the majority of reactant availability and hence reaction in this location. However, under dry conditions, the area under the channel becomes too dry and the activity under the land is higher, driving up temperature in this location. Considering that automotive applications are likely to experience both conditions from start-up through steady-state, this bias needs to be considered in terms of durability and design when a conventional channel/land configuration is used. If a thick DM with high in-plane conductivity is used, much of this bias can be eliminated, however.



SW condition – hottest location under the channel. This is where the highest current activity is in wet condition.

Performance is invariant with chosen variables at high CD



FA condition – hottest location under the land. Storage of water there allows highest current under dry conditions.

Performance is sensitive to parameters, especially MPL thickness

Figure 30 Temperature contour plot of the 2-D domain simulated including channel, land and anode-to-cathode DM structure for Case 1 and Case 2 from Table 2.

Other key findings from this portion of the computational study include:

- The dry case (CA) and very dry case (FA) do not show significant two-phase effects. The reaction is more concentrated under the land because the limiting factor is ohmic resistance instead of transport loss. Heliox results also confirmed this experimentally. Thus, a single-phase model can be appropriate for these conditions.
- By contrast in the wet case (HS) and very wet case (SW), reaction is more concentrated under the channel because the in-plane transport is limiting the performance rather than the ohmic loss.
- The temperature gradient through the inner layers is also dependent on the thermal conductivity of catalyst layer, which is taken from literature. Although outside the scope of this study, this parameter therefore also represents a potential parameter which can be engineered to achieve a change in the water management.
- MPL 100 consistently was predicted to result in the worst performance regardless of the hydration conditions due to its high thickness and other parameters, which was observed experimentally. The 50 GK performance observed experimentally could not be captured by the model indicating the dominance of the Si inclusion on the wet operation.
- MPL sets with lower thickness, higher thermal conductivity and higher porosity are consistently predicted to give better performance, such as MPL 40 100°C C90, MPL 50 2EX, MPL 40 100°C.

Multi-Phase Computational (Taguchi) Study

To quantify the key controlling variables in MPL that can be engineered so future materials can be more efficiently designed, the relative impact of the MPL thickness, porosity, permeability, and thermal conductivity for symmetric material sets was conducted. In a Taguchi study, a high and low value of the variables of interest is chosen, and testing is conducted and the output variable(s) is assessed as a function of the chosen inputs, within the range of parametric permutation selected (see Table 10). For these tests which were performed computationally, the high and low values chosen represent what we believed to be high and low values that were possible with conventional engineering practices based on feedback from W. L. Gore engineers.

Table 10 Parameters Used in Taguchi Study.

Test Run	Thermal Conductivity A	Thickness B	Through Plane Permeability C	Porosity D	Output Metric (V)
1	-	-	-	-	
2	+	-	-	-	
3	-	+	-	-	
4	+	+	-	-	
5	-	-	+	-	
6	+	-	+	-	
7	-	+	+	-	
8	+	+	+	-	
9	-	-	-	+	
10	+	-	-	+	
11	-	+	-	+	
12	+	+	-	+	
13	-	-	+	+	
14	+	-	+	+	
15	-	+	+	+	
16	+	+	+	+	

Parameter	Up (+) Value	Down (-) Value
Thermal Conductivity (in and through plane)	0.24 W/mK	0.12 W/mK
Thickness MPL	100 micron	40 micron
Through plane permeability	1100 ml/(min · cm ² · kPa)	6 ml/(min · cm ² · kPa)
Porosity	90	63

All cases: Stoich anode = 1.3
cathode = 2.0. Backpressure = 50
Dew Point = 55/55

Test conditions simulated were as follows with a 1:1 channel/land configuration.

CASE 1: CA: High voltage and low voltage T=80, Dew point = 55/55

CASE 2: CA High voltage and low voltage T=80, Dew point = 55/55

CASE 3: FA: High voltage and low voltage T=95, Dew point = 55/55

CASE 4: FA High voltage and low voltage T=95, Dew point = 55/55

CASE 5: HS: High voltage and low voltage T=80, Dew point = 100/100

CASE 6: HS High voltage and low voltage T=80, Dew point = 100/100

In all cases, the anode/cathode stoichiometry was 1.3/2.0, and the anode/cathode backpressure was 50 kPa. For each of these conditions, a 24 test matrix, or 16 computational runs per voltage (High voltage and low voltage were dependent on the test conditions and chosen to achieve a high current and low current output, normally 0.7 V and 0.4 V respectively) resulted in 32 computational simulations per case with an output metric of current density.

After testing was completed, the fact that the simulated channel/land ratio was 1:1 while the experimental design was 3:1 was discussed, and additional simulations were conducted as follows:

CASE 7: CA: High voltage and low voltage T=80, Dew point = 55/55

CASE 8: HS High voltage and low voltage T=80, Dew point = 100/100

Tables 11-13 show the results for the 1:1 channel to land ratio simulations. Note that the output is in A/m², so numbers represent A/cm² divided by 1000, and are not particularly significant below $\square(100)$.

Table 11 CA condition output 1:1 C|L ratio.

Low Current

Variable	Impact A/m ²
MPL Thermal Conductivity	41
MPL Thickness	-314
MPL Through Plane Permeability	0
MPL Porosity	45

High Current

Variable	Impact A/m ²
MPL Thermal Conductivity	366
MPL Thickness	-867
MPL Through Plane Permeability	0
MPL Porosity	131

Table 12 FA condition output 1:1 C|L ratio.

Low Current

Variable	Impact A/m ²
MPL Thermal Conductivity	103
MPL Thickness	-1046
MPL Through Plane Permeability	0
MPL Porosity	99

High Current

Variable	Impact A/m ²
MPL Thermal Conductivity	1737
MPL Thickness	-3669
MPL Through Plane Permeability	1
MPL Porosity	41

Table 13 HS condition output 1:1 C|L ratio.

Low Current

Variable	Impact A/m ²
MPL Thermal Conductivity	1
MPL Thickness	-221
MPL Through Plane Permeability	-23
MPL Porosity	2

High Current

Variable	Impact A/m ²
MPL Thermal Conductivity	-247
MPL Thickness	-1782
MPL Through Plane Permeability	189
MPL Porosity	1318

From this output, the following conclusions for the 1:1 C|L ratio can be summarized, which are of course subject to the veracity of the model itself, and all other things equal:

- MPL thickness is the strongest parameter with an influence that grows with current. *Thinner is better* for all cases wet and dry due to mass transport. (note: symmetric cases only).
- High thermal conductivity becomes critical for higher current, high temperature, dry conditions but is nearly insignificant at low current. This is an excellent result for design since it means it can be used to tailor high temperature operation but not effect start-up in a significant manner.
- In wet conditions, a *low* MPL thermal conductivity is desired at high current.
- Porosity and through plane permeability only becomes critical at high current wet conditions

For the high channel to land cathode design simulated, results were the same, as shown in Table 14, except the influence of thermal conductivity at high current for HS wet conditions. The 3:1 ratio results show need to reject heat, the 1:1 results show need to retain heat to drive off moisture.

Table 14 CA and HS condition output comparison for different C/L ratios.

CA: Low CD: 1:1		Low CD: 3:1 Ratio		High CD: 1:1 Ratio		High CD: 3:1 Ratio	
Variable	Main Effect	Variable	Main Effect	Variable	Main Effect	Variable	Main Effect
thermal conductivity	40.57	thermal conductivity	40.95	thermal conductivity	366.40	thermal conductivity	365.30
thickness	-313.97	thickness	-270.22	thickness	-867.72	thickness	-1112.78
through-plane permeability	-0.00	through-plane permeability	0.00	through-plane permeability	-0.02	through-plane permeability	-0.025
porosity	45.42	porosity	24.87	porosity	131.88	porosity	142.58

HS: Low CD: 1:1 Ratio		Low CD: 3:1 Ratio		High CD: 1:1 Ratio		High CD: 3:1 Ratio	
Variable	Main Effect	Variable	Main Effect	Variable	Main Effect	Variable	Main Effect
thermal conductivity	1.36	thermal conductivity	9.00	thermal conductivity	-246.71	thermal conductivity	715.73
thickness	-221.34	thickness	-212.29	thickness	-1781.86	thickness	-1450.09
through-plane permeability	-23.45	through-plane permeability	-16.85	through-plane permeability	189.47	through-plane permeability	76.14
porosity	1.83	porosity	-1.76	porosity	1317.78	porosity	1194.32

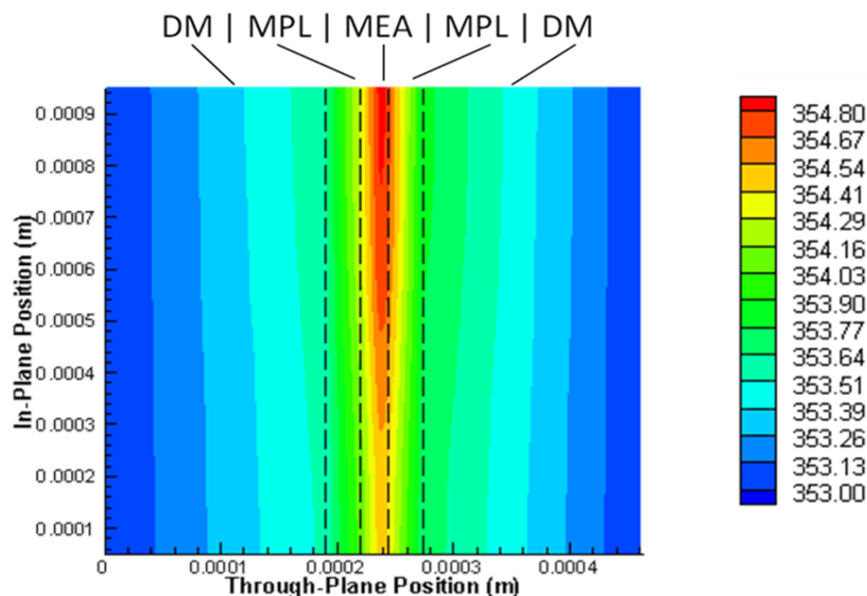
Multi-Phase Study of the Role of Thermal Control and use of Asymmetric Material Sets

The purpose of this preliminary simulation was to quantify how much thermal control could be achieved by varying the properties of material sets based on currently available materials. Table 15 shows the test conditions simulated. All simulations were conducted at a cell temperature of 80°C, with zero back pressure, 100/100 A/C inlet humidity, and an A/C stoichiometry of 1.3/2.0, respectfully.

Table 15 Test parameters for asymmetric material study.

	Thickness (μm)	Thermal Conductivity (W/mK)
“Thin” MPL	30	0.25
“Thick” MPL	100	0.1
“Normal” MPL	60	0.18
“Thin” DM	190	1.7
“Thick” DM	410	0.22

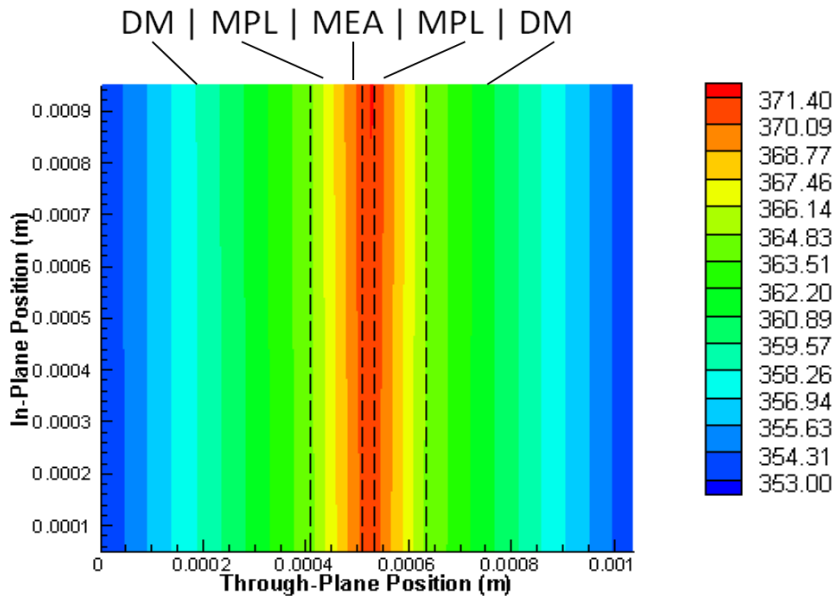
Figures 31 and 32 show some extremes of the internal temperature distribution achievable with conventional materials at high current. For the minimized resistance cases, the temperature gradient between the cathode (highest temperature location for symmetric cases), can still reach 5°C for 2 A/cm². This is significant enough to drive a dominant fraction of the water generated in the vapor phase¹. For the higher thermal resistance case of Figure 32, the temperatures increase so much that in normal operation, dryout would likely limit current unless extremely high RH input was used.



Minimized ΔT , $\sim 2^\circ\text{C}$ at $1\text{A}/\text{cm}^2$, $\sim 5^\circ\text{C}$ at $2\text{A}/\text{cm}^2$.

Figure 31 Minimized temperature gradient material set (symmetric) with thin macro and high k_{MPL} and k_{DM} at 2 A/cm².

¹ Kim, S., and Mench, M. M. 2009. Investigation of Temperature-Driven Water Transport in Polymer Electrolyte Fuel Cell: Phase-Change Induced Flow, *Journal of Electrochemical Society*, **156** pp. B353-B362.

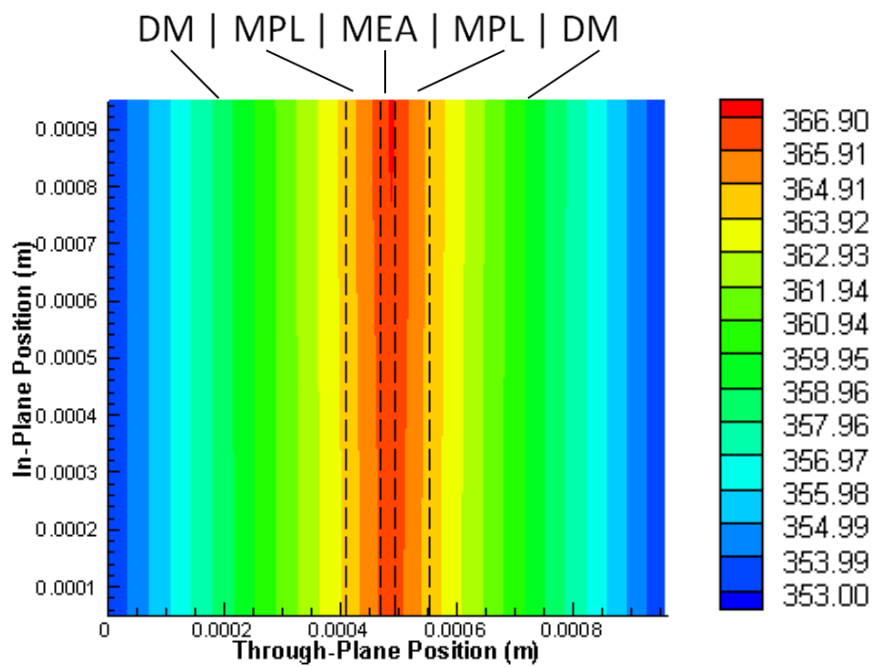


Much greater ΔT , $\sim 16^\circ\text{C}$, lower performance. Operation at 2 A/cm^2 is not possible. Evaporative loss is extreme.

Figure 32 Maximized temperature gradient material set (symmetric) with thick macro and low k_{MPL} and k_{DM} at 2 A/cm^2 .

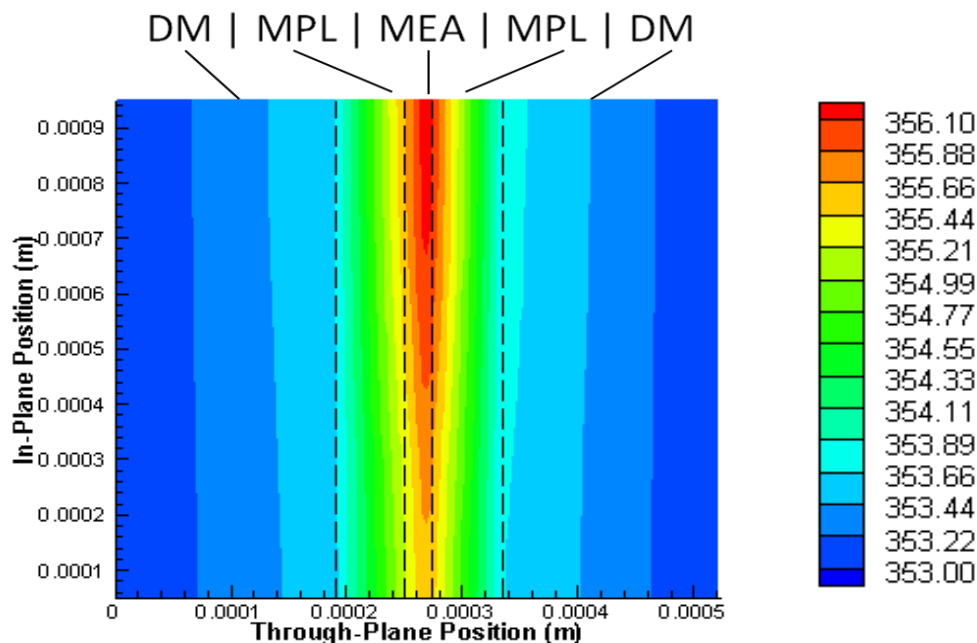
Figures 33 and 34 were generated to look at comparing the dominance of the macro DM on the internal temperature profile for thick and thin macro configurations. For a thick DM configuration, most of the internal temperature profile occurs though the macro portion, minimizing the impact of the thinner MPL and CL sections. This also has the effect of reducing the thermal bias from the channel/land configuration, which can be beneficial in durability, mass distribution, and start-up shut down as well. When the macro DM is reduced in thickness, the MPL and CL thermal properties become much more important, and greater impact should be achieved by tailoring their properties. With macro DM with high thermal resistance, very little impact can be achieved through the CL and MPL thermal property adjustment. However, as the macro DM becomes thinner, as is the trend, the thermal properties of the CL and MPL as well as the interfacial properties will all begin to become important and perhaps dominate inside the PEFC.

It should be noted the results of the thick and thin macros are similar to a low and high thermal conductivity macro, respectively. These simulations were also conducted and communicated to W. L. Gore but not shown here. Since thermal resistance is proportional to the thickness, and inversely proportional to the conductivity, the combined factor scales directly with temperature gradient for a given heat flux and *both* parameters can be engineered to achieve the same goal. In this case, the choice of how to achieve the desired effect would be based on the other impacts including mass transport and assembly volume.



Control of the temperature gradient is through the macro DM, and C|L bias is minimized at the CL.

Figure 33 Macro DM temperature gradient control material set (symmetric) with thick macro and normal MPL at 1 A/cm².



For thin DM, control of the temperature gradient is through the MPL properties, and Channel/Land bias is evident.

Figure 34 MPL DM temperature gradient control material set (symmetric) with thin macro and normal MPL at 1 A/cm².

Figure 35 shows the limits of the thermal control achievable with the materials listed in Table 9 asymmetrically installed in the PEFC. For 1 A/cm² (and other currents), it can be seen that the temperature gradient can in fact be shifted from the cathode to anode side. Normally, the cathode side is slightly higher due to the higher polarization at this location. In the membrane, water moves toward the warmer location due to thermo-osmosis. This effect is smaller than electro-osmotic drag², but becomes relevant in high-current situations where performance is limited by anode dryout. Additionally, since water moves via PCI flux toward cold locations in the porous media, increasing the gradient in the anode so that more water moves to that side can increase back flux and reduce the net drag coefficient, which would enhance performance in low RH, high power operation.

² Kim, S., and Mench, M. M. 2009. Investigation of Temperature-Driven Water Transport in Polymer Electrolyte Fuel Cell: Thermo-osmosis in Membranes, *Journal of Membrane Science*, **328**, pp. 113-120.

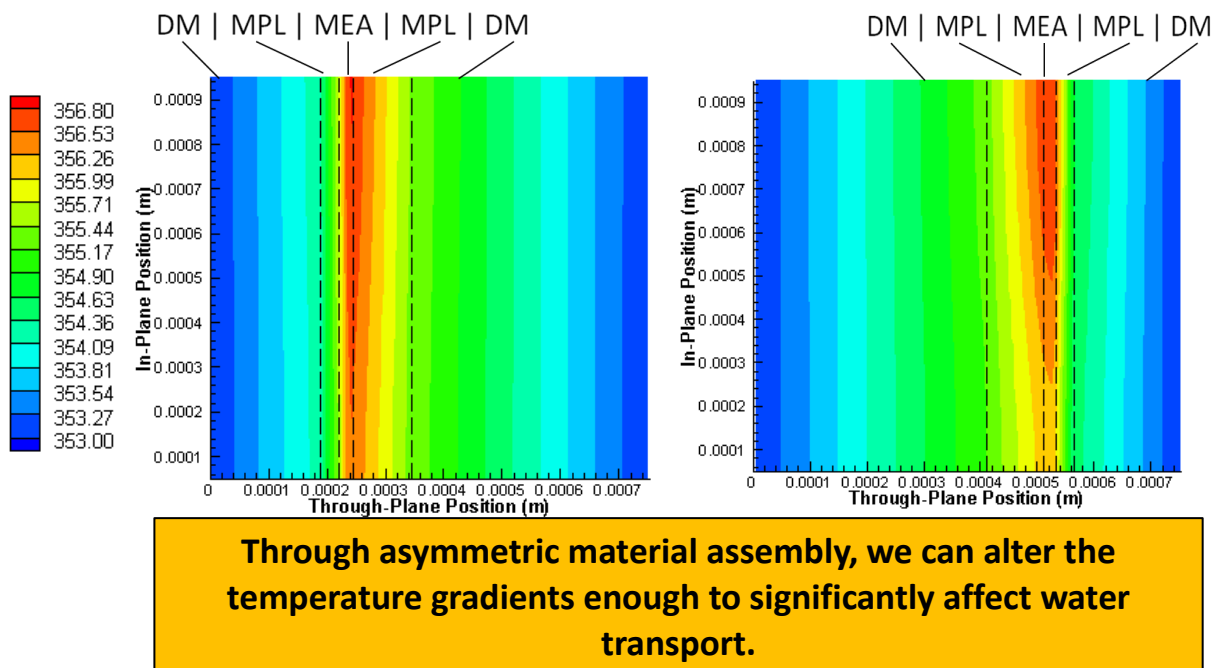


Figure 35 Comparison of temperature gradient achieved with asymmetric material sets using thin, high conductivity material anode material set and thick, low conductivity cathode (left) compared to the reverse assembly (right)

Summary and Conclusions

An extensive computational and experimental study was conducted to assess and understand the impact of thermal and mass transport parameters in the MPL on operational performance. 7 MPL materials with different thickness, hydrophobicity and pore morphology were investigated both *in-situ* and *ex-situ* experimentally, and a wide range of computational simulations were conducted with a 2-D model including multi-phase effects over a wide range of operating conditions. The thermal conductivities of 7 composite materials were measured, the surface compositions were assessed of all MPLs, and a comprehensive test matrix, including SW (superwet), HS (wet), CA (dry) and FA (extreme dry), were applied to all 7 materials for *in-situ* tests. EIS and water measurements were also performed. In addition to air, each material was also tested with heliox.

Results are summarized throughout this report, major conclusions are listed below:

- At dry conditions, no significant difference of performance was found among MPLs. The fuel cell performances are mainly dominated by their HFRs and their interfacial contacts. In these conditions, little liquid water were expected to be saturated in the diffusion media, including MPLs and DMs, thus the effects of mass transport resistance due to the flooding in diffusion media on fuel cell performances were very minimal. Modeling and heliox results confirmed this, thus, a single-phase model can be appropriate for these conditions in the future. Computational simulation revealed that anode/cathode MPL and/or DM asymmetry can potentially protect anode from dryout and promote removal at cathode, since it can be used to alter predicted temperature levels and gradients. *This is a useful area for future work to affect the high temperature operation*
- Net water drag coefficient was derived based on water transport value from anode to cathode. All the MPL materials have a similar and small net water drag coefficient for the same conditions, which ranged from 0.023 to 0.049 in FA conditions.
- Among the MPLs, the less hydrophobic MPL (50 GK) was found to be most sensitive to flow stoichiometry at both dry and wet conditions, while least sensitive to the RHs, especially at high RH range.
- For a thick DM configuration, most of the internal temperature profile occurs though the macro portion, minimizing the impact of the thinner MPL and CL sections. This also has the effect of reducing the thermal bias from the channel/land configuration, which can be beneficial in durability, mass distribution, and start-up shut down as well. When the macro DM is reduced in thickness (or has a high relative thermal conductivity), the MPL and CL thermal properties become much more important, and greater impact should be achieved by tailoring their properties. With macro DM with high thermal resistance, very little impact can be achieved through the CL and MPL thermal property adjustment. However, as the macro DM becomes thinner, as is the trend, the thermal properties of the CL and MPL as well as the interfacial properties will all begin to become important and perhaps dominate inside the PEFC.
- A temperature inversion phenomenon was predicted for a channel / land configuration. In a wet condition, due to flooding under the lands, the hottest location becomes that under the channel due to the majority of reactant availability and hence reaction in this location. However, under dry conditions, the area under the channel becomes too dry and the activity under the land is higher, driving up temperature in this location. Considering that automotive applications are likely to experience both conditions from start-up through steady-state, this bias needs to be considered in terms of durability and design when a conventional channel/land configuration is used. If a thick DM with high in-plane conductivity is used, much of this bias can be eliminated, however.

- MPL sets with lower thickness, higher thermal conductivity and higher porosity are consistently predicted to give better performance.
- MPL thickness is the strongest parameter with an influence that grows with current. Thinner is better for all cases wet and dry due to mass transport. (note: symmetric cases only).
- High thermal conductivity becomes critical for higher current, high temperature, dry conditions but is nearly insignificant at low current. This is an excellent result for design since it means it can be used to tailor high temperature operation but not effect start-up in a significant manner.
- In wet conditions, a *low* MPL thermal conductivity is desired at high current.
- Porosity and through plane permeability only becomes critical at high current wet conditions and are generally not important factors in the range of parameters examined.
- In general, we found for all wet and dry environments, as would be experienced in an automotive operation, thin MPL and DM are good for heat *and* mass transport. A high thermal conductivity material is best as it is critical at high current low RH conditions but has little impact at wet conditions. For wet conditions, a high porosity, high permeability MPL is useful as it has a small impact on normal and high temperature conditions, and improves performance during a wet start-up.

Section 2

Tasks included in this section:

Literature Review

MEA Alternative Concepts Generation and Process Design

The fundamental approach was to evaluate in-line, direct coating processes to form full-width electrode-membrane-electrode (3 layer MEA) products. Such direct coating processes can efficiently produce MEAs at high speed, at low cost and at high volume because they can be scaled to very wide widths, may eliminate sacrificial supporting films or backing layers and eliminate intermediate process handling steps.

This task involved an iterative process in which alternative strategies for MEA processing were considered utilizing existing MEA components as building blocks to evaluate a process for MEA manufacturing. Evaluation of each potential concept included coating technique, coating substrate and coating media (solutions or mixture). Successful lab prototypes were screened initially for power density and effectiveness in influencing break-in. Changes in the component compositions or processing methods were then explored in-order to achieve the break-in and power density goals. The most promising samples were then characterized with respect to the MEA durability targets.

Low-Cost Backer

New low cost backers were required by the processes that are developed in MEA Alternative Concepts Generation and Process Design. Backers were selected to cost as little as possible or be reusable in order to minimize the final cost of the MEA.

Power Density

Beginning of life polarization curve testing at a series of automotive fuel cell relevant conditions using at least two different types of gas diffusion media. High-throughput automated electrochemical diagnostics such as cyclic voltammograms, electrochemical impedance spectroscopy, and He/O₂ were used to obtain further understanding of polarization losses when polarization curves indicate significant changes in MEA performance.

Break-in Performance

Characterized break-in using current or improved protocol

Durability Performance

Characterized mechanical durability (in RH cycling testing) using current or improved protocol

Characterized chemical durability (in OCV hold testing) using current or improved protocol.

Stack Testing

Single-cell (system compatibility check) and/or multi-cell stack(s) (stack validation).

Executed a stack test plan with respect to the project objectives to evaluate. MEAs made by the current process and MEAs made with alternative processes for break-in time, performance, and durability.

Process/Product Down-Selection

Utilized all testing results – break-in, durability, BOL, model output and cost to choose best concepts.

Designed a laboratory scale continuous rolled good MEA fabrication process.

Specified any additional equipment required for 3-layer rolled good scale-up, test at outside vendors as required, and purchase equipment.

Set-up lab coating equipment and/or coat/test at outside vendors as required.

Process/Product Optimization via Continuous Lab-Scale Coating

Explored process parameters and fabricate prototypes.

Tested lab-scale continuously produced prototypes against performance target (break-in and power density).

Performed durability tests on most favorable prototype.

Re-evaluated the cost model with the learning of the in-line prototype evaluation.

During the first stages of this work, a primary and alternative process path were identified utilizing the results of the literature review in conjunction with Gore's internal coating expertise.

- Primary path
 - Direct coated cathode on a backer-supported reinforced membrane
 - Direct coated anode on 2-layer intermediate
- Alternate path
 - Direct coat anode on supported ½ membrane
 - Direct coat cathode on supported ½ membrane
 - Bond the membrane-membrane interface of the 1.5 layer webs to make a 3-layer web

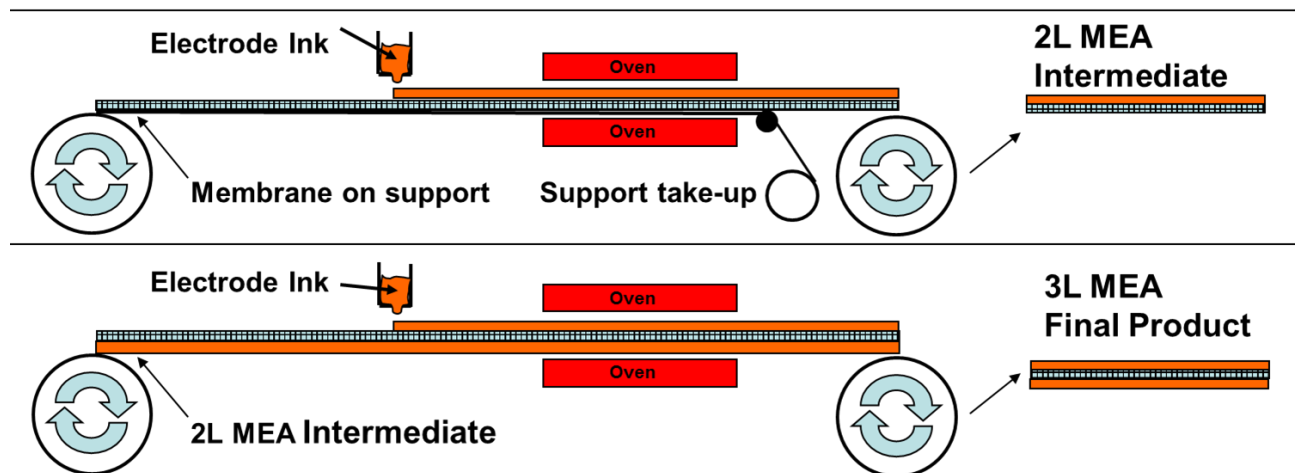


Fig 36a) Primary path process schematic

Although early direct coated cathodes demonstrated very poor performance, further experiments improved performance to the point where direct coated cathodes were comparable to the current commercial cathodes in saturated and sub-saturated operating conditions.

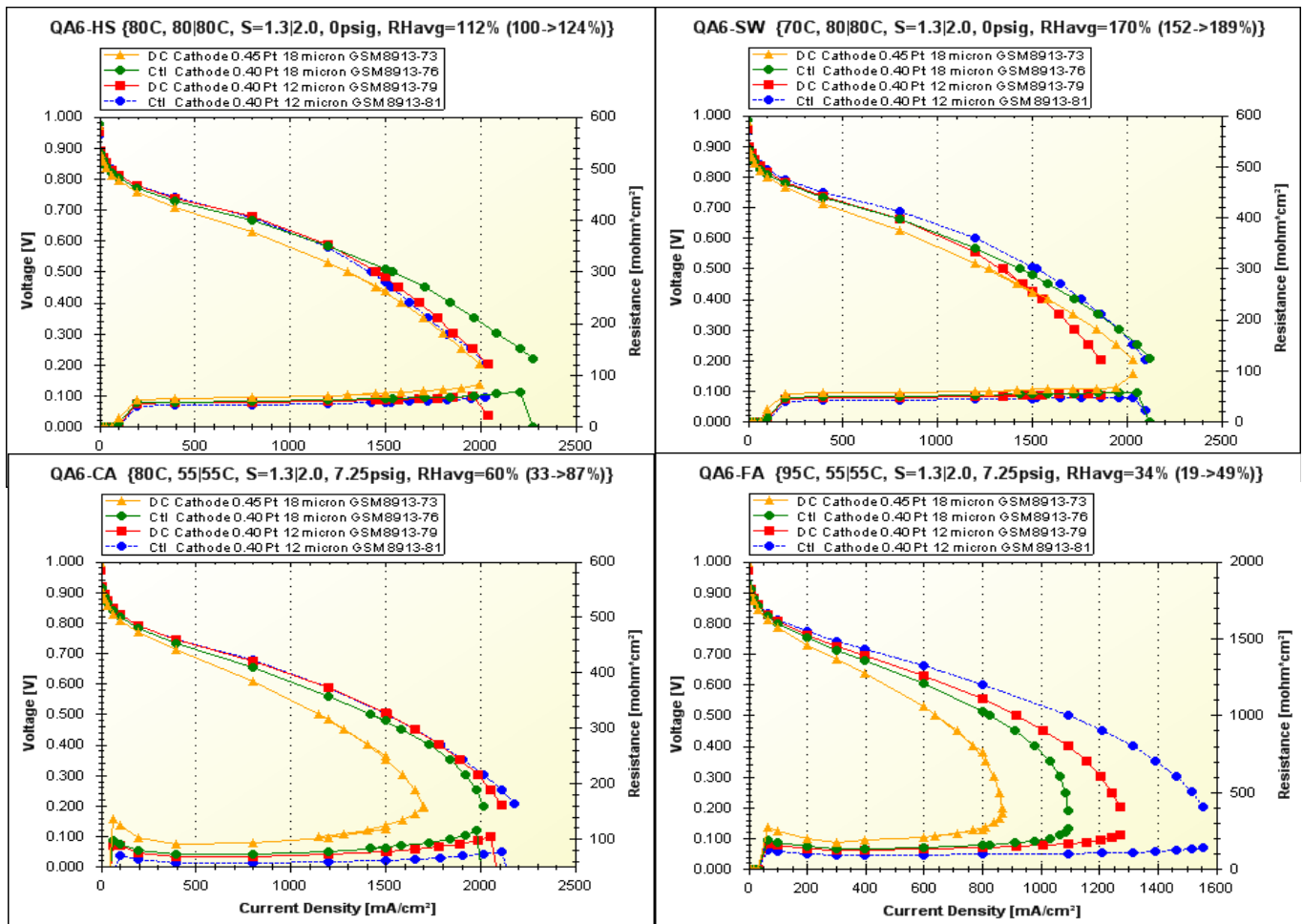


Figure 36b: Early direct coated cathodes demonstrated very poor performance (gold triangles)

Cathode electrochemical diagnostics were used to understand how polarization losses in direct coated cathodes differ from the current commercial cathodes.

- Standardized protocol combined BOL robustness testing with key cathode diagnostics at wet and dry conditions
- Test summary
 - **Pre-Conditioning Diagnostics**
 - Cleaning Cyclic Voltammograms (CVs)
 - CV, H2 Cross-Over, Electrochemical Impedance Spectroscopy (EIS)
 - **Conditioning**
 - **Saturated and Super-Saturated Performance**
 - Polarization Curves, Current Interrupt Resistance, and Stoich Sensitivity
 - **Saturated Diagnostics**
 - He/O2, O2 Tafel
 - CV, H2 Cross-Over, EIS
 - **Sub-Saturated and Hot Sub-Saturated Performance**
 - Polarization Curves, Current Interrupt Resistance, and Stoich Sensitivity
 - **Sub-Saturated Diagnostics**
 - He/O2, O2 Tafel
 - CV, H2 Cross-Over, EIS

Upon further iteration, direct coated anode/membrane 2L and cathode/membrane 2L constructions were developed in line with the primary path and both demonstrated reasonable un-optimized performance.

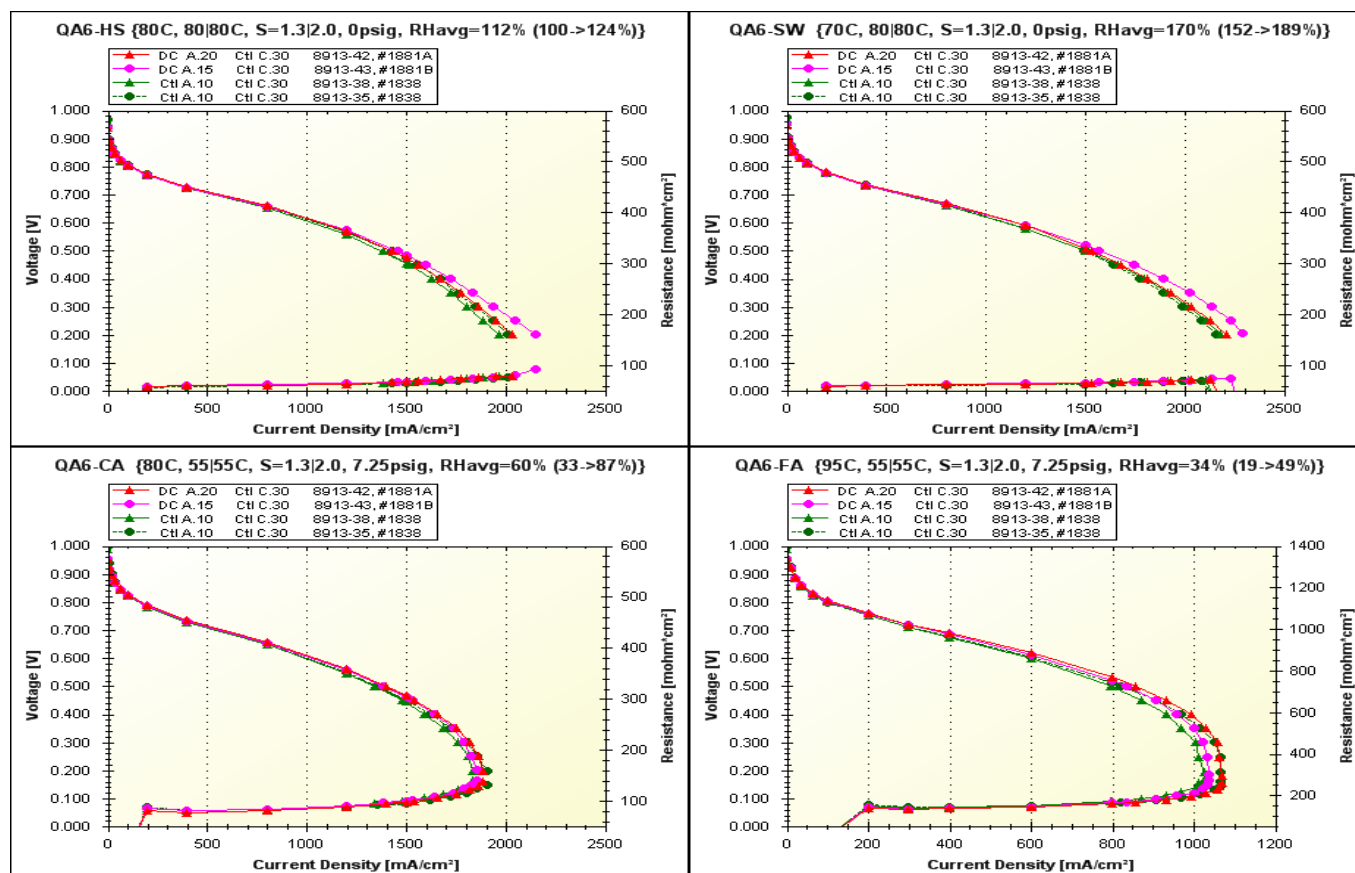


Figure 37: Performance of an MEA made with DC anode is comparable to a commercial control MEA. Due to early process challenges, DC anode Pt loadings were higher than the current commercial control anode in this data set.

Observations made during the coating of the 2-layer constructions led to a significant change in the alternate path process. Instead of coating electrodes on to a ½ membrane which is supported by a carrier film, a lower-cost process which only requires 1 carrier film for the entire process was developed. This allowed for the MEA in the new alternate path process to be fabricated from the bottom up, starting with a low-cost, non-porous backer web.

Figure 38 summarizes beginning-of-life (BOL) performance for MEA's made with commercial (control) cathode electrodes and experimental anode electrodes. The anodes in this data set were coated onto either a reinforced membrane (primary path, coating method 1) or a carrier film (alternate path, bottom-up coating methods 1 and 2). All three approaches provide MEA's which meet or exceed the BOL performance of the current commercial MEA across a variety of operating conditions.

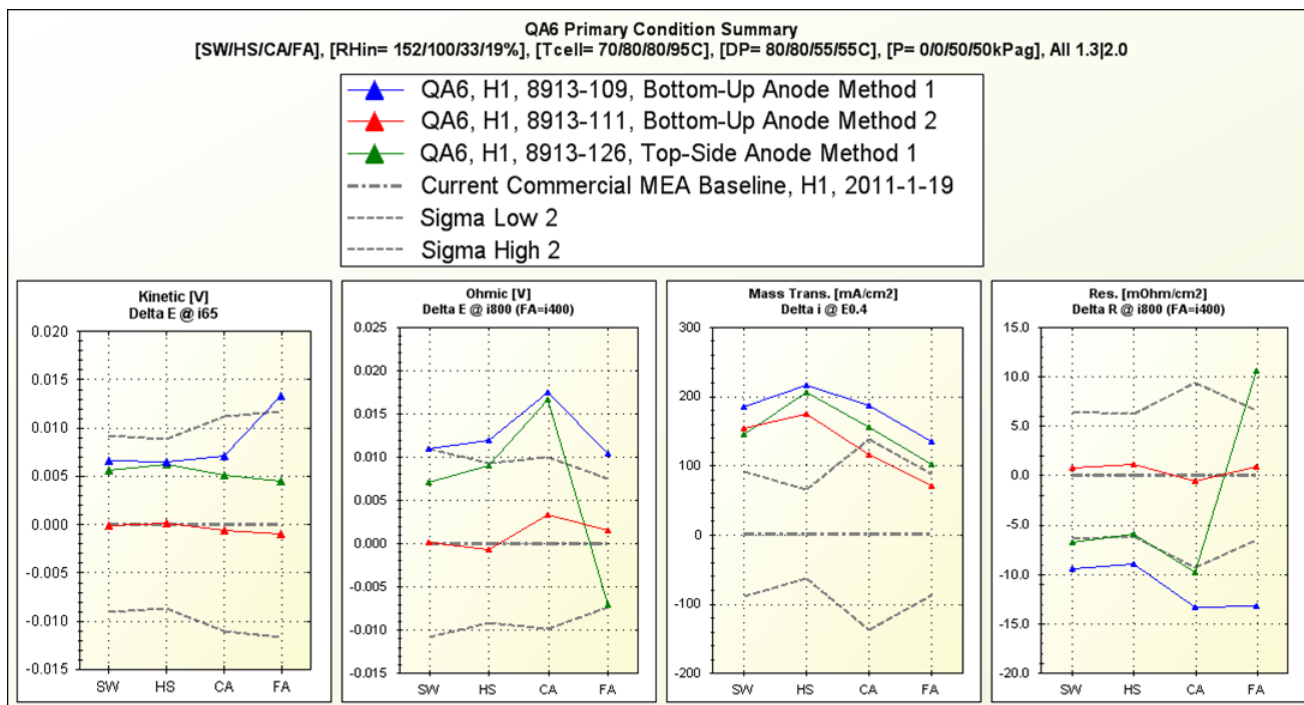


Fig. 38 QA6 BOL performance summary for experimental anode electrodes

Figure 39 shows high-resolution pol curve data for the 80°C cell temp / 80°C anode and cathode dew point operating condition (100% saturated inlets). Performance of the experimental anode MEAs in the high-current density region of the pol curve clearly exceeds the 2-standard-deviation limits of the baseline. The intimate interfaces formed by direct coating are hypothesized to be the cause of the performance improvement.

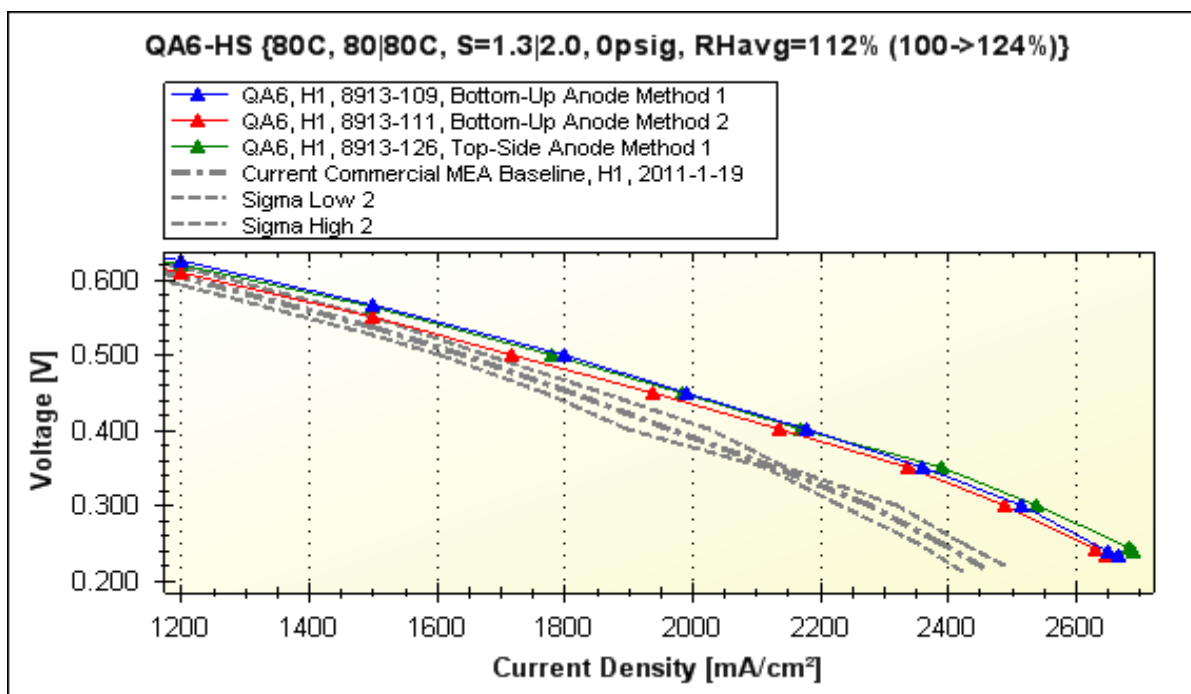


Fig. 39 QA6 BOL pol curve for experimental anode electrodes

Figure 40 summarizes beginning-of-life (BOL) performance for MEA's made with current commercial (control) anode electrodes and experimental cathode electrodes. The cathodes in this data set were coated onto a carrier film (alternate path, bottom-up coating methods 1 through 4). All four approaches provide MEA's with performance close to that of the current commercial MEA, but only the MEA made by method 4 is consistently within the 2-standard-deviation limits.

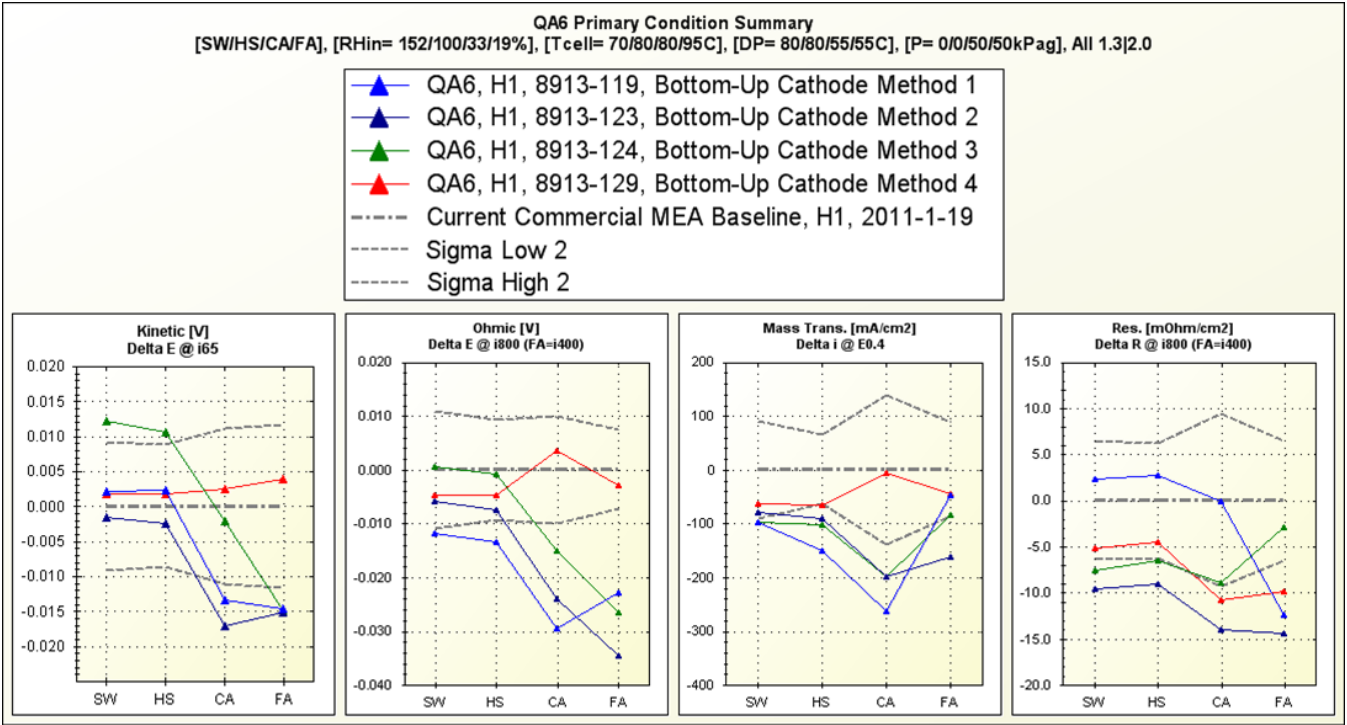


Fig. 40 QA6 BOL performance summary for bottom-up cathode electrodes

Figure 41 summarizes beginning-of-life (BOL) performance for MEA's made with current commercial (control) anode electrodes and experimental cathode electrodes. The cathodes in this data set were direct-coated onto a reinforced membrane (primary and alternative paths). Methods 1 and 2 provide MEA's with excellent performance in dry operating conditions and performance close to that of the current commercial MEA in operating conditions with saturated and supersaturated inlets.

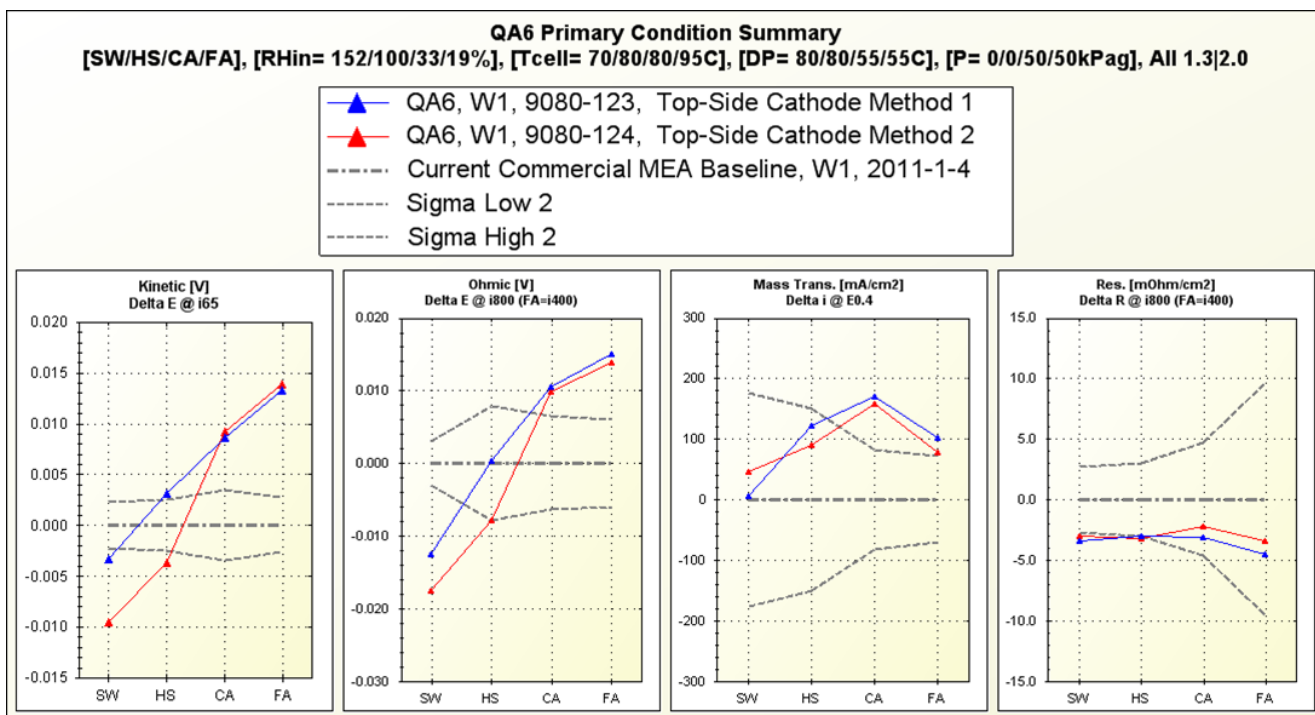


Fig. 41 QA6 BOL performance summary for top-side cathode electrodes

Subsequent efforts focused on understanding the interactions between cathode ink formulation and low-cost backer for a process in which the cathode is the first layer to be coated in the 3-layer MEA. MEAs used in BOL testing were constructed by bonding the experimental cathodes to a ~10 micron reinforced membrane and commercial anode electrode. Fig 42a shows an example of a cathode coating in progress and Fig 42b shows the profound effect that solvent/backer interactions can have on performance, particularly in the high current density region of the pol curve.

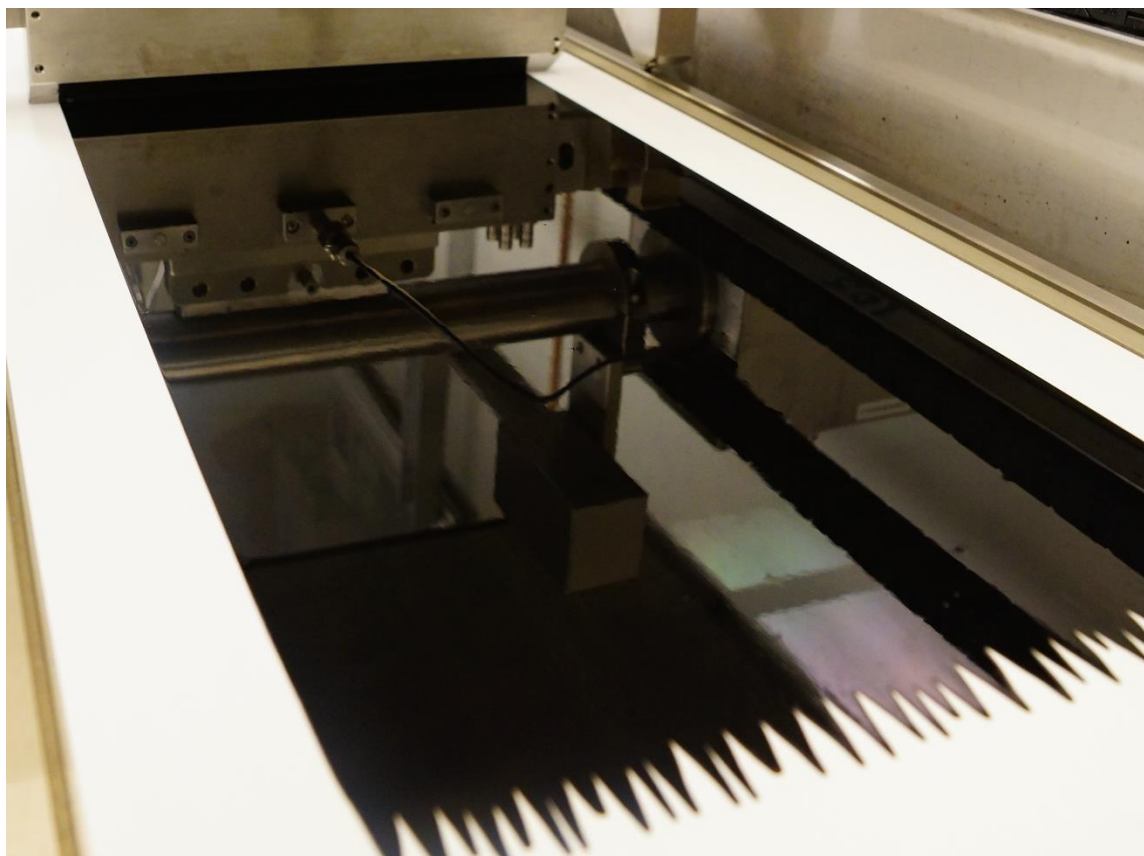


Fig. 42a: Cathode coating on low cost backer

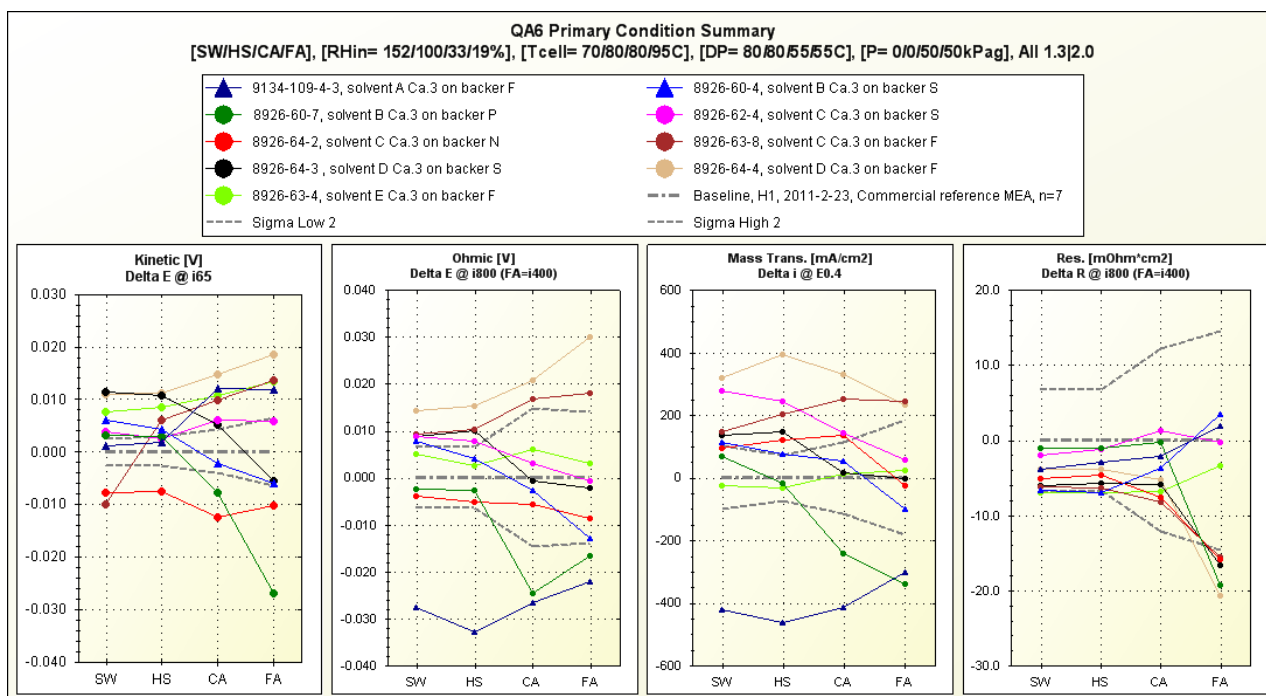


Fig. 42b QA6 BOL performance summary for experimental cathode electrodes

Figure 43 shows the RH sensitivity of the new experimental cathodes made by coating method 4. Sample 8926-64-4 (solvent D Ca.3 on backer F) maintains the highest performance across the entire spectrum of operating conditions, indicating an improved electrode structure.

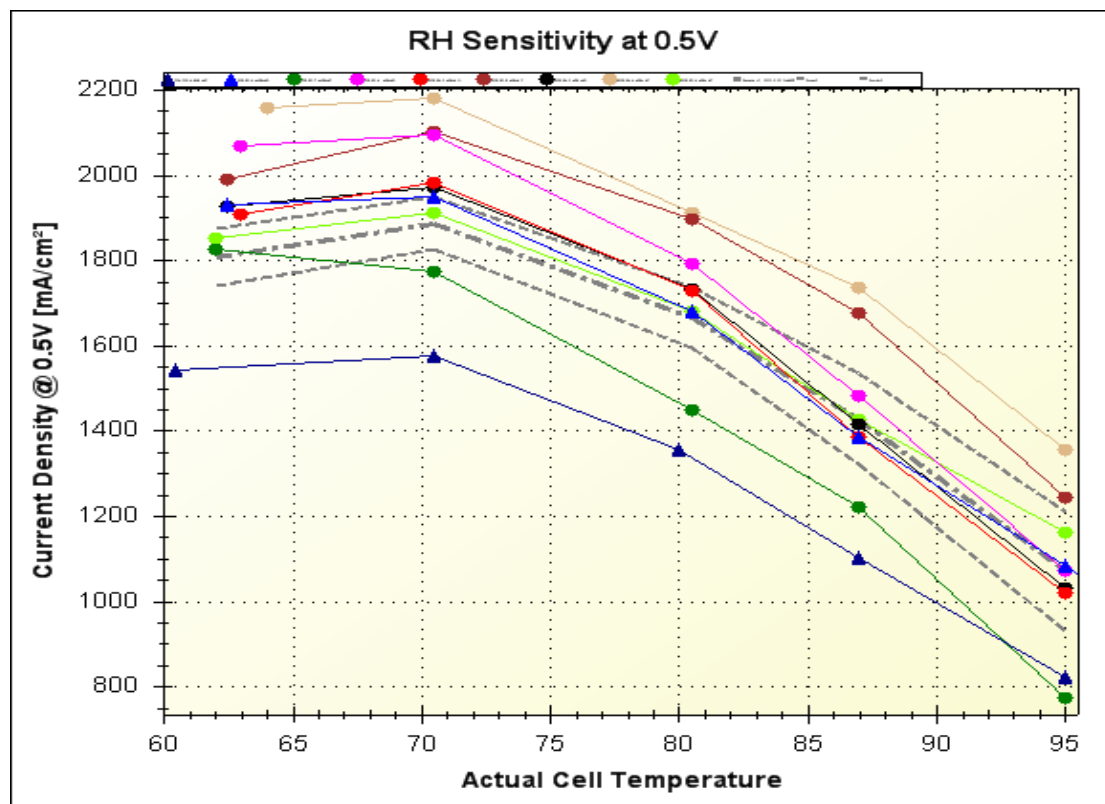


Fig. 43 QA6 RH Sensitivity plot for experimental cathode electrodes (see Fig 42 for legend)

Fig. 44 demonstrates the challenges of refining the bottom-up cathode coating process, as well as the interactions between the cathode layer and the direct coated reinforced ionomer layer, particularly in the high current density region of the pol curve. Sample A represents the most effective combination of a bottom-up cathode and a direct coated ionomer layer. Samples B and C suffer from flooding in saturated operating conditions, although sample B demonstrates excellent high current density performance in sub-saturated operating conditions.

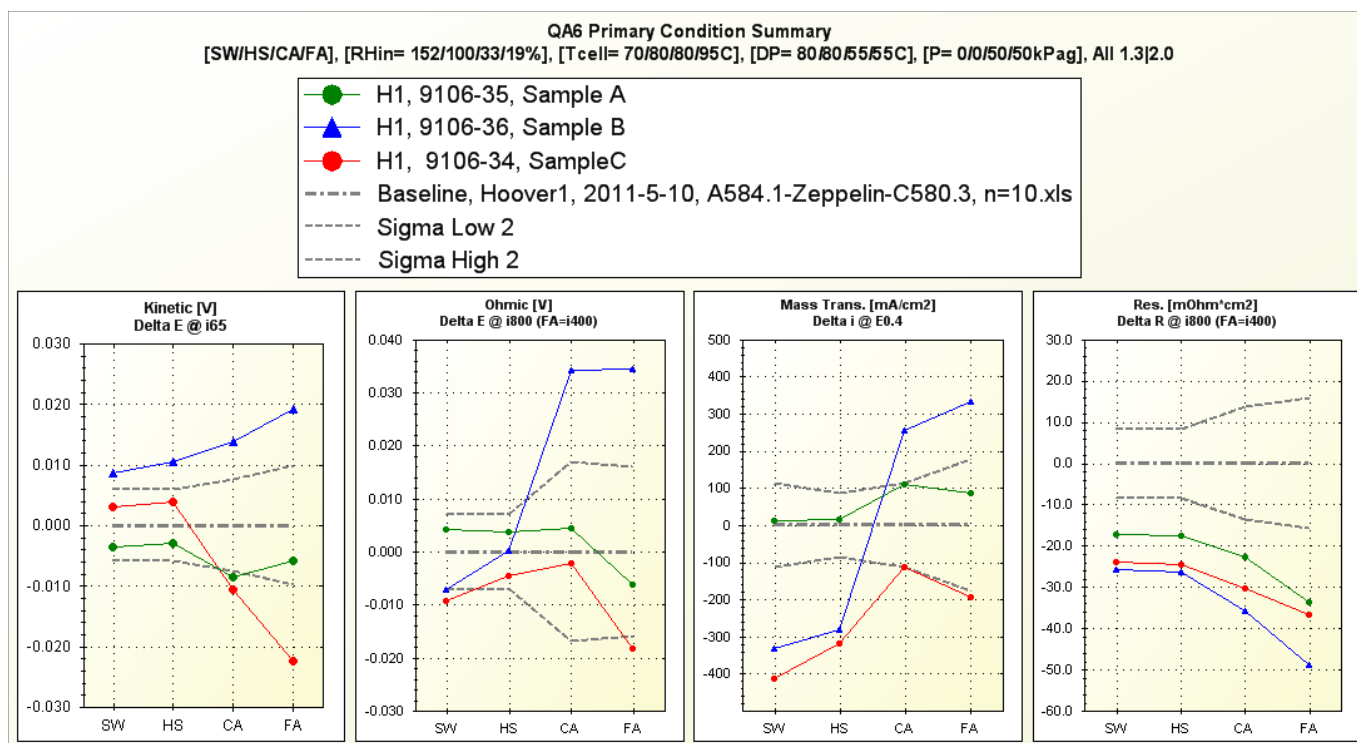


Fig 44. QA6 BOL performance summary for new experimental MEAs made by the bottom-up process (control anodes used for all 3 samples)

Subsequent work focused on optimizing the anode electrode to improve MEA durability while maintaining robust performance throughout a wide range of operating conditions which an MEA may encounter in transient operation. Anode electrode ink components such as catalyst, ionomer, and solvent were varied in a series of designed experiments.

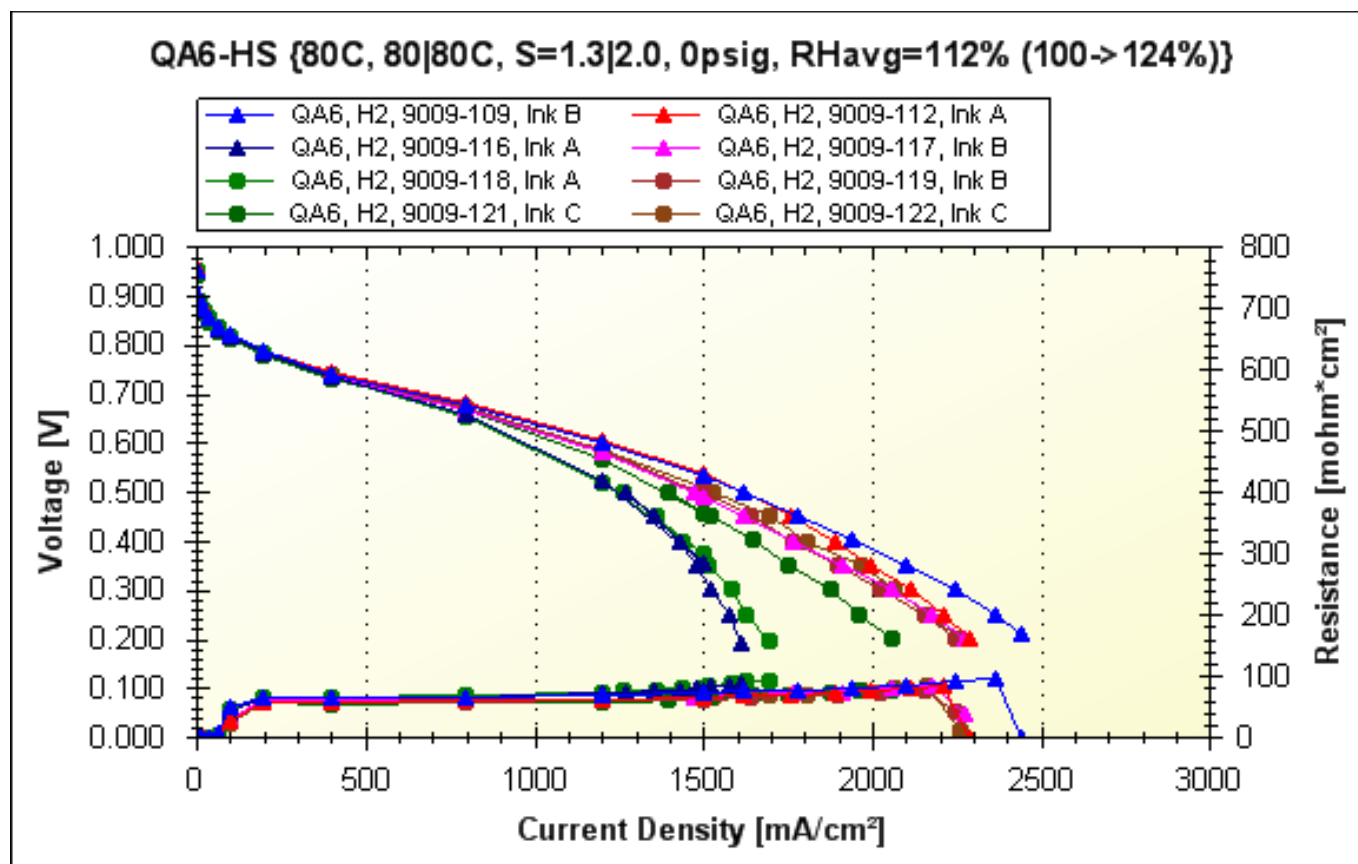


Fig. 45 HS condition BOL performance pol curves for experimental anode with control membrane and cathode

Figures 45 and 46 depict BOL performance of MEAs made with new electrode ink formulations. Kinetic performance is consistently good, but high-current-density performance varies significantly from sample to sample. These results are attributed to variation in the sheet-coating lab-scale process.

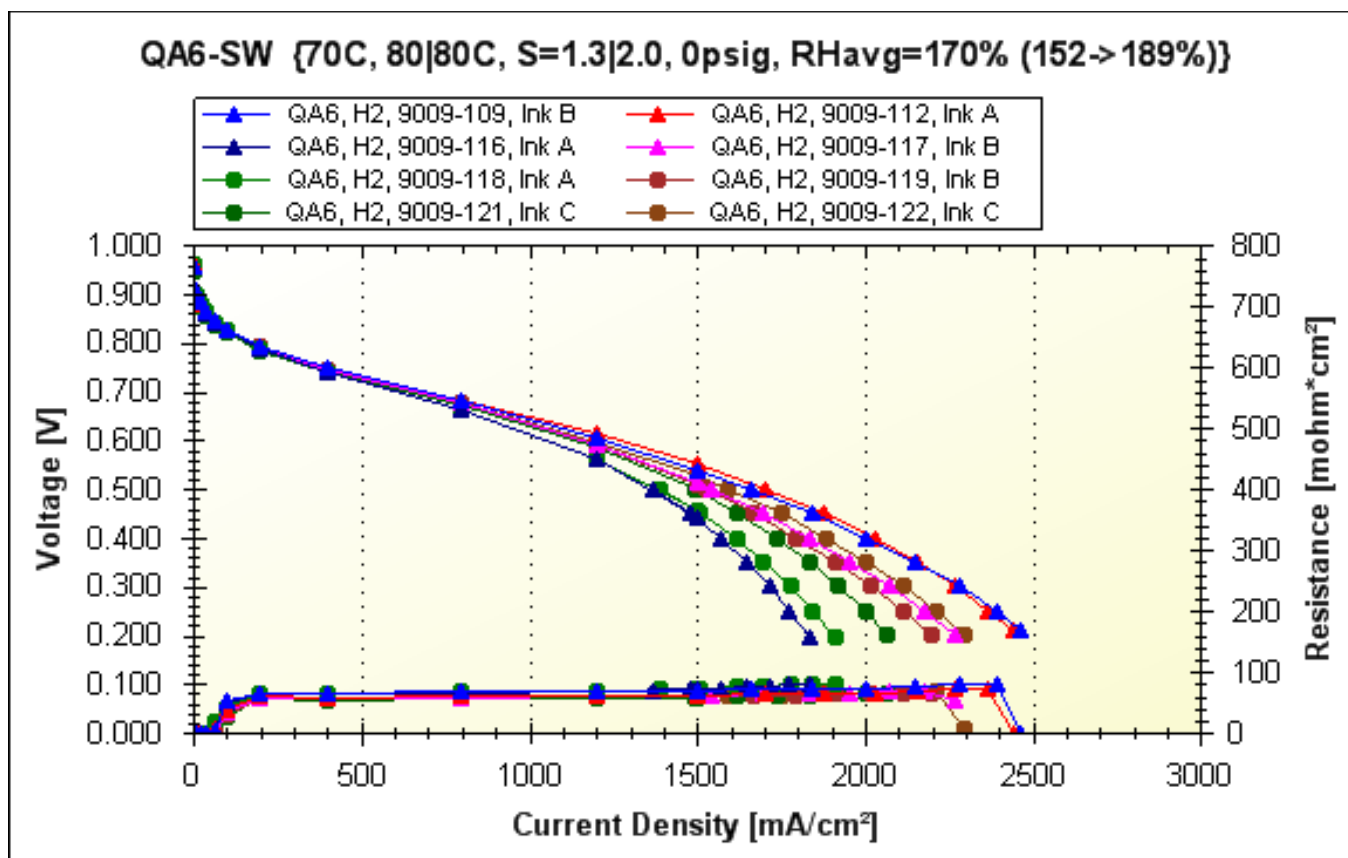


Fig. 46 SW condition BOL performance pol curves for experimental anode with control membrane and cathode

Figures 47 and 48 depict BOL performance of MEAs made with new electrode ink formulations. In the higher temperature, lower RH operating conditions of CA and FA, there is less variation in high-current-density performance. The contrast between wet and dry operating conditions suggests that some of the experimental anodes may be prone to flooding in wet conditions. It is possible that membrane ionomer was dissolved during the anode coating process, thereby increasing the effective ionomer:catalyst ratio of the anode electrode.

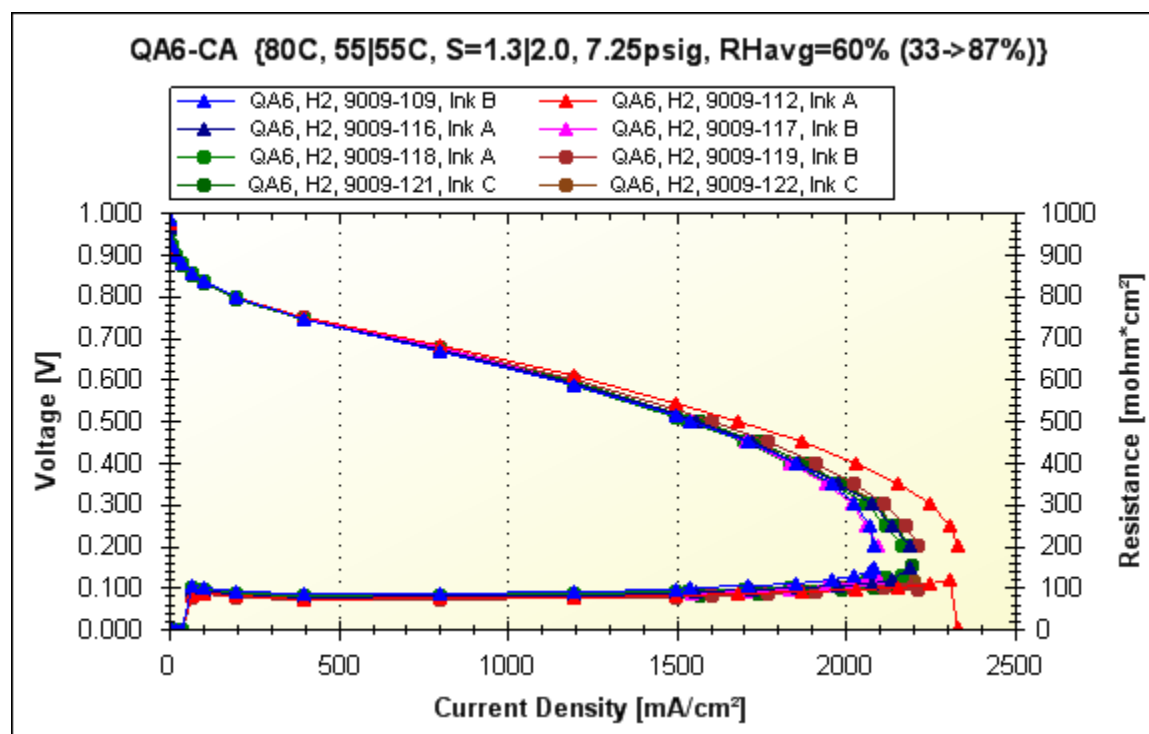


Fig. 47 CA condition BOL performance pol curves for experimental anode with control membrane and cathode

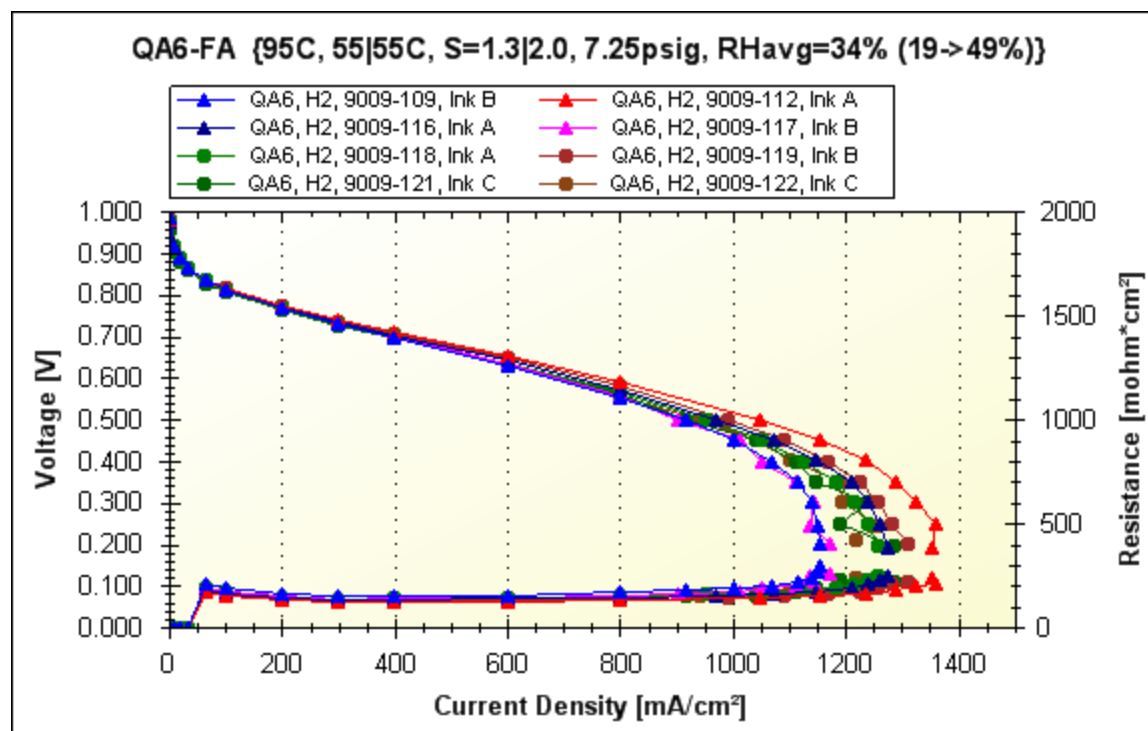


Fig. 48 FA condition BOL performance pol curves for experimental anode with control membrane and cathode

Figure 49 compares the start/stop cycling voltage decay rate of the MEAs made with experimental anodes to the control MEAs. All of the experimental anode ink formulations impart a significant improvement to the durability in start/stop cycling.

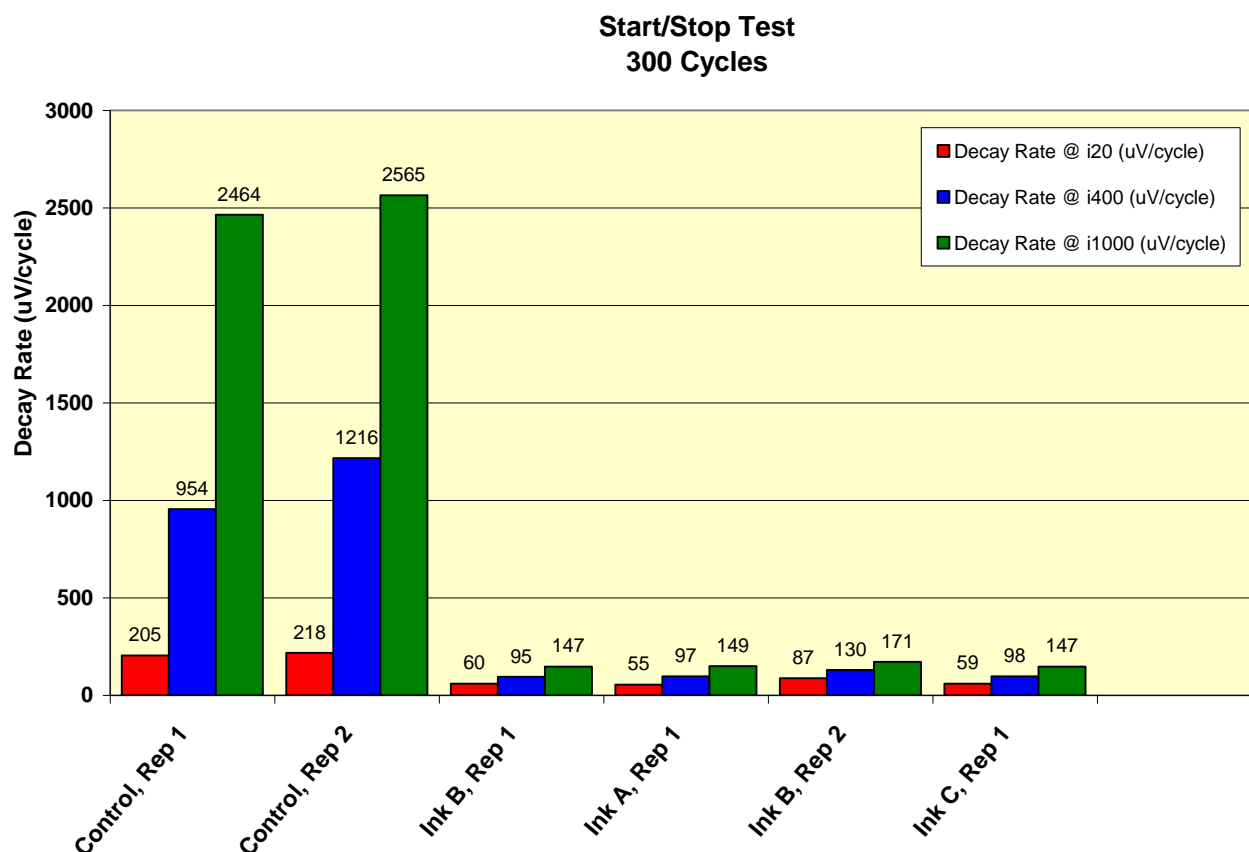


Fig. 49 MEA durability impact of experimental anode with control membrane and cathode

Due to suspected process variation inherent in small scale sheet coating, continuous coating trials on a pilot coating line were planned and executed. Studying the effect of drying conditions on the cathode electrode built on previous experiments in which the cathode electrode was patch coated and hand dried.

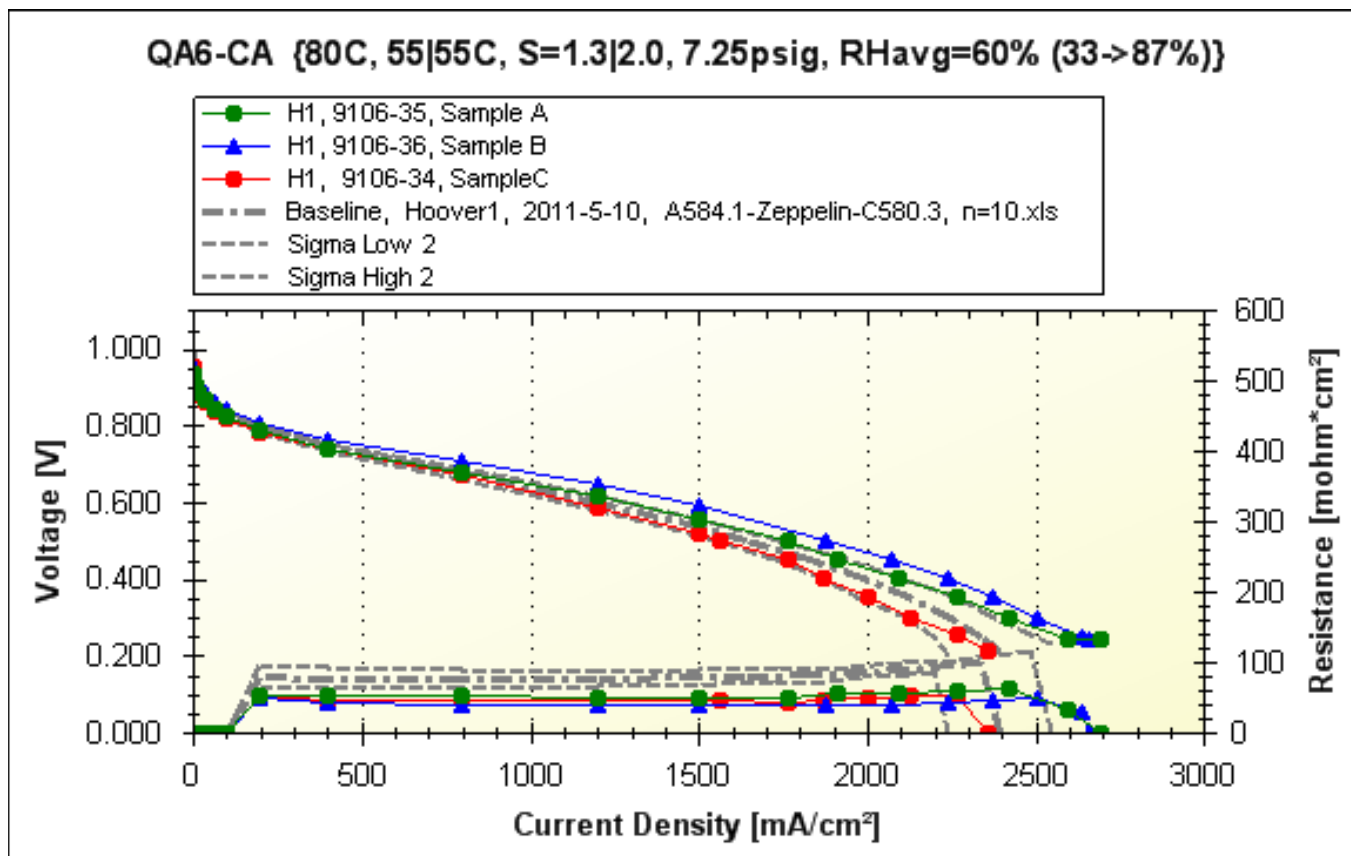


Fig. 50 CA condition BOL performance pol curves for sheet-coated experimental cathode with control anode

Figure 50 shows high-resolution pol curve data for the 80°C cell temp / 55°C anode and cathode dew point operating condition (33% RH inlets). In this set of operating conditions, sample B exceeds the performance of the current commercial control MEA.

Figure 51 shows BOL test results of a pilot scale roll-to-roll cathode coating trial. Drying conditions were identified as the most likely root cause for the difference between the performance achieved in Figure 50 vs Figure 51.

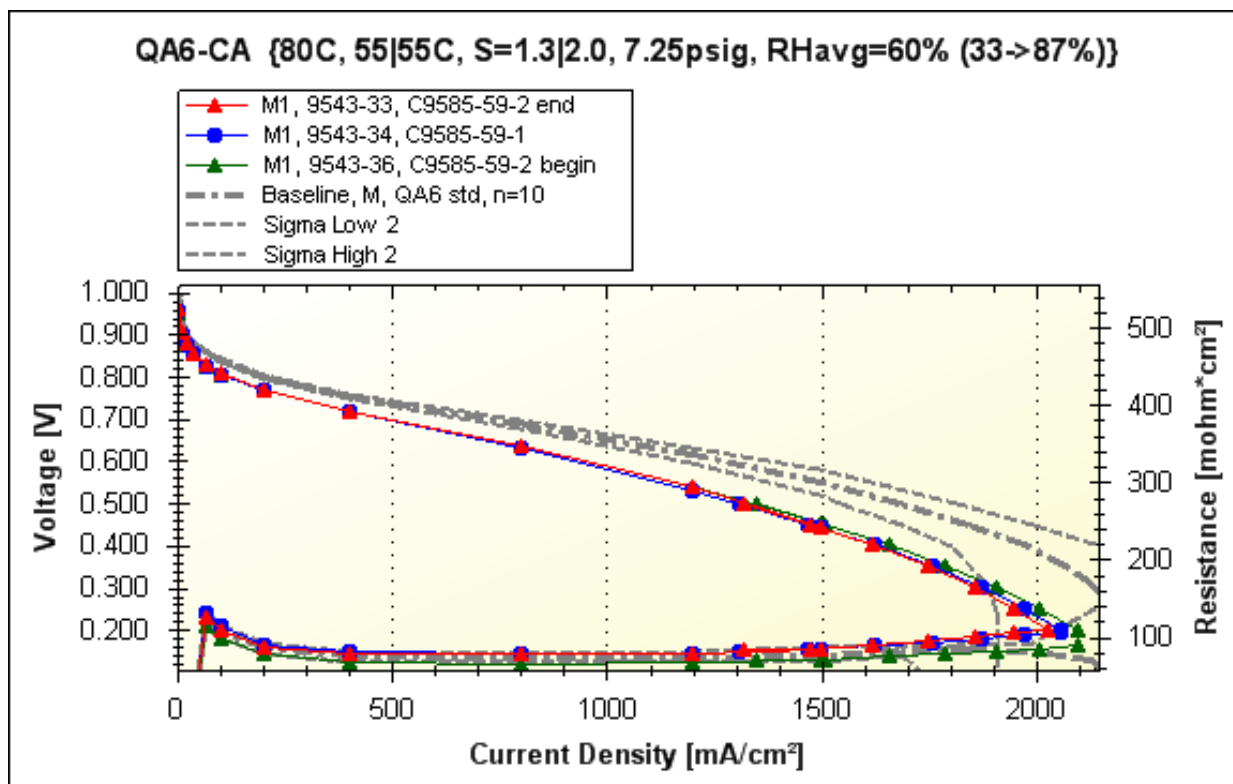


Fig. 51 CA condition BOL performance pol curves for pilot scale roll-to-roll experimental cathode with control anode

Figure 52 shows a summary of BOL results of a pilot scale roll-to-roll cathode coating trial across a wide range of operating conditions. As indicated in the comparison between Figure 50 and Figure 51, the pilot scale roll-to-roll cathode performs lower than the baseline in hotter, drier operating conditions.

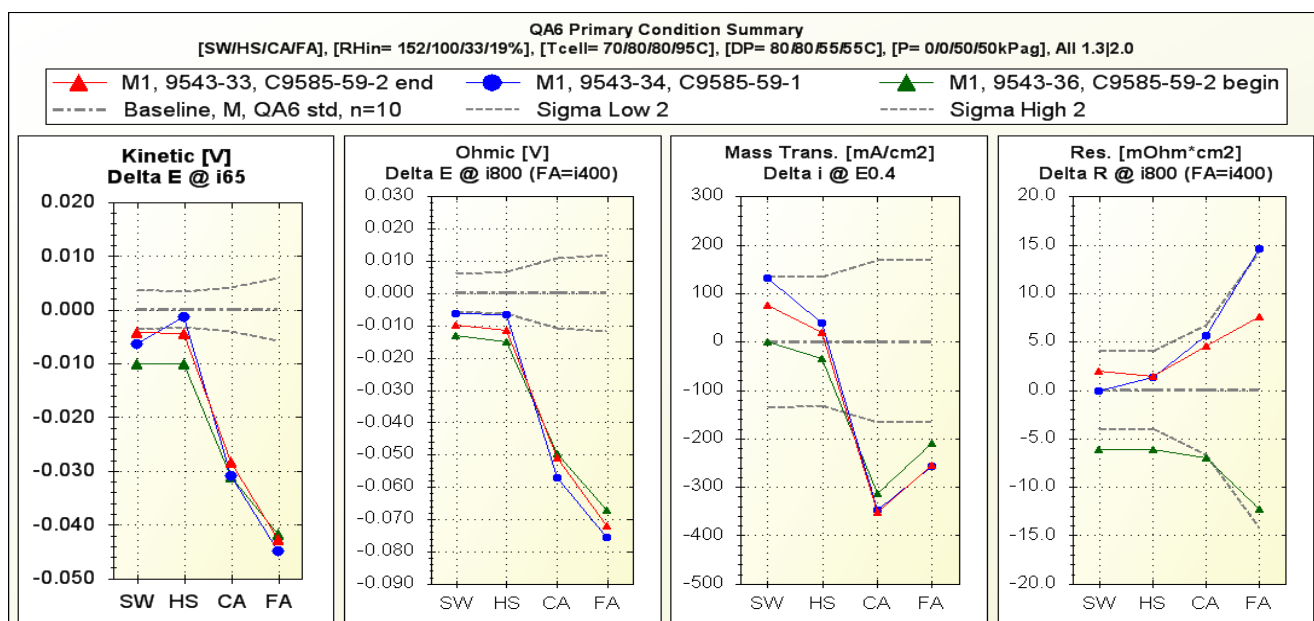


Fig. 52 BOL performance pol curve summary for pilot scale roll-to-roll experimental cathode with control anode

In subsequent work, the sheet coating procedure was modified to utilize a solvent-rated oven capable of approximating pilot scale drying conditions. The problem of low performance in the CA and FA operating conditions was resolved by adjusting the ink formulation for the simulated pilot-scale drying conditions. As shown in figure 53, performance of the MEA made by the adjusted ink formulation is equivalent to the control MEA.

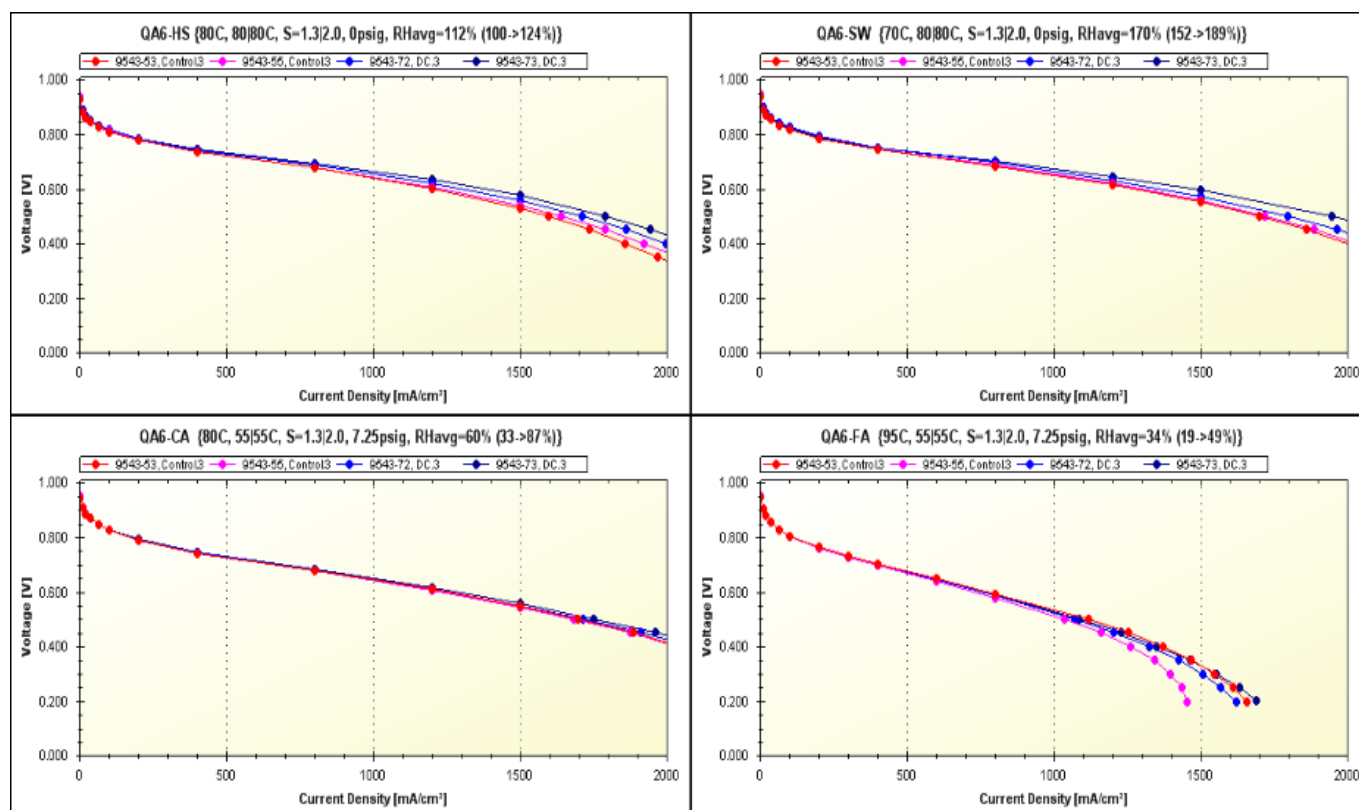


Fig. 53 BOL performance pol curves for sheet-coated oven-dried experimental cathode with control anode

The improved ink formulation was then used in pilot-scale production of the cathode on low-cost backer. Over 50 meters of cathode were coated in a continuous roll to roll process in order to supply substrate for direct coating of membrane and anode electrode. The pilot-line cathode was tested for performance and durability and demonstrated equivalence with the current commercial MEA as shown in figures 54 and 55.

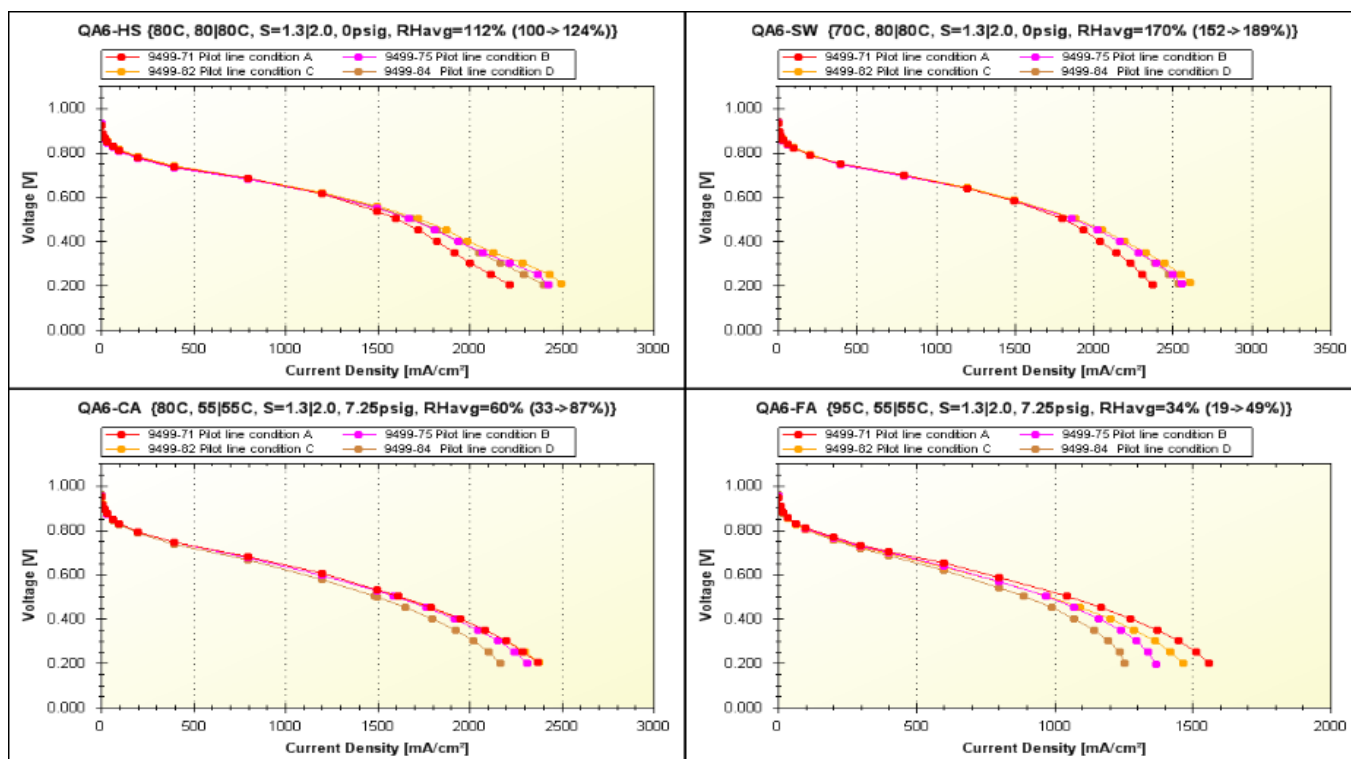


Fig. 54 BOL performance pol curves results for cathode on low-cost composite backer coated on a roll-to-roll process matched with control membrane and anode

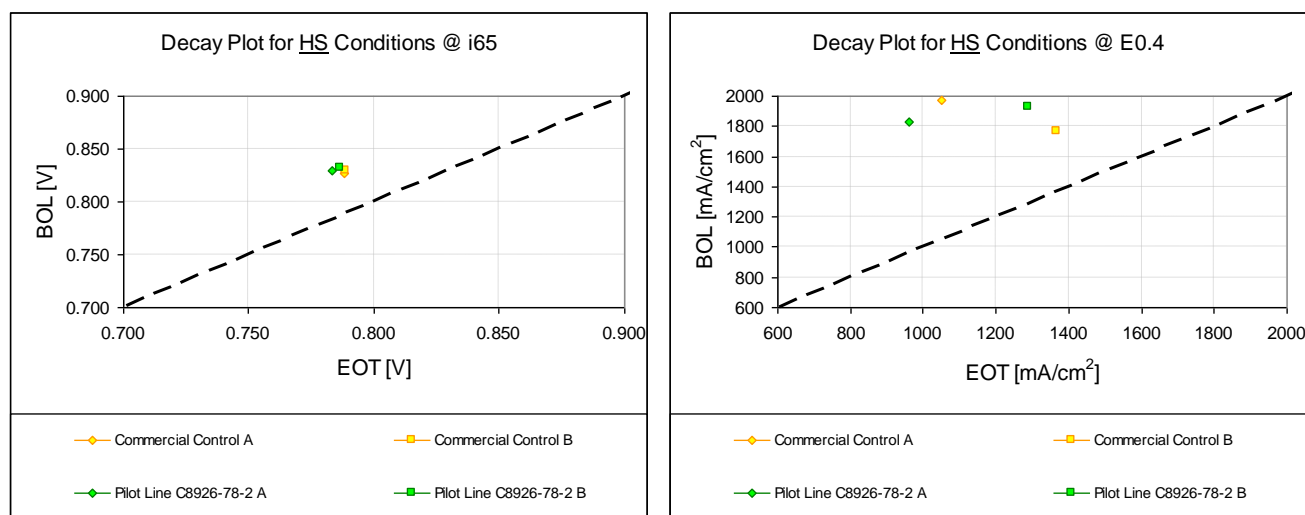


Fig. 55 Voltage cycling durability test results for cathode on low-cost composite backer coated on a roll-to-roll process matched with control membrane and anode.

After the cathode electrode has been coated on the low-cost multi-layer backer, the next step is to form a reinforced membrane directly on the cathode. Figure 56 demonstrates the capability that Gore developed to coat a highly uniform ionomer film on the cathode surface. This sample was coated on a sheet coater which utilized the same type of coating head as the roll-to-roll pilot coating line which was used for cathode coating. As shown in figure 58, this ionomer coating had no negative impact of MEA BOL performance. Given the progress made on the bottom-up coating approach, the process outlined in Fig 57 was selected as the final primary path.

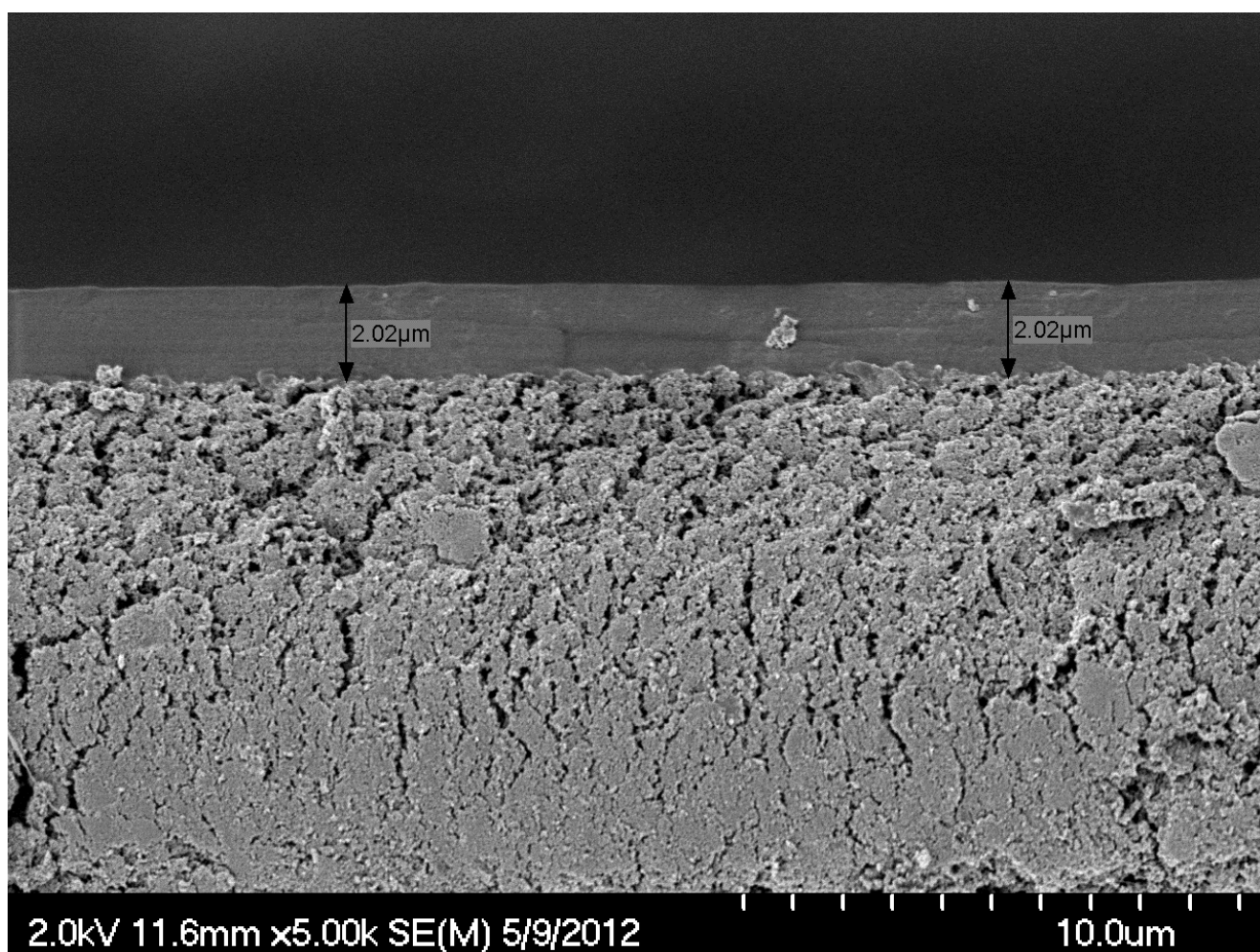


Fig. 56 SEM cross section of highly uniform ionomer layer coated directly on the experimental cathode.

Approach: Low-Cost MEA Mfg Process, Primary Path

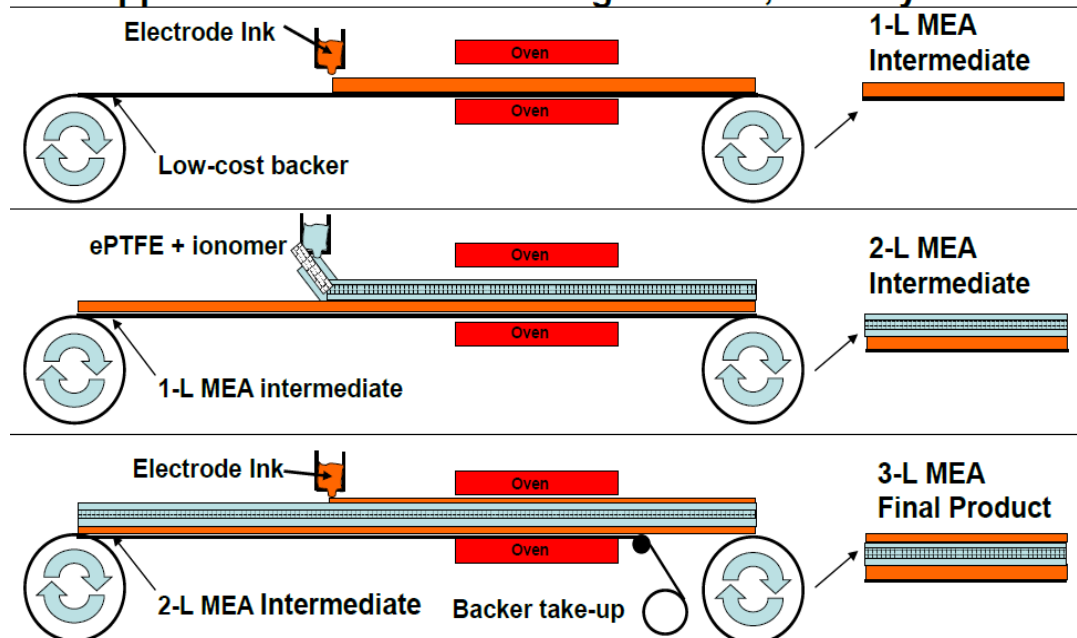


Fig 57: MEA manufacturing process schematic

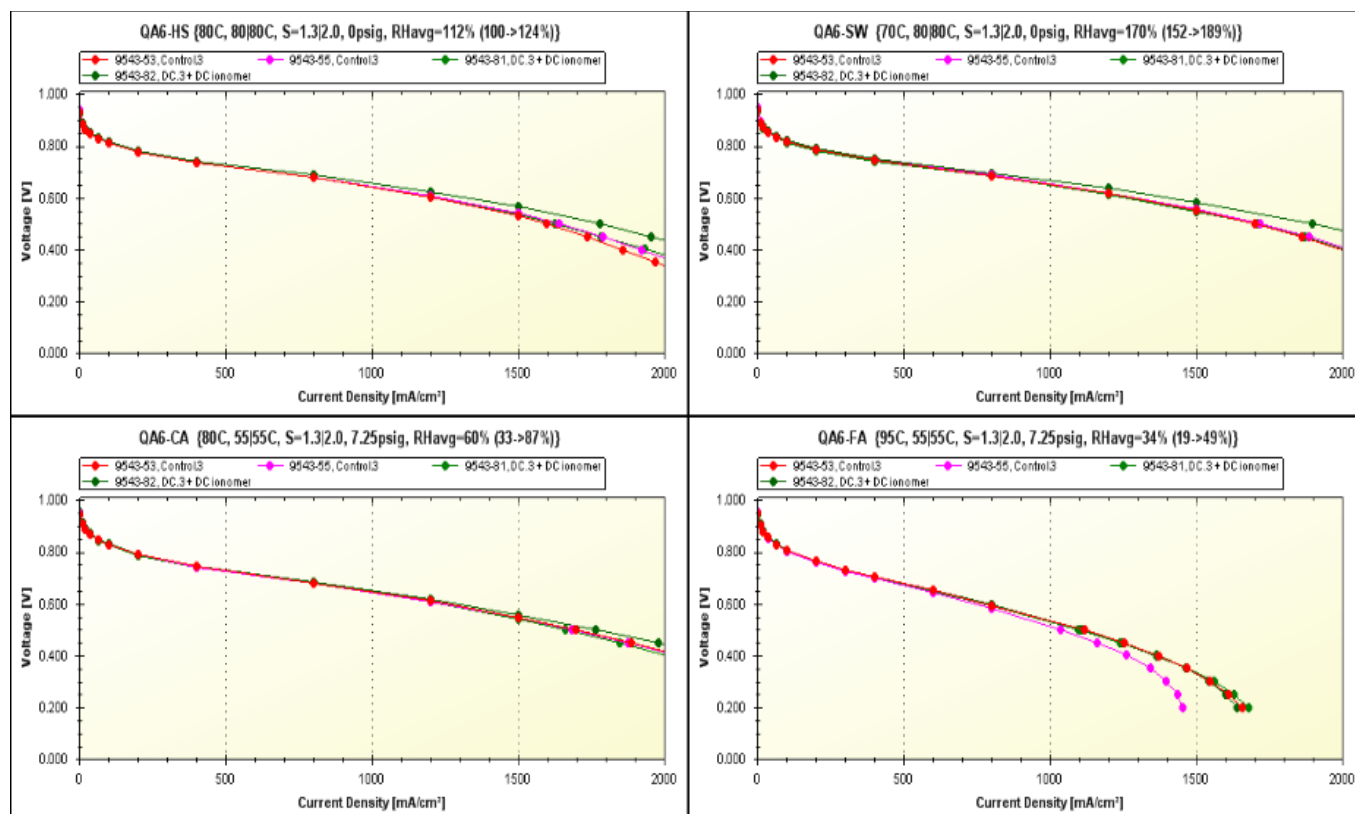


Fig. 58 BOL performance pol curves for experimental cathode with direct-coated ionomer film and control anode

While the small scale ionomer coatings worked well in a lab setting, defects occurred in subsequent pilot line trials. Experiments were executed to investigate alternative ionomer formulations and to provide a deeper understanding of the interactions between low-cost backer, cathode surface structure, and ionomer formulation coating. The results of these experiments indicated an interaction between the low-cost backer and the cathode electrode that was causing the defects in the reinforced membrane coating process. Alternative low-cost backer materials were screened in sheet form and two promising candidates were chosen for roll to roll process trials. The data in figure 59 indicates that one variant achieved the target performance (9585-134-2, black), while the other variant suffered from low performance in all 4 sets of operating conditions.

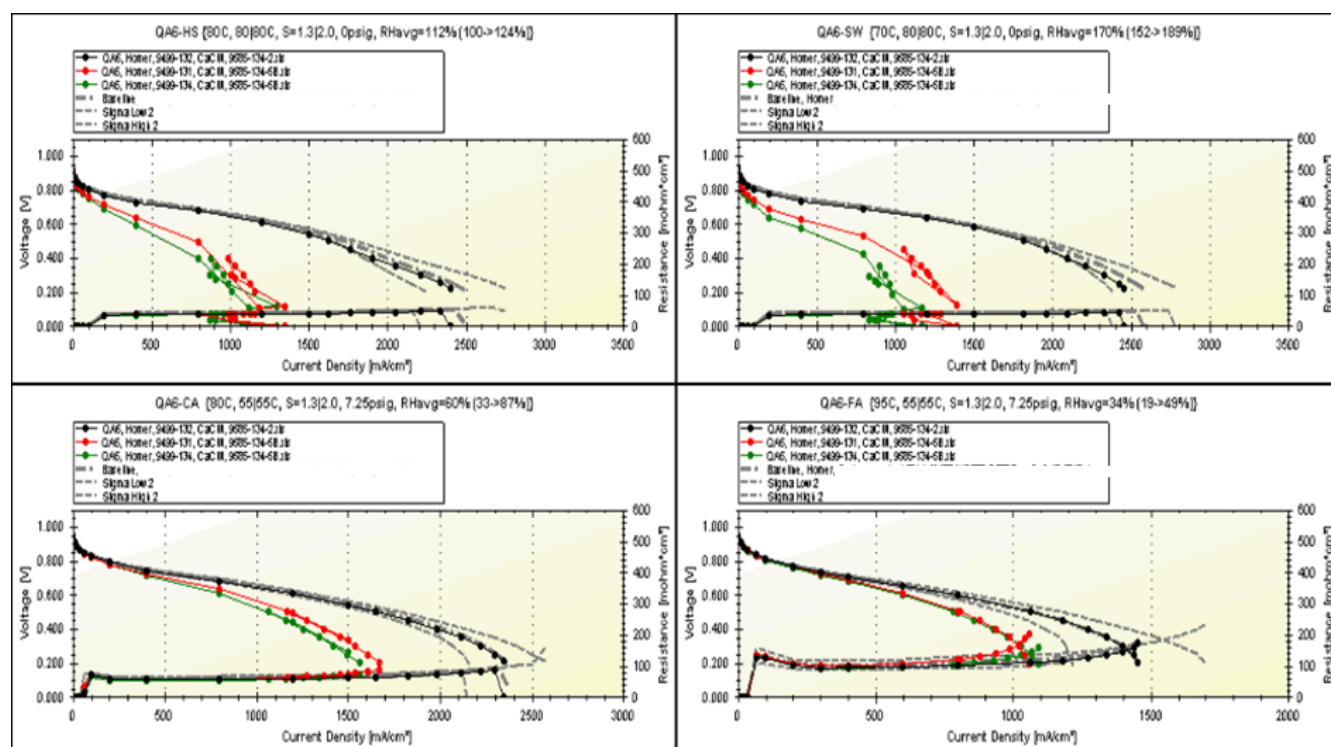


Figure 59: BOL performance of cathode coated on modified backer

BOL testing of the direct coated MEA indicated good performance, but coating defects resulted in a low yield. Further study of coating parameters was executed to reduce the frequency of defects. In parallel, Gore leveraged the results of the heat and water transport model to match the direct coated MEA with an alternative gas diffusion media layer. The results shown in figure 60 indicate the tradeoffs that can be made in wet vs. dry operating conditions by changing the properties of the gas diffusion media.

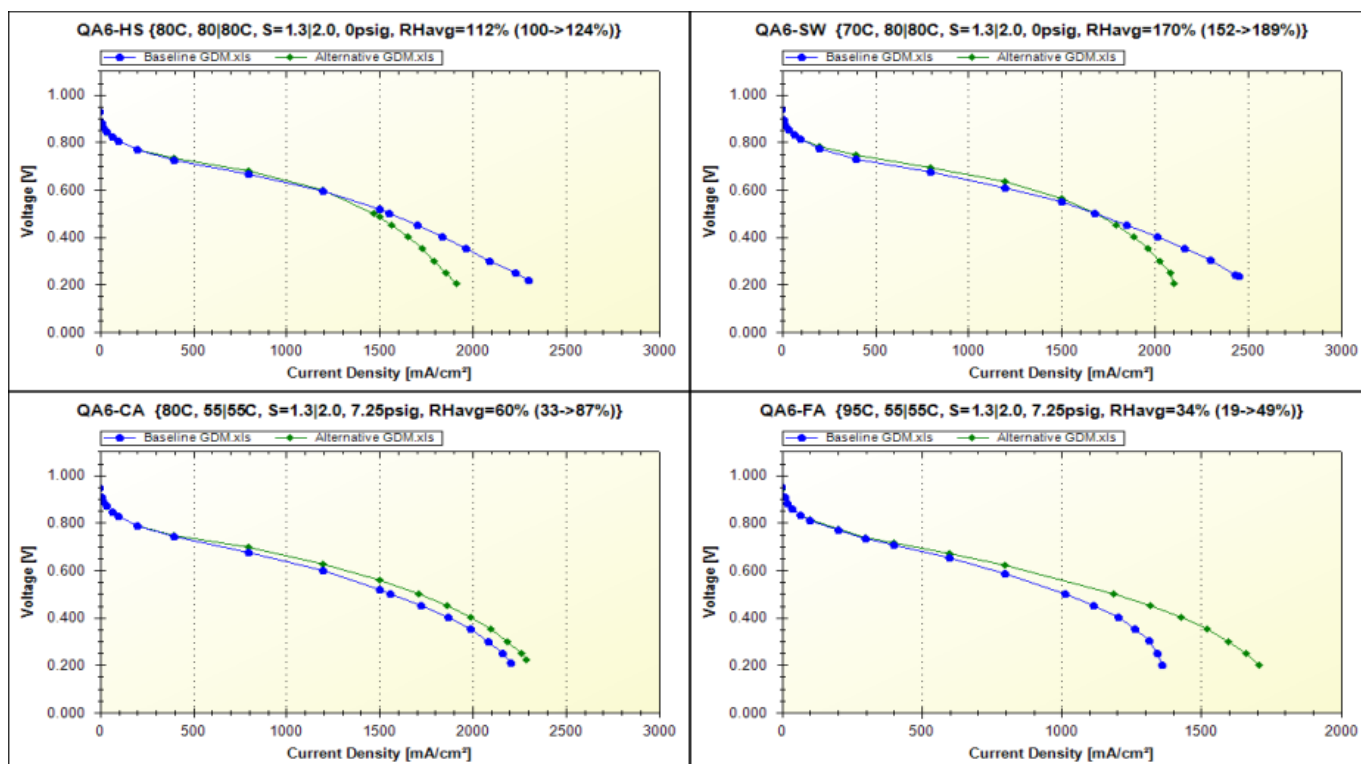


Figure 60: BOL performance of direct coated MEA with baseline and alternative GDM

A series of pilot coating line experiments led to improvements in direct coating yields and the final setting were chosen to provide samples for short stack validation testing. The results of a QC check for the direct coated MEAs provided to UTK for stack testing are shown below in Fig. 61.

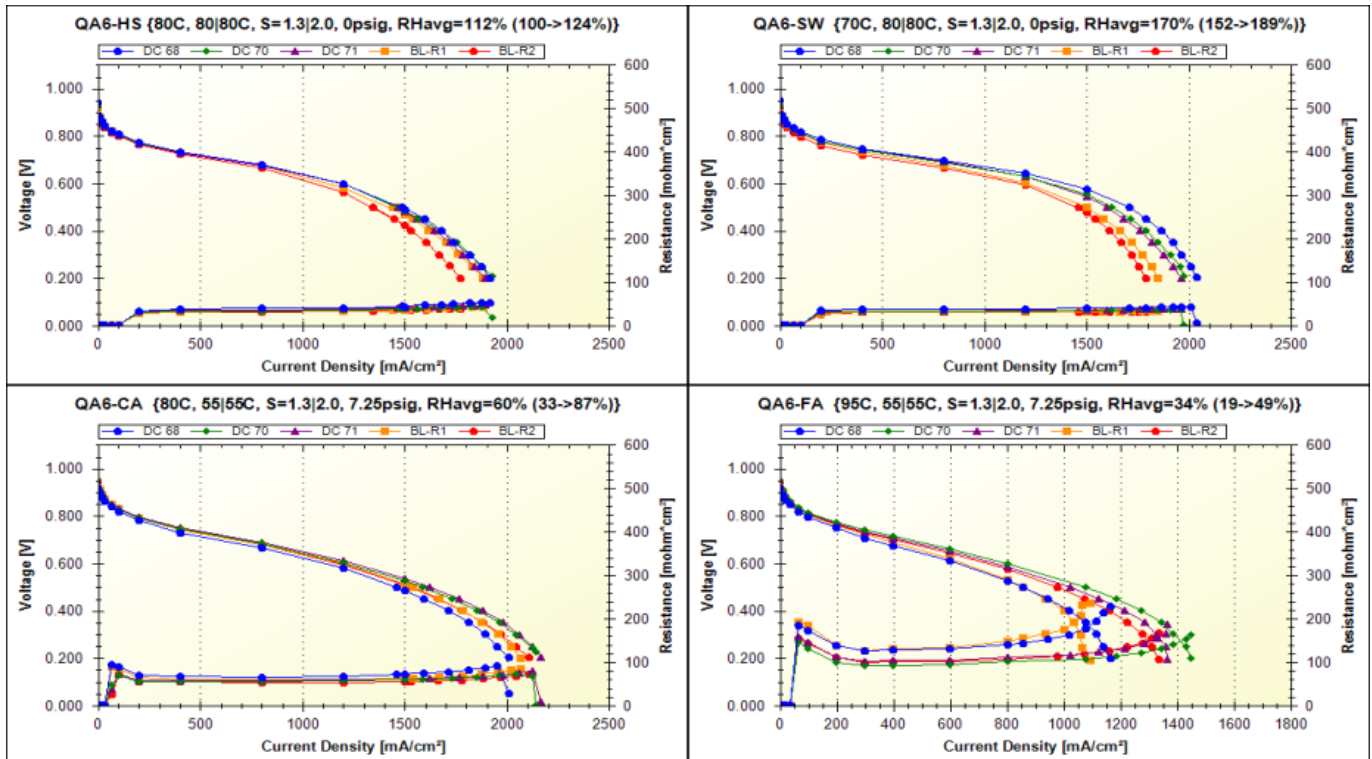


Fig. 61 – Direct coated MEA's demonstrate comparable or better performance than baseline MEA's in Gore single cell QC testing

At the University of Tennessee, a 50cm² (2.5 cm in width x 20 cm in length), wavy cell design was used (Fig. 62 and 63) for stack testing. This geometry was designed by General Motors during previously-funded DOE work. As shown in Figure 63, there are 22 parallel wavy channels at the cathode (left picture) and 11 parallel wavy channels (right picture) at the anode.

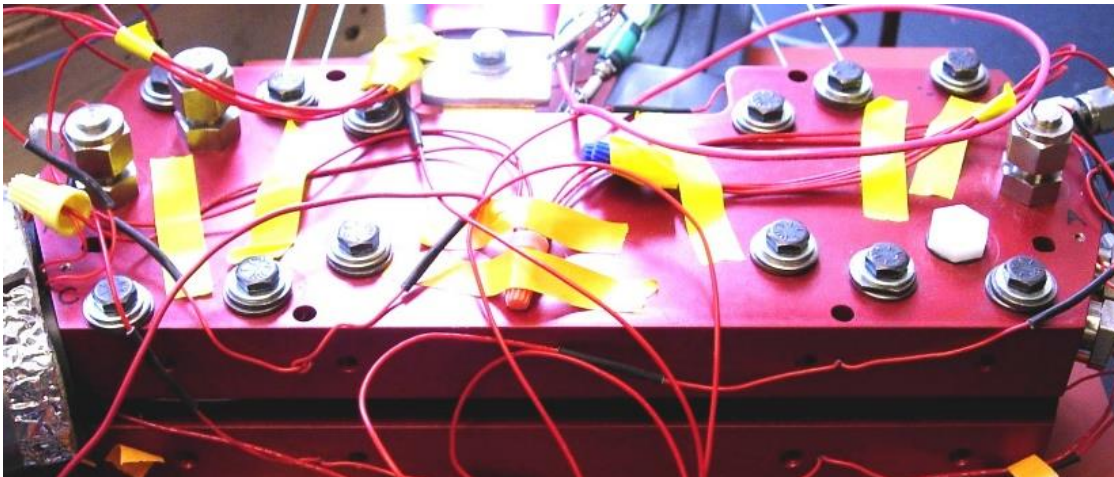


Fig.62: Assembled fuel cell with an active area of 50 cm²

The test system used for stack testing includes a Scribner 840e unit to control fuel cell temperature, flow rate, pressure and RH. A Scribner 890C E-load was also used with a capacity of up to 250A/ 1 kW. Properly sized mass flow controllers and humidification sub-systems were selected and integrated into the test stand. All flow controller, pressure transducer, and humidifier sub-systems were calibrated

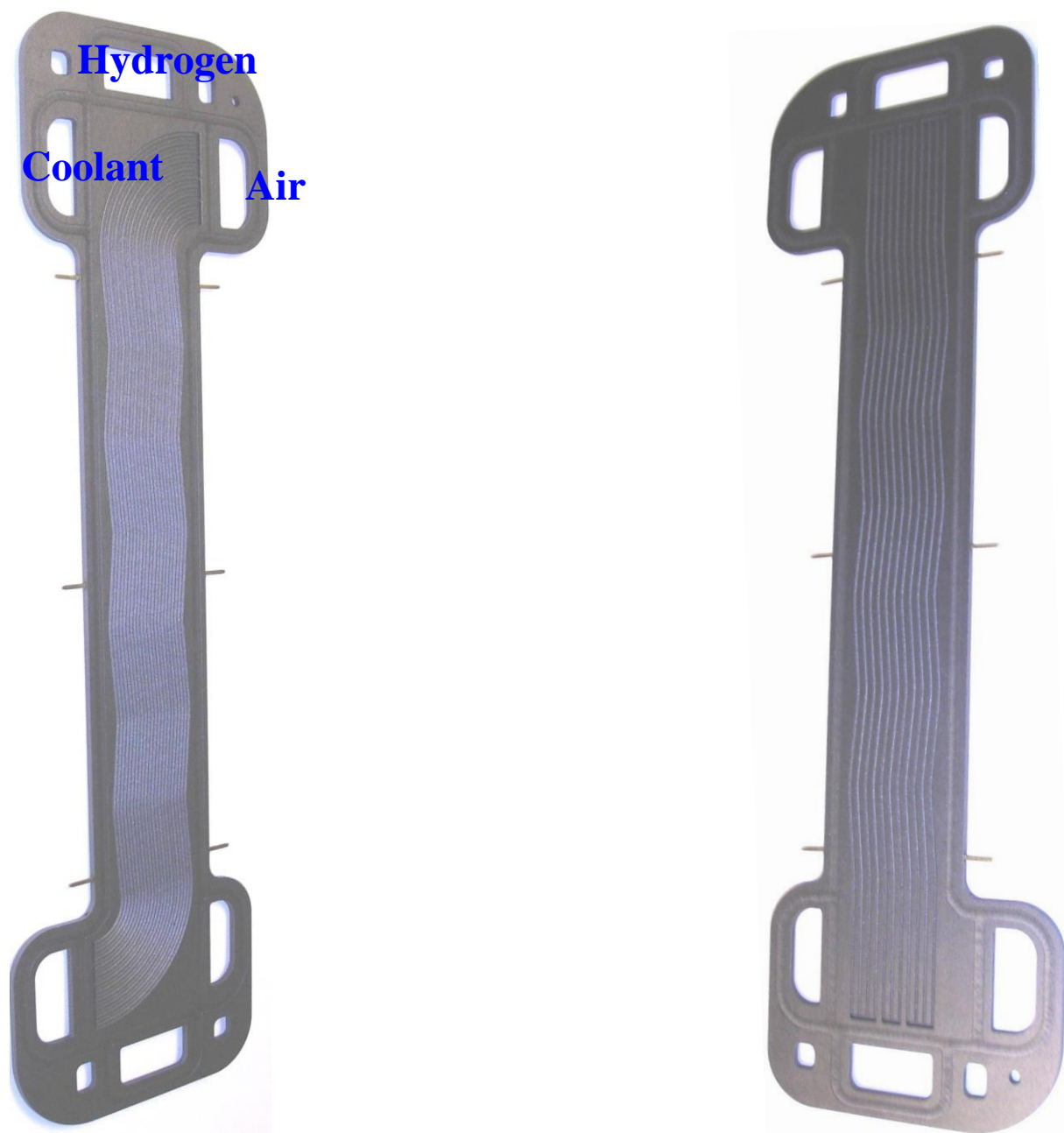


Fig. 63: Wavy flow fields; cathode face is on the left while the anode face is on the right.

The fuel cell was operated under Super Wet (SW), Historic/Stationary (HS), Current Automotive (CA) and Future Automotive (FA) conditions, which include a large relative humidity variation, ranging from 19% to 152%, which was designed to cover all fuel cell extreme environments. Based on the initial tests performed, some of the operating conditioned were changed from original conditions as summarized in

Table 10: Detailed summary of test conditions.

	Conditions Summary (Stoich sensitivity also performed)													
	Anode Inlet			Cathode Inlet		Backpressure		Stoich		Utilization		Average RH		
	Tcell	DP	RHa,i	DP	RHc,i	Anode	Cathode	Sa	Sc	Ua	Uc	RHInlet	RHOutlet	RHavg
	[oC]	[oC]	[%]	[oC]	[%]	[psig]	[Kpag]	[-]	[-]	[%]	[%]	[%]	[%]	[%]
QA6-HS	80	80	100	80	100	0.0	0.0	2.0	4.0	50	25	100	124	112
QA6-SW	70	80	152	80	152	0.0	0.0	2.0	4.0	50	25	152	189	170
QA6-CA	80	55	33	55	33	7.3	50.0	2.0	4.0	50	25	33	87	60
QA6-FA	95	55	19	55	19	7.3	50.0	2.0	4.0	50	25	19	49	34
RHS-60	60	55	79	55	79	7.3	50.0	2.0	4.0	50	25	79	206	143
RHS-70	70	55	51	55	51	7.3	50.0	2.0	4.0	50	25	51	132	91
RHS-87	87	55	25	55	25	7.3	50.0	2.0	4.0	50	25	25	66	45
RHS-103	103	55	14	55	14	7.3	50.0	2.0	4.0	50	25	14	36	25
RHS-110	110	55	11	55	11	7.3	50.0	2.0	4.0	50	25	11	29	20

- HS* (Historic/Stationary) Ambient Pressure, Saturated Inlets
- SW (SuperWet) Ambient Pressure, Super-Saturated Inlets
- CA* (Current Automotive) Medium Pressure, Dry
- FA (Future Automotive) Medium Pressure, Hot and Very Dry

*Stoich Sensitivity Performed: A= 1.7, 2.0, 3.1 | C= 2.6, 3.0, 4.0, 5.0

Primary Conditions (CP)

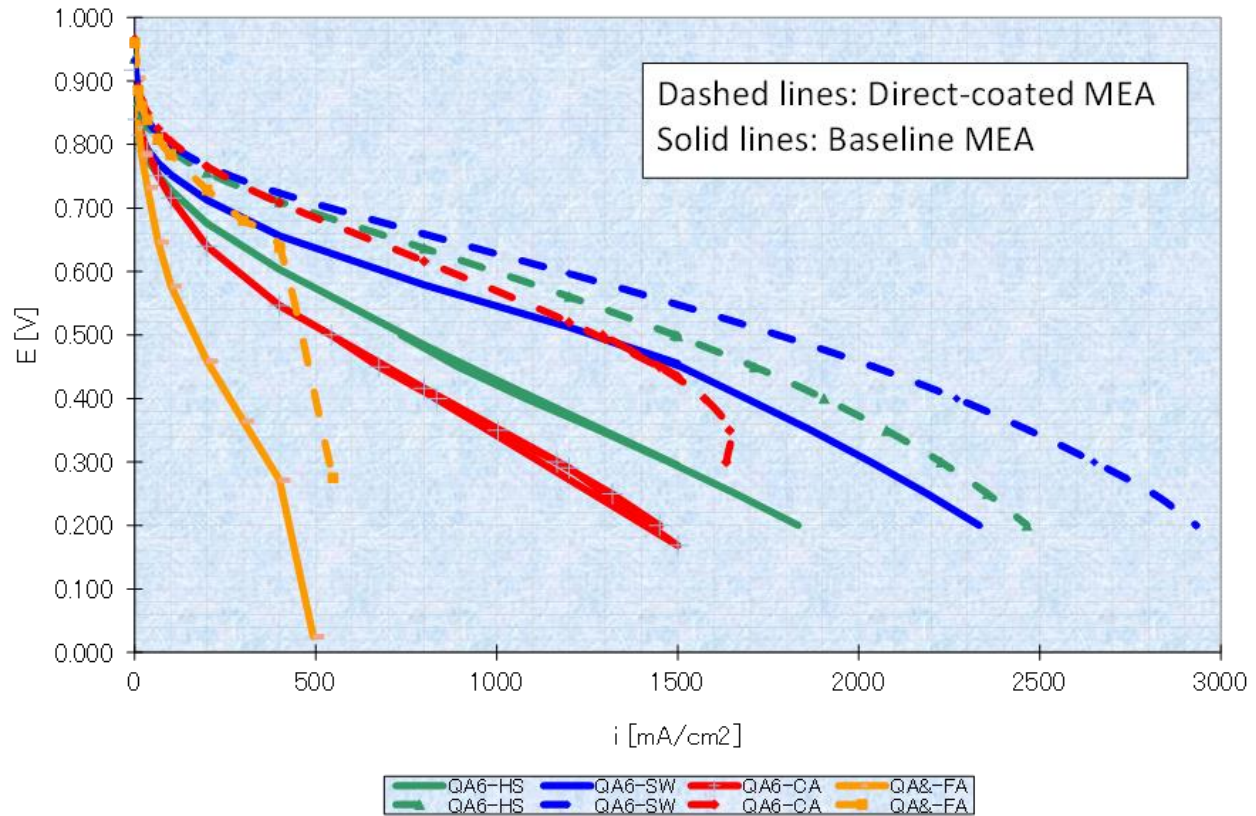


Fig.64: Comparison of Baseline and Direct-coated MEAs for the double-cell configuration based on the average cell voltage

The results of the baseline and direct-coated MEA stack testing are shown in Figure 64. Voltage cycling tests were conducted using a Bio-Logic SP-240 where the voltage was selected for cycling between 0.6V and 0.9V. The following table summarizes the details of the voltage cycling tests:

Table 11: Voltage swing cycling degradation test parameters

Cell Temperature: 80C
Anode: H ₂ (RH = 95%)
Cathode: N ₂ (RH = 95%)
Anode Stiocs 1.1 @ 1A/cm ²
Cathode Stiocs 1.3 @ 1A/cm ²

A voltage swing degradation test was completed for 48 hours, and results are shown in Fig. 65.

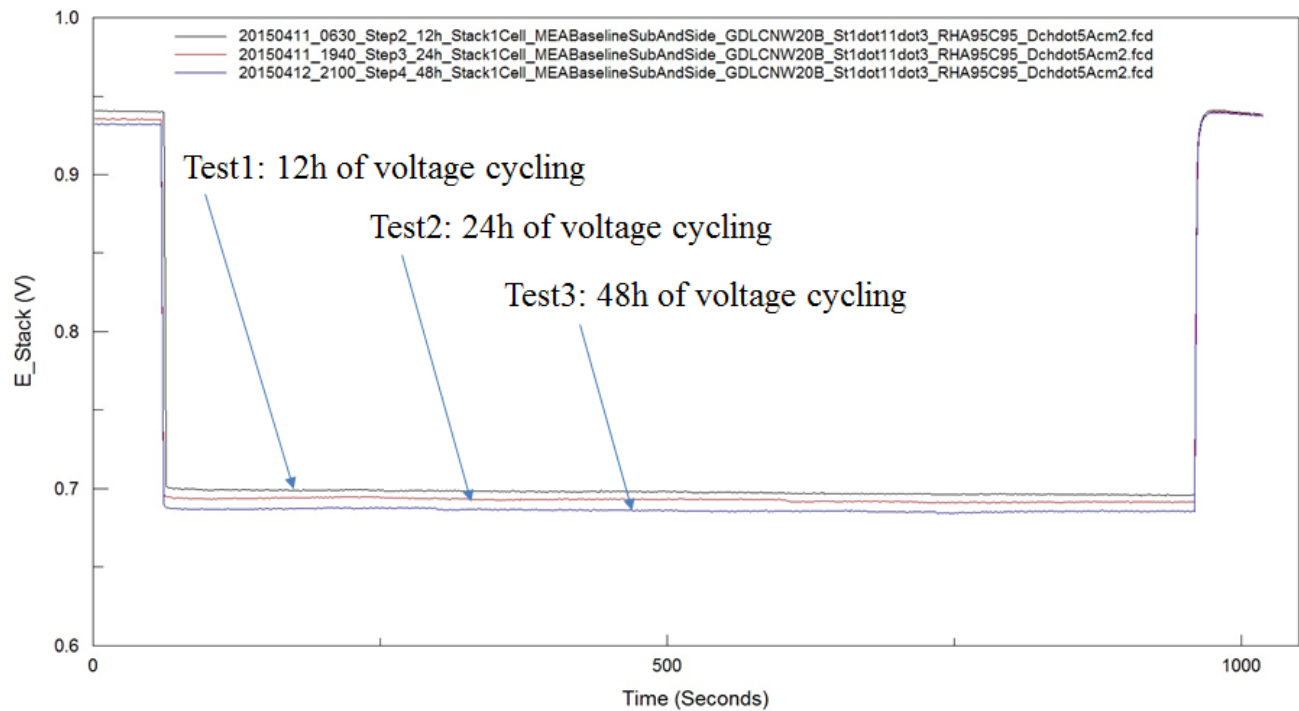


Fig. 65: Voltage decay of single-cell stack with baseline MEA after cycling (Discharge at 0.5 A/cm²)

The durability tests were duplicated as planned and repeatable results achieved. Table 12 summarizes the comparison.

Table 12: Voltage swing cycling degradation tests for baseline MEA at different cell builds

	Degradation rate (V/h)
Cell build 1	-0.000282
Cell build 2	-0.000305

The same test station and protocol was used to evaluate the direct coated MEA. The details of the voltage cycling have been reported at Table 12. A swing degradation test was completed for 48 hours, and results are shown in Fig. 66 for Direct-coated MEA.

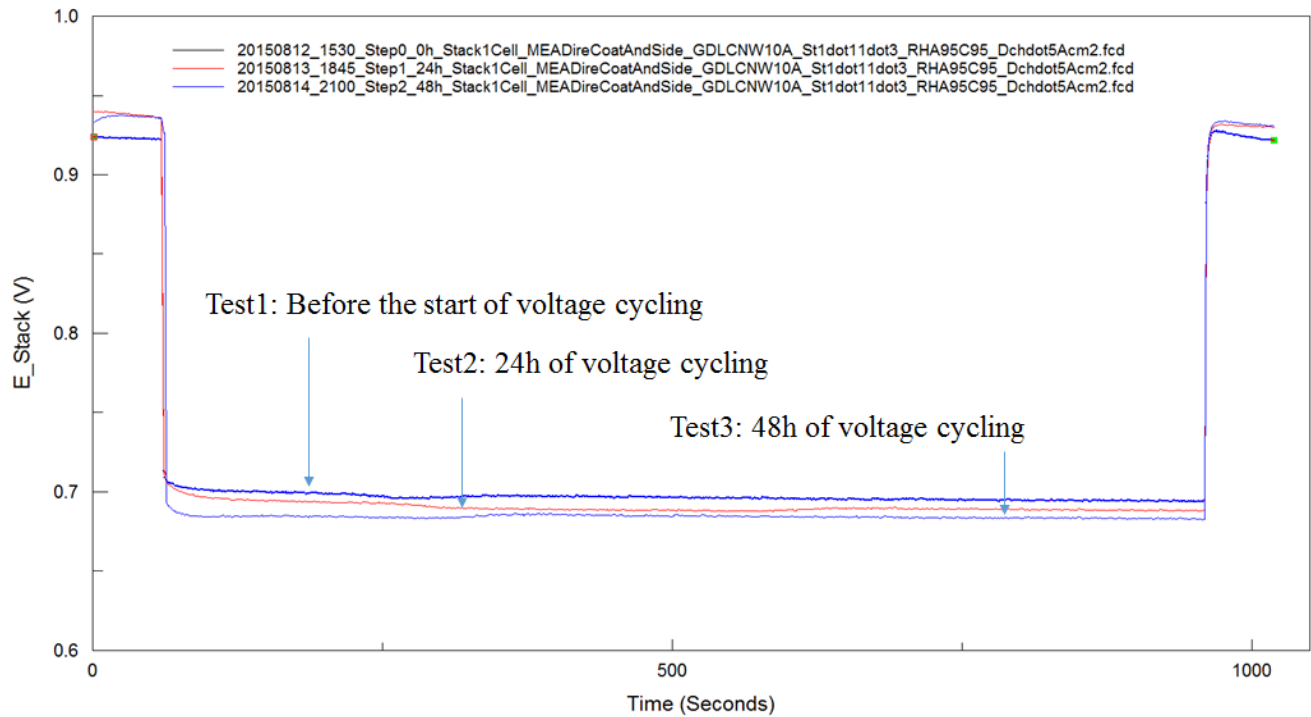


Fig. 66: Voltage decay of single-cell stack with Direct-coated MEA after cycling (Discharge at 0.5 A/cm²)

The durability tests were duplicated as planned and repeatable results achieved. Table 13 summarizes the comparison.

Table 13: Voltage swing cycling degradation tests for Direct-coated MEA at different cell builds

	Degradation rate (V/h)
Cell build 1	-0.000243
Cell build 2	-0.000229

Section 3

Mechanical Modeling/Experimentation of Alternative Structures

Parallel to the prototype generation, mechanical modeling of MEAs was undertaken. The modeling work was utilized to (i) determine the local stresses developing in the materials when subjected to relative humidity and temperature cycling, and (ii) determine crack and damage resistance of proposed MEA designs. The model results were used to guide the preparation of the new prototype MEAs.

In order to fully characterize the time-dependent response of the materials, the quasi-static response is typically determined by conducting tests at an extremely slow (effectively zero) displacement rate. However, this was not feasible in the current study, since such tests take prohibitively long times. Instead, an alternative method was used, where the equilibrium stress was recorded from the series of stress relaxation tests at selected holding strains. These equilibrium stress-holding strain pairs were then used to estimate the quasi-static response. The logic behind this approach is that, for a loaded specimen at a certain holding strain in a stress-relaxation test, the minimum stress that the specimen can relax to (the equilibrium stress) is equivalent to the stress from quasi-static loading, as illustrated in Fig. 2.3.

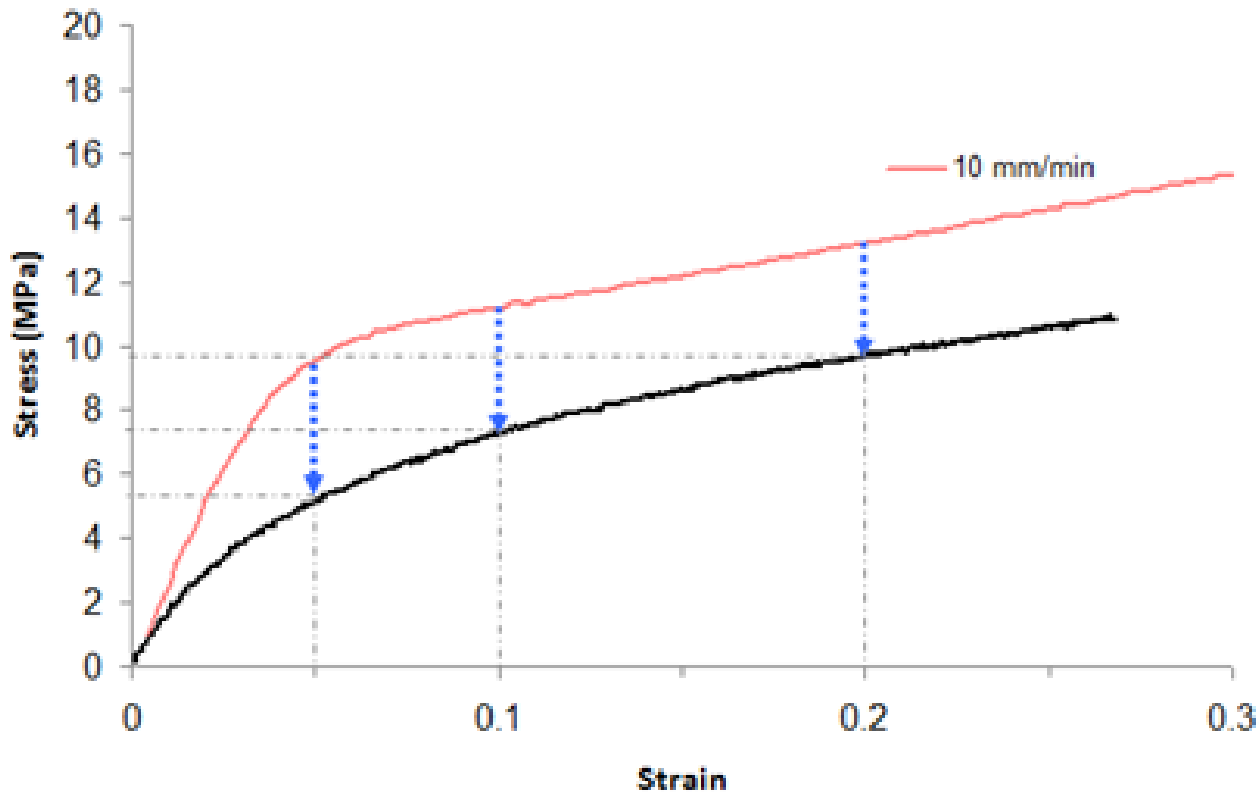


Fig. 2.3: Illustration of the method used for determining quasi-static curve from the stress-relaxation test

Constitutive models

In order to incorporate the time-dependent responses measured in section 2.1 in numerical simulations, constitutive models for the materials need to be established. These models need to capture the rate-temperature-humidity dependent properties of the materials.

Unreinforced membrane

A two-layer viscoelastic-plastic model constitutive equation is available in the commercial finite element software ABAQUS6.9 [2.1, 2.2]. A schematic of the constitutive model is shown in Fig. 2.4 and indicates the two “layers.” The right layer is the “elastic-plastic arm” consisting of an elastic (spring) element and a plastic (slider) element in series. The plastic slider comes into action when the stress in this top layer exceeds the yield strength. An additional spring element parallel to the slider is present to account for the hardening of the material post-yield. Any type of hardening (isotropic, kinematic or any other format) can be simulated with this model. The left layer is the elastic-viscous arm consisting of one elastic element (spring) and one viscous element (dashpot). The spring in this layer simulates the viscous modulus of the system while the dashpot adds strain rate dependency to the model. Any viscous law can be implemented for the dashpot element to capture the appropriate time dependent behavior of the material.

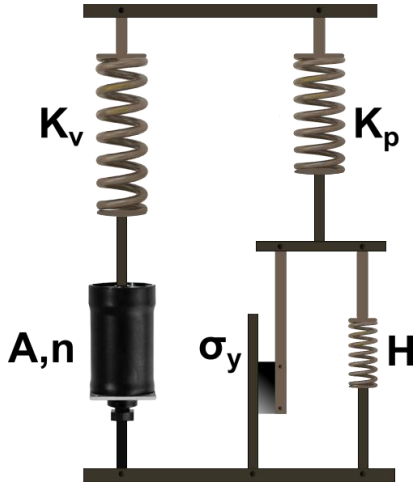


Fig. 2.4: One-dimensional idealization of the two layer viscoelastic-plastic model

The total stress during stress-relaxation simulation for the constitutive model is obtained as

$$\sigma = \sigma_y + H' \varepsilon_P + \left[\left(\frac{\dot{\varepsilon}}{A} \right)^{\frac{(1-n)}{n}} + (n-1)AK_v t \right]^{\frac{1}{(1-n)}} \quad (1)$$

where σ_y is the yield strength; σ_p the plastic strain; H' describes the hardening which may follow any general hardening law; K_v is the elastic spring constant in the elastoplastic arm. The total instantaneous elastic response of the material, $K_p + K_v$, is the stiffness during a tensile experiment conducted at high displacement rate. In addition, the dashpot captures the viscous behavior of the material using a time hardening law, $\dot{\varepsilon}_v = AS_v^n$, where the subscript refers to the dashpot element, the strain rate corresponds to the viscous strain rate and the stress is the viscous stress. Although this model can describe rate dependent visco-elastic-plastic behavior, it does not incorporate any temperature or humidity dependence.

Table 14 Viscoelastic-plastic properties of Nafion® 211 membrane as functions of temperature, humidity, and strain rate.

Temp °C	RH %	Kv [Mpa]		Kp [Mpa]	n	Ln(A)		σ_y [Mpa]	H [Mpa]
		10mm/min	250mm/min			10mm/min	250mm/min		
25	30	220	256	50	6.2	-19.47	-18.64	2.0	25.2
45	30	161	233	30	4.4	-14.55	-12.90	0.8	21.8
65	30	135	165	18	3.4	-11.42	-9.72	0.15	14.3
80	30	80	114	12	4.5	-12.51	-11.62	0.1	8.4
25	50	200	252	35	6	-19.18	-17.50	1.7	19.8
45	50	170	190	20	5.6	-16.55	-15.02	0.6	19.2
65	50	120	150	15	4.7	-13.87	-12.43	0.1	11.3
80	50	71	100	11	4.5	-11.76	-10.82	0.1	8.2
25	70	160	207	40	6.2	-19.11	-17.50	1.6	19.7
45	70	155	180	23	5.9	-16.92	-15.42	0.4	16.9
65	70	100	125	12	4.6	-13.03	-11.74	0.1	10.4
80	70	60	90	10.6	3.6	-10.48	-8.80	0.1	8.9
25	90	155	181	40	6.4	-19.11	-17.32	1.5	16.7
45	90	145	150	20	4.5	-13.03	-11.74	0.2	14.4
65	90	70	85	12	4.6	-13.72	-12.02	0.1	11.1
80	90	54	67	10.6	4.4	-11.51	-9.72	0.1	8.4

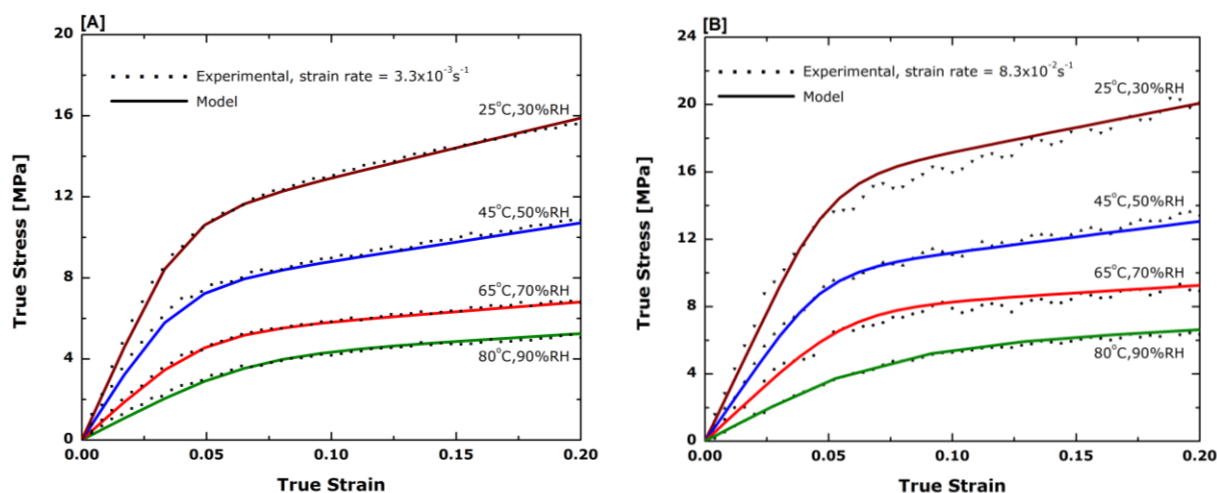


Fig. 2.5: [A] True stress vs. true strain uniaxial tensile response of the PFSA membrane at various environmental conditions obtained experimentally compared with the constitutive model predictions for strain rate $3.3 \times 10^{-3} \text{ s}^{-1}$; [B] strain rate $8.3 \times 10^{-2} \text{ s}^{-1}$

To include temperature and humidity effects, the constitutive equation (1) is fit to the stress-relaxation experimental data for each environmental condition measured above, to obtain the rate-temperature-humidity specific material parameters (shown in Table 14). The original two-layer model does not capture the strain-rate dependence of the initial stiffness [2.1, 2.2]. This capability was added in the present work by adding strain-rate dependence to the spring element in the elastic-viscous layer of the model. The parameters so obtained are then used to simulate both the tensile and stress-relaxation tests using finite element model. Comparisons at selected environmental conditions are shown in Fig. 2.5-2.6.

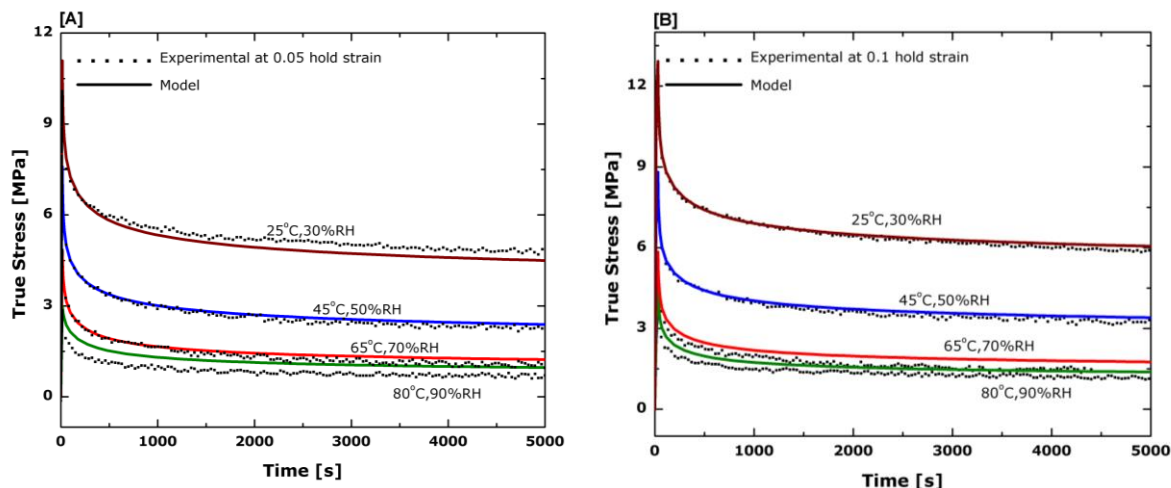


Fig. 2.6: [A] True stress vs. true strain stress relaxation response of the PFSA membrane at various environmental conditions obtained experimentally compared with the constitutive model predictions for hold strain 0.05; [B] hold strain 0.1

Determining the time, temperature and humidity dependent behavior of electrodes

The electrodes used for Proton Exchange Membrane Fuel Cells (PEMFCs) are typically painted or sprayed onto the membrane during manufacturing, making it difficult to directly characterize their mechanical behavior as a stand-alone material. In this part of the research, an experimental-numerical hybrid technique was devised to extract the electrode properties from the experimentally measured properties of Nafion[®] 211 membrane and a membrane electrode assembly (MEA) based on Nafion[®] 211 membrane at various temperatures, humidities, and strain rates. The following, will briefly review the experimental procedures, followed by a summary of the numerical work and reverse analysis used to determine the electrode properties.

Experimental Procedure

Details pertaining to the experimental procedure for determining the mechanical properties of Nafion[®] 211 membranes are discussed in previous published work [3.1] and in the preceding sections. A similar experimental procedure was employed to determine the mechanical properties of the MEAs. The procedure used in the interrupted tension tests is also described.

Tensile and relaxation tests

The time-dependent mechanical properties of MEAs based on Nafion[®] 211 membranes were measured at three strain rates (5.0, 0.2, 0 mm/mm per minute³) for sixteen temperature and relative humidity combinations, i.e. four selected temperatures (25, 45, 65, 80°C) and four selected relative humidities (30, 50, 70, 90%). The tests were conducted using the same equipment and procedures as described in section 2, for testing of the Nafion[®] 211 membranes. Two sets of experiments were conducted at each environmental condition: tensile tests and relaxation tests. The tensile tests were conducted at two selected strain rates (5/min and 0.2/min) and the relaxation tests, at three selected holding strains (0.05, 0.1 and 0.2).

³ Tests at higher strain rates (up to 12/min) showed similar stress strain response.

Interrupted tension tests

The interrupted tension tests were conducted at four selected temperature-humidity conditions ($T=25^{\circ}\text{C}/\text{RH}=30\%$, $T=25^{\circ}\text{C}/\text{RH}=90\%$, $T=80^{\circ}\text{C}/\text{RH}=30\%$, $T=80^{\circ}\text{C}/\text{RH}=90\%$) and two strain rates (0.2/min, 5.0/min) using the same experimental setup as in Section 3.1.1. Since the objective was to obtain the detailed micro-structural damage evolution of the MEA, the interrupted tests were performed up to selected true-strain levels of 0.1, 0.2, 0.3 and 0.4 as calculated from the load-displacement data.

After the specimens were subjected to the interrupted tests, two types of samples were cut from each: (1) a rectangular piece of approximately 10 mm in length and 5 mm in width to evaluate the extent of in-plane surface cracking; and (2) a slender piece of approximately 10 mm in length to evaluate the cracks in a cross-sectional view (Fig. 3.1). Observations were made using a scanning electron microscope (JSM-7400F) with a wide range of magnifications from 25x to 300,000x. By scanning the specimen surface, it was possible to collect data about the damage including individual crack location, orientation and crack length as well as crack density. Looking at the cross section of the sample gave information about the depth of the cracks and the existence and extent of delamination.

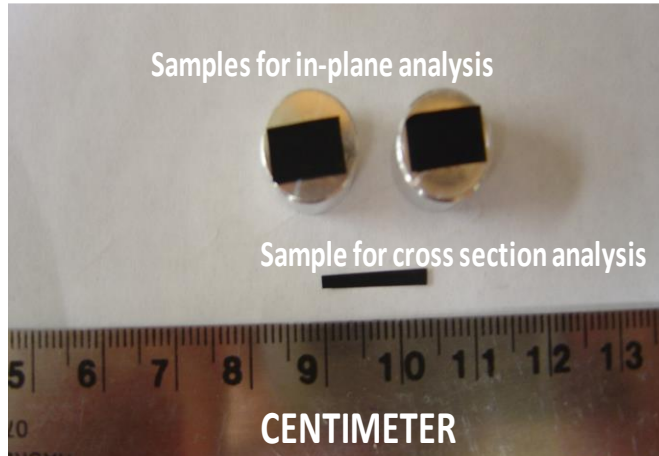


Fig. 3.1: Aluminum stubs and samples used for taking SEM images.

Experimental Results

Tensile and relaxation tests

Fig. 3.2 shows typical true stress-true strain curves for Nafion[®] 211 membrane and the MEA at 45°C and 50% relative humidity for several strain rates. True stress S_{true} and true strain, e_{true} relationships are used to take into account large deformation and can be related to engineering stress, S_{eng} and engineering strain, e_{eng} through the equations,

$$\sigma_{true} = (1 + \epsilon_{eng}) \sigma_{eng} \quad (1)$$

$$\epsilon_{true} = \ln(1 + \epsilon_{eng})$$

Fig. 3.3 shows typical stress-time curves for relaxation tests. The sample is held at constant strains of 0.05, 0.1, and 0.2 respectively. The stress decreases quickly during the first few minutes, and the rate of decrease gradually slows until it is changing very slowly after two hours. In an actual relaxation test, the

sample would be held at this constant strain until the stress reaches an equilibrium value. However, due to limitations in the testing equipment and practical considerations, the relaxation tests were run for two hours and the stress level at that time was assumed to be the equilibrium stress. By assuming that the zero strain condition corresponds to a stress free state, a curve was fitted through zero and the three equilibrium stresses determined from the relaxation tests to get an approximation to the quasi-static stress-strain curve for tensile tests as shown in Fig. 3.2.

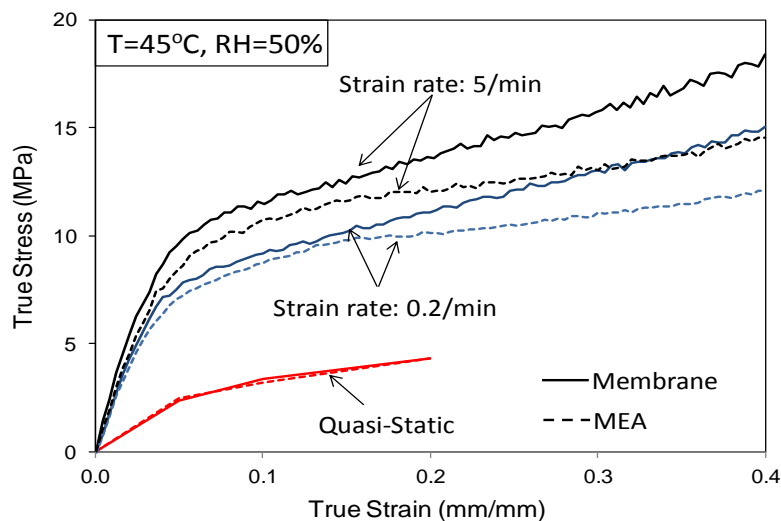


Fig. 3.2: True stress-true strain curves of Nafion[®] 211 membrane and the MEA at selected strain rates for T=45°C, RH=50% (the quasi-static results are derived from relaxation tests).

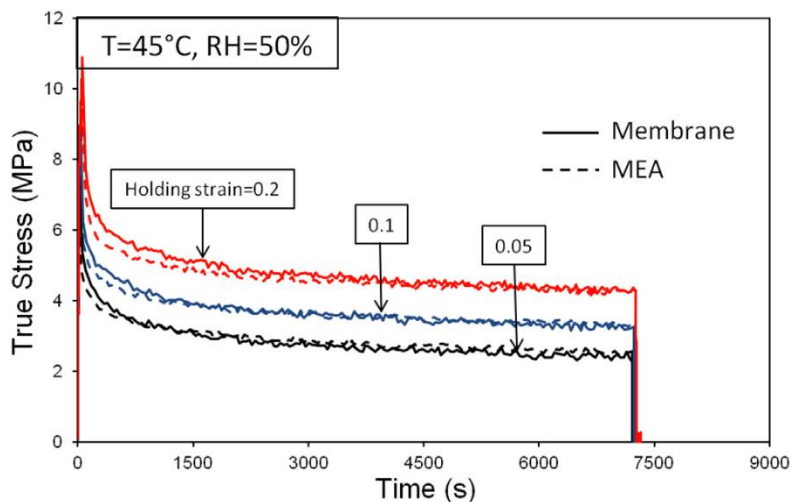


Fig. 3.3: True stress-time curves for relaxation tests of Nafion[®] 211 membrane and MEA at selected holding strains for T=45°C, RH=50%.

Based on the true stress-true strain response, mechanical properties such as Young's modulus and proportional limit stress were determined. The initial slope of the tensile true stress-true strain response is taken as the rate-dependent Young's modulus for the material. However, based on the monotonically increasing load used in the tests, it is not possible to identify the onset of yielding or a yield limit. Instead,

the proportional limit stress is reported, which has been defined graphically as the stress at the intersection of the tangents to the initial linear portion of the curve and the initial strain hardening response (Fig. 3.4).

The average Young's modulus and proportional limit stress of the two types of samples at selected strain rate/temperature/humidity combinations are summarized in Table 15 and Table 15, respectively. The results suggest that similar to Nafion® 211 membrane, Young's modulus and proportional limit stress of the MEA increase as the strain rate increases, temperature decreases or humidity decreases. Furthermore, the MEA has a lower Young's modulus and proportional limit stress than Nafion® 211 membrane at strain rates of 0.2/min and 5.0/min. For the quasi-static condition, the two types of samples have nearly the same properties.

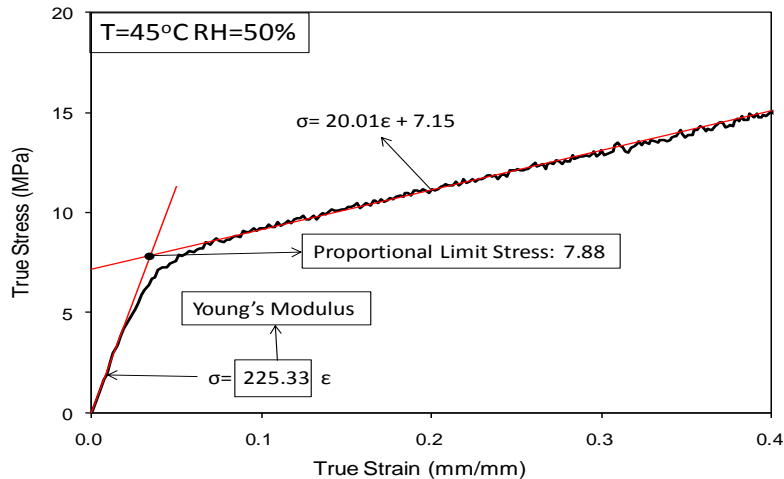


Fig. 3.4: Graphical definition of Young's modulus and proportional limit stress

Table 15 Young's modulus of Nafion® 211 membrane and the MEA based on Nafion® 211 membrane as a function of temperature, humidity, and strain rate.

Temperature/Humidity	Strain rate (mm/mm per minute)	Nafion® membrane	MEA
45°C /50%	0.0	45.9	46.5
45°C /50%	0.2	210.2	188.8
45°C /50%	5.0	248.1	224.7
45°C /90%	0.2	165.4	135.1
80°C /90%	0.2	66.1	60.7

Table 16 Proportional limit stress of Nafion® 211 membrane and the MEA Nafion® 211 membrane as a function of temperature, humidity, and strain rate.

Temperature/Humidity	Strain rate (mm/mm per minute)	Nafion® membrane	MEA
45°C /50%	0.0	2.3	2.3
45°C /50%	0.2	7.9	6.9
45°C /50%	5.0	10.6	7.8
45°C /90%	0.2	6.3	4.1
80°C /90%	0.2	3.9	2.9

Interrupted tension tests

Fig. 3.5 shows SEM images of the MEA plane surface after interrupted tension tests, up to strain levels from 0 to 0.6. The specimens were loaded at a strain rate of 0.2/min with T=25°C and RH=30%. The images

suggest that cracking initiates between strain levels of 0.1 and 0.2, and that the crack density increases as the strain increases. The images also show that cracking develops perpendicular to the direction of tensile loading. Fracture information such as crack length (in the plane) and crack density has been quantified for all conditions considered to provide input for the finite element models used to determine the electrode's mechanical behavior (discussed below).

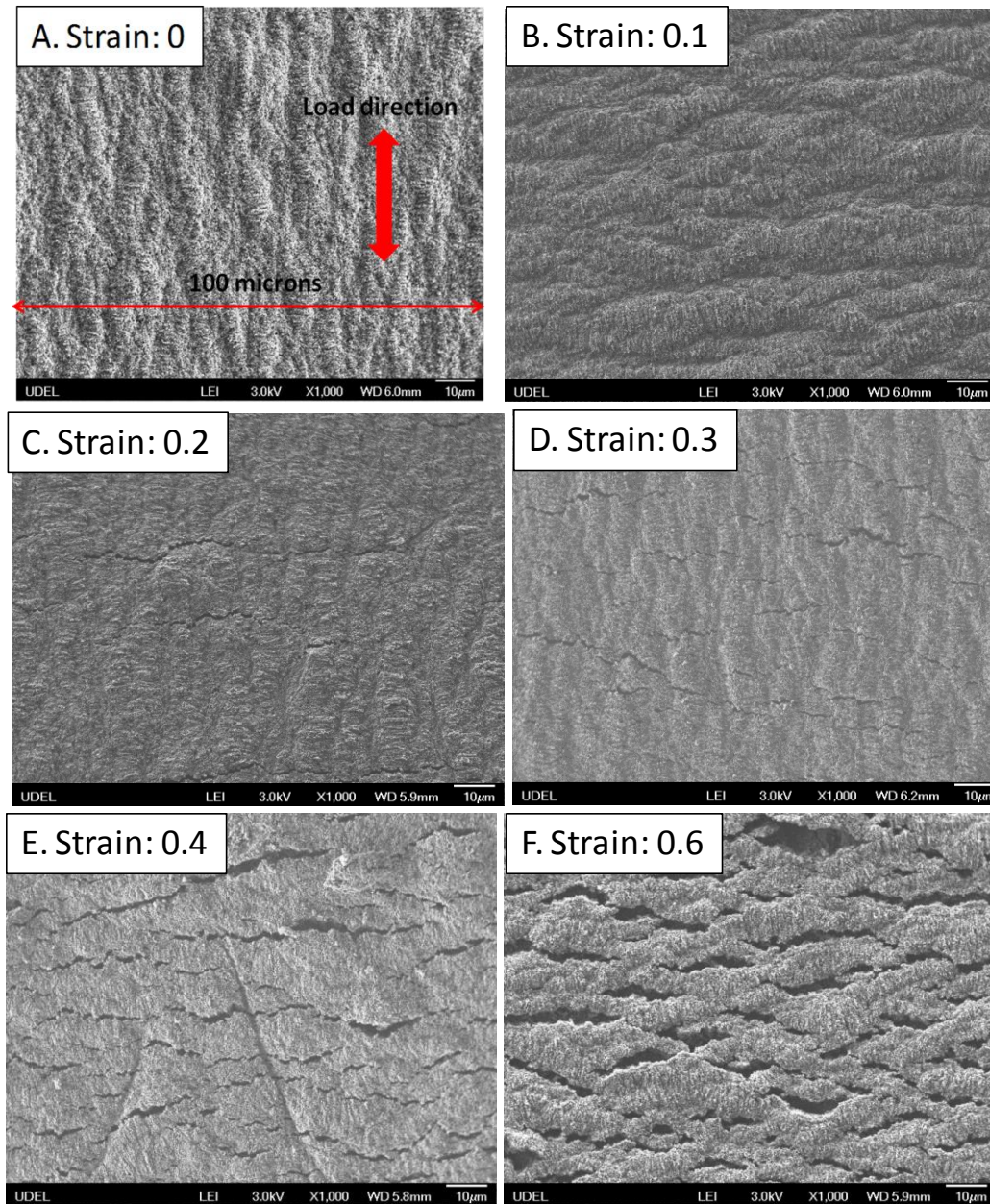


Fig. 3.5: SEM images of the MEA plane surface loaded to selected strain levels of 0, 0.1, 0.2, 0.3, 0.4 and 0.6 at the strain rate of 0.2/min with $T=25^{\circ}\text{C}$, $\text{RH}=30\%$.

Interfacial delamination between the membrane and electrodes was also investigated. Fig. 3.6 shows SEM images of the MEA cross-sectional surface after interrupted tension tests, up to strain levels from 0 to 0.6. The specimens were loaded at a strain rate of 0.2/min with $T=25^{\circ}\text{C}/\text{RH}=30\%$. The figure shows that the delamination initiates around the tip of the vertical cracks through the electrode, and that the vertical cracks are limited to the electrode layers.

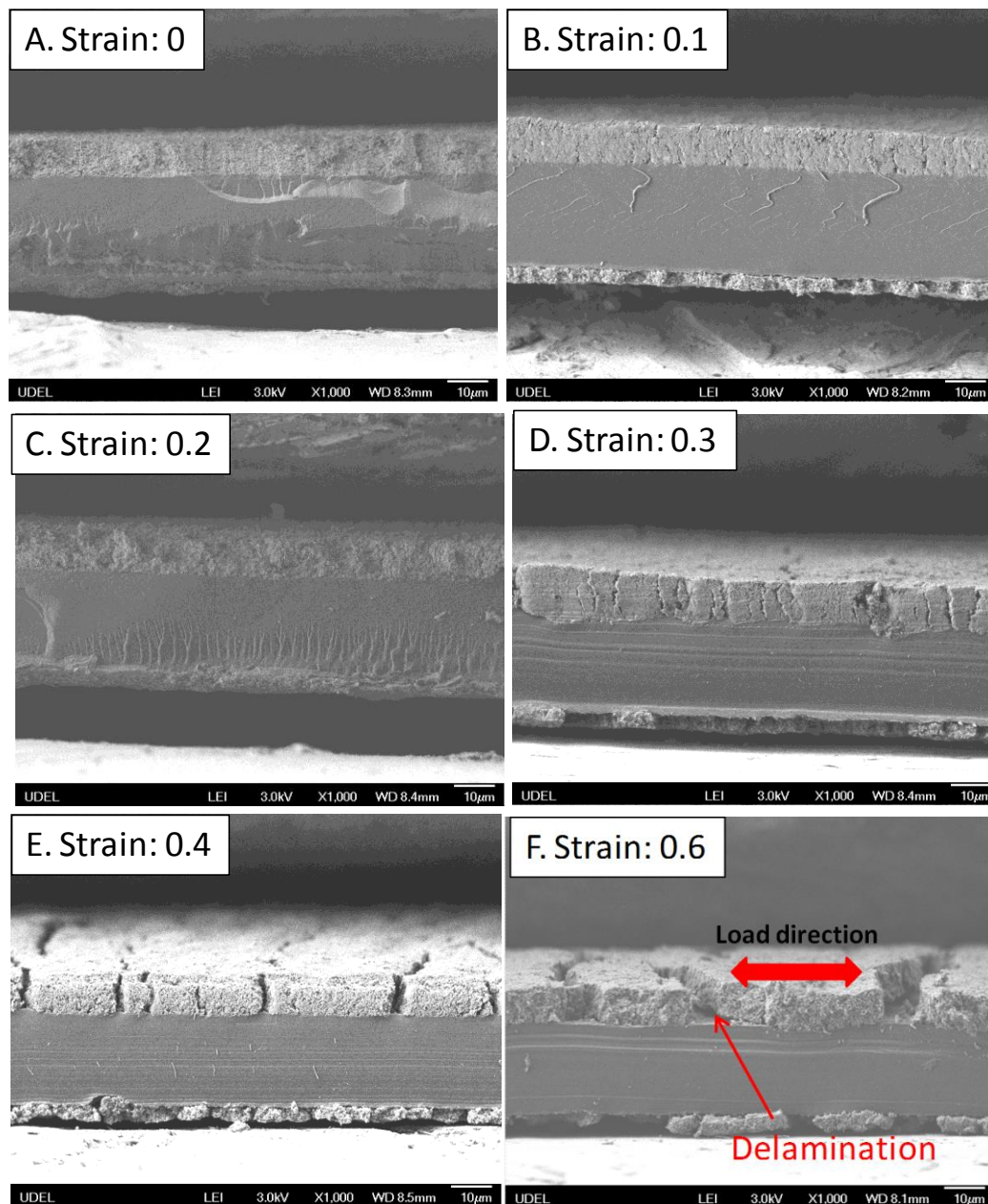


Fig. 3.6: SEM images of the MEA cross-sectional surface loaded to selected strain levels of 0, 0.1, 0.2, 0.3, 0.4 and 0.6 at the strain rate of 0.2/min with $T=25^{\circ}\text{C}$, $\text{RH}=30\%$.

The professional statistical software package, *ImageJ*⁴, was used to analyze and summarize all the crack information. For each condition, a non-dimensional crack density parameter, G , was calculated to characterize the crack distribution with a single parameter. In an image of area, A , with N cracks of

⁴ *ImageJ* can be downloaded for free at <http://rsbweb.nih.gov/ij/download.html>

individual length, l_i , the crack density parameter, G , can be determined from the following relationship [3.2]:

$$G = \frac{\sum l_i^2}{A} \quad (2)$$

Two distributions of micro-cracks can be assumed to have a similar effect on the overall constitutive response of the system when they have the same crack density parameter [3.2]. Thus, to simulate the mechanical response with a set of simple 2D models, the N cracks with various lengths in a representative area can be modeled as M cracks with a same crack length L , where M is the equivalent crack number. In this study, L was assumed to be the width of the SEM images (100 microns) as shown in Fig. 3.5. The equivalent crack number M can be calculated according to the following equation:

$$G = \frac{\sum l_i^2}{A} = \frac{Ml^2}{A} \quad (3)$$

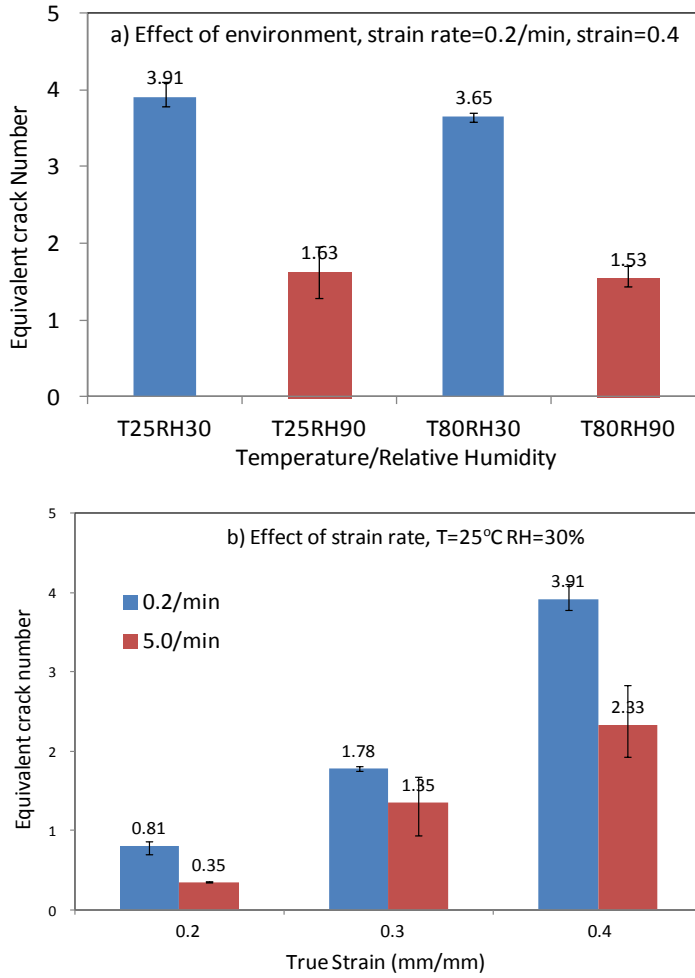


Fig. 3.7: Effects of a) environment (temperature/humidity), b) strain rate on the equivalent crack number.

The results suggest that at higher humidity and at higher strain rate fewer cracks develop, and that temperature has little effect on the crack number (Fig. 3.7). This may be the result of a competition between the crack driving force and fracture toughness.

Determination of the electrode behavior

Linear properties

Within the linear regime, the rule-of-mixtures was used to determine Young's modulus of the electrode since the MEA is a simple layered structure of the membrane and electrodes.

For uniaxial tension, it can be assumed that the overall strains, ϵ , in the individual layers and the MEA in the loading direction are the same (iso-strain):

$$\epsilon_{MEA} = \epsilon_m = \epsilon_e \quad (4)$$

where the subscripts *MEA*, *m* and *e* represent the membrane electrode assembly, membrane and electrode, respectively. The resultant force on the MEA consists of the force on the membrane and the force on the electrodes:

$$F_{MEA} = F_m + F_e \quad (5)$$

Furthermore, assuming a uniform uniaxial (1-D) stress distribution and Hooke's Law,

$$F / A = S = E\epsilon, \quad (6)$$

yields,

$$(E\epsilon A)_{MEA} = (E\epsilon A)_m + (E\epsilon A)_e. \quad (7)$$

This equation can be used to calculate Young's modulus for the electrode, given the elastic properties of the membrane and MEA and the thickness of the individual layers in the MEA, which were obtained from the tensile and relaxation tests described in Section 3.1. The results of these calculations are shown in Fig. 3.8.

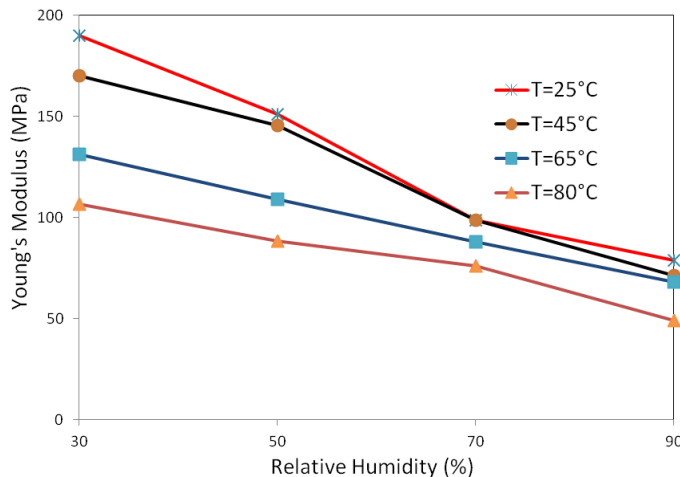


Fig. 3.8: Calculated Young's modulus of the electrode at a strain rate of 0.2/min

Nonlinear properties

Beyond the linear regime, plasticity, strain hardening, and mechanical failure mechanisms cause nonlinearities, which preclude the use of the rule-of-mixtures. Consequently, a two-dimensional finite element model (Fig. 3.9) was developed using the commercial software ABAQUS 6.9 to determine the nonlinear electrode properties via reverse analysis. Since symmetry conditions were assumed, a representative segment of the MEA was modeled using a quarter of the structure. The boundary conditions: $u_y=0$ on the bottom edge and $u_x=0$ on the left edge were imposed. Generalized plane strain was assumed and a uniform x-displacement condition was applied on the right edge.

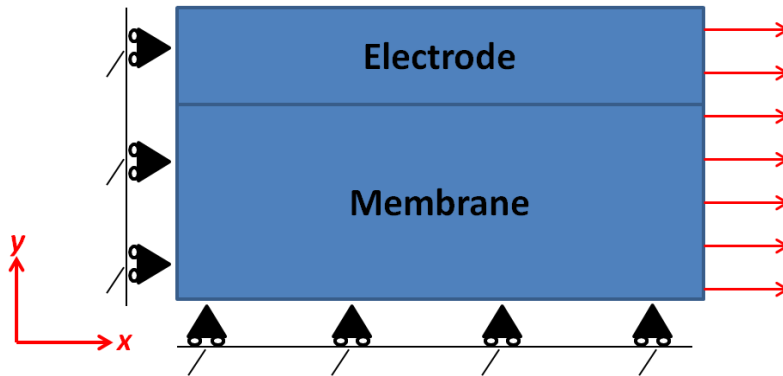


Fig. 3.9: Representation of the two-dimensional numerical model used to determine the mechanical properties of the electrodes; $u_y=0$ on the bottom edge and $u_x=0$ on the left edge.

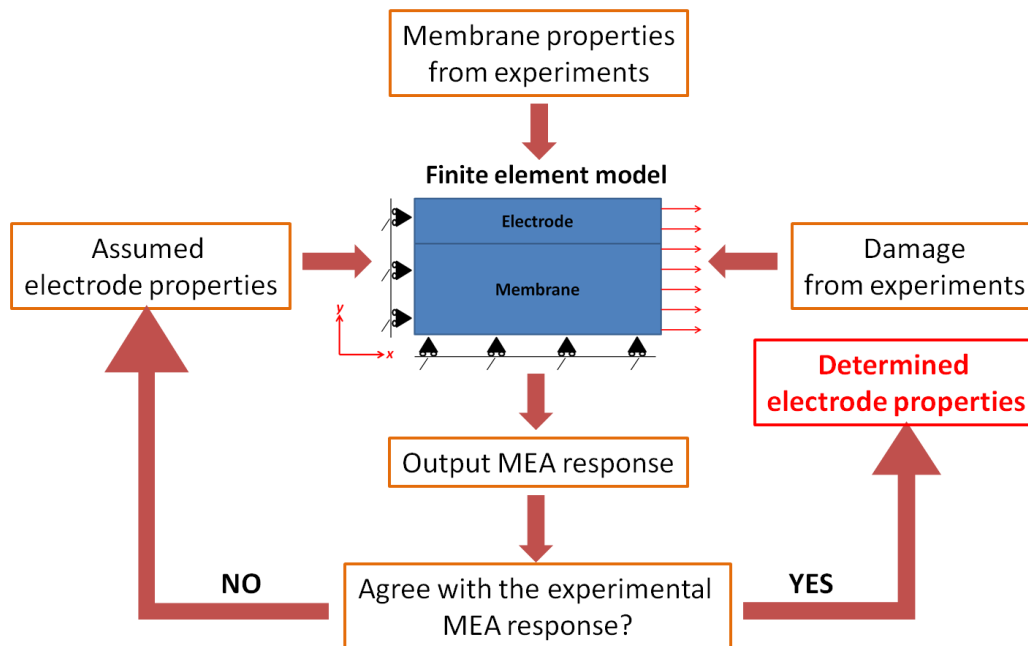


Fig. 3.10: The general method used to determine the electrode properties beyond the linear elastic regime.

The mechanical properties of the Nafion® 211 membrane and electrodes are required input for the finite element model. While the properties of the Nafion® 211 membrane are known from the experiments described above, the properties of the electrodes are the objective of the analysis and are unknown. Therefore, representative values are assumed and varied in the model for a series of successive runs.

When the true stress-true strain response of the MEA from the model agrees with the experimental results for the MEA, it can be assumed that the constitutive properties of the electrodes used in the model correspond to the actual properties of the electrodes. The flow chart in Fig. 3.10 illustrates the general methodology.

The SEM images from the interrupted tension tests showed that electrode cracks initiate between strains of 0.1 and 0.2. Therefore, fracture is not involved for strains up to 0.1, and a commonly-used empirical stress-strain relationship [3.3] was implemented to capture the linear plus the initial non-linear behavior of the electrode before cracking

$$\sigma = \frac{S}{E} + K \dot{\epsilon}^n \quad (8)$$

In this relationship, the rate-dependent Young's modulus of the electrodes, E was previously determined from the rule-of-mixtures analysis described in Section 3.4.1. The terms K and n are material constants that characterize the non-linear portion of the curve, and are typically obtained by fitting the equation to experimental data. In this work, K and n (in the constitutive relationship for the electrodes) were systematically varied in the finite element model of the MEA (Fig. 3.9). When the true stress-true strain response of the MEA from the finite element model agreed with the experimental results, we assumed that the electrode properties used in the model corresponded to the actual properties of the electrodes.

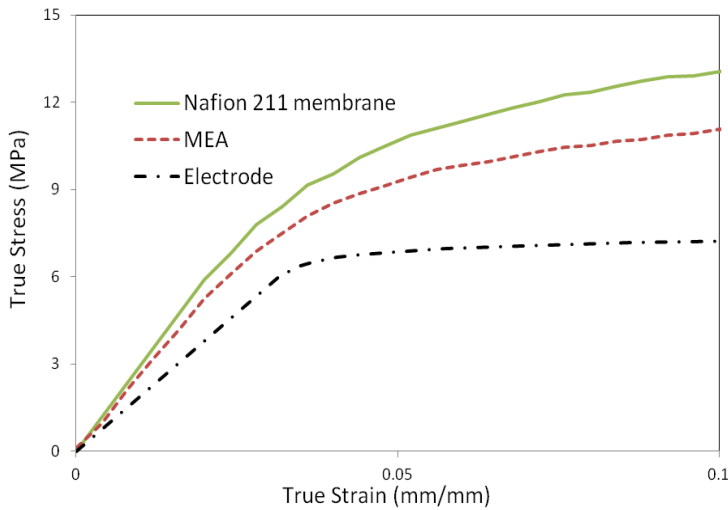


Fig. 3.11: True stress-true strain response of the membrane, MEA and electrode at 0.2/min and T=25°C, RH=30%, up to strain 0.10.

Fig. 3.11 shows a typical comparison of the true stress-true strain response of the membrane, MEA and electrode (derived), up to a strain of 0.1. Fig. 3.12 shows the derived true stress-true strain response of the electrode up to a strain of 0.1 for various combinations of temperature, humidity and strain rate. Similar to the behavior of the membrane, the electrode becomes stiffer as the temperature decreases, humidity decreases, or strain rate increases. The uniqueness of K and n is not guaranteed due to the nonlinearity of Eq. 8. However, values determined via this technique are very useful for predicting the stress-strain response of the MEA, as shown in Fig. 3.13.

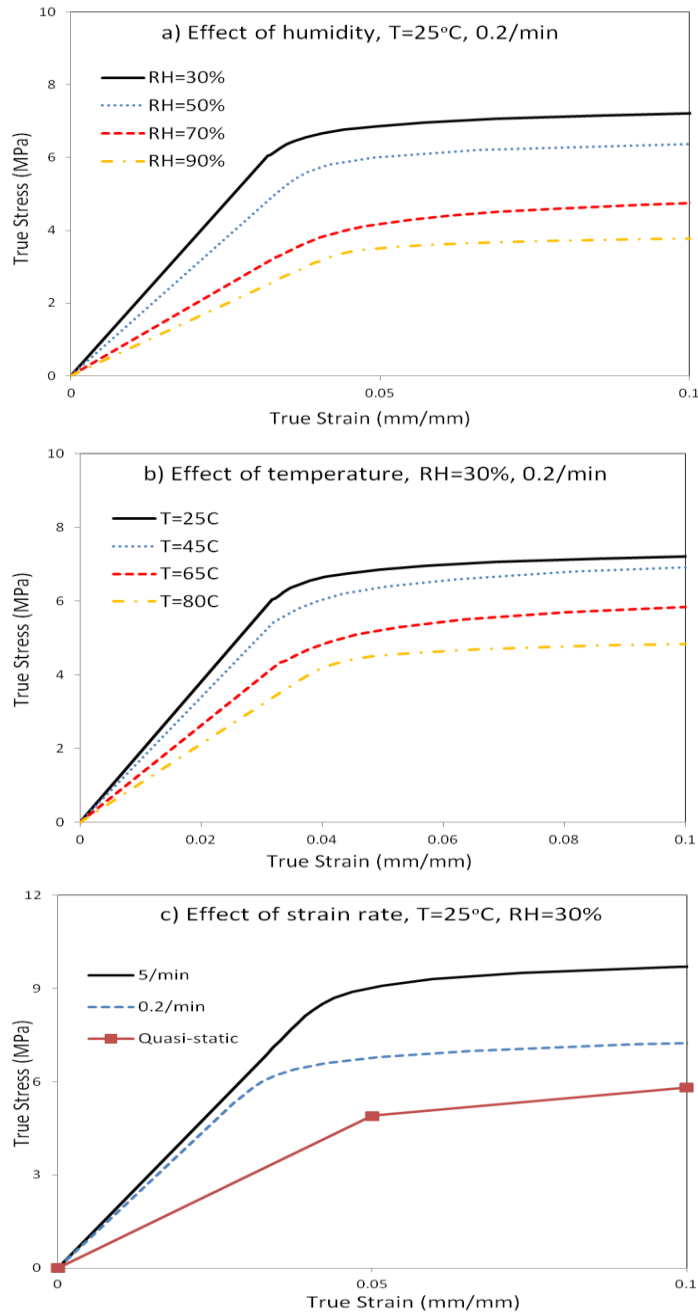


Fig. 3.12: The effect of a) humidity, b) temperature, and c) strain rate on the calculated true stress-true strain response of the electrode, up to strain 0.10.

When the strain is higher than 0.1, however, the response from the empirical equation (Eq. 8) deviates significantly from the response observed in the experiments. The results from the interrupted tension experiments indicate that this deviation may be due to the onset of cracking. Therefore, the damage evolution information obtained from the interrupted tests was incorporated to the numerical model to simulate the electrode response beyond strain 0.1. The details are not presented here for conciseness. Note that in real operations of PEM fuel cells, the strains in the membrane and electrodes normally do not go beyond 0.1.

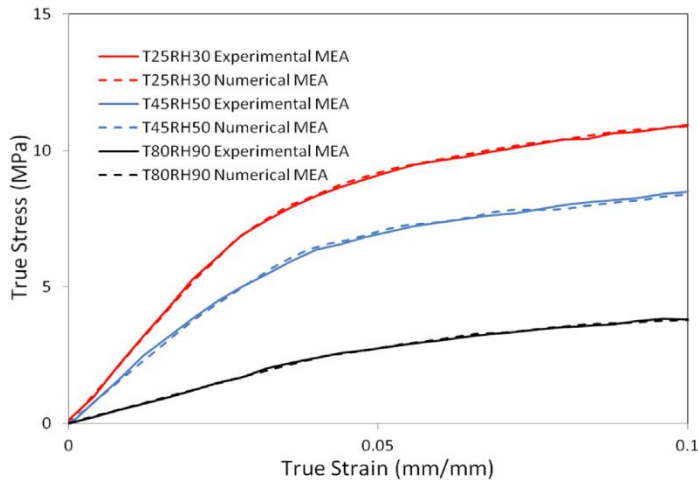


Fig. 3.13: Predicted true stress as a function of true strain for the MEA, compared to the experimental MEA response, for various T/RH combinations.

The derived time-dependent mechanical behavior of the electrode, as a function of strain rate, temperature and humidity, can be defined and used in finite element models through a two-layer viscoplastic constitutive model [3.4].

Since it is difficult to directly measure electrode mechanical properties, an experimental-numerical hybrid technique has been devised to determine the time-dependent mechanical behavior of the fuel cell electrodes. Tensile and relaxation tests were conducted to characterize the time-dependent mechanical behavior of both Nafion® 211 membranes and MEAs based on Nafion® 211 membranes at various temperatures, humidities, and strain rates. Those tests show that the MEAs have lower Young's modulus and proportional limit stress than Nafion® 211 membranes. The tests also show that Young's modulus and proportional limit stress of the MEAs are affected by the temperature, humidity and strain rate in a similar way to the effects on Nafion® 211 membranes. The rule-of-mixtures together with an iso-strain condition were then used to determine the rate-dependent Young's modulus of the electrodes. The results indicate that the electrodes generally have lower Young's modulus than Nafion® 211 membranes. Under quasi-static conditions, however, the membrane, electrode and MEA have very similar Young's modulus.

Beyond the initial linear regime, the behavior becomes nonlinear and requires a more sophisticated modeling approach. Therefore, reverse analysis based on finite element models was conducted to determine the electrode behavior at moderate to large strains. In addition, interrupted tension tests at various strain levels were conducted in order to collect crack evolution information for the MEA. The interrupted tension tests showed that cracks in the electrodes initiate between strains of 0.1 and 0.2 perpendicular to the direction of tensile loading. Separately conducted finite element simulations showed that it is unlikely that cracks initiated at a lower strain level, and closed before SEM examination.

Quantification of the crack information shows that in the range of values tested, higher humidity or larger strain rate leads to fewer cracks, and that temperature has little effect on the crack number. These fracture observations were then incorporated to the finite element models for determining the electrode behavior at large strain levels. The results show that the electrodes show trends similar to those for Nafion® 211 membrane as a function of strain rate, temperature and humidity, but have lower Young's modulus and proportional limit.

Study of the effects of different layering configurations on the mechanical behavior of reinforced membranes

The aforementioned work established a set of time, temperature and humidity dependent mechanical properties for typical unreinforced and reinforced membrane and electrode materials. This work was leveraged in finite element models to explore the effects of various layering configurations of reinforced/unreinforced material on the stresses developed in the system during selected hygrothermal loading conditions.

Model parameters

The basic model domain is a representative plane strain element of MEA adapted from previous research conducted at the University of Delaware [4.1] and is shown in Fig. 4.1. The models of the membrane consists of one layer or two layers of the reinforcement material, arranged along with unreinforced PFSA resulting in a composite structure. Schematics of the geometry of the layering configurations showing the relative arrangement of reinforced and unreinforced layers are shown in Fig. 4.2. The reference case of unreinforced PFSA is also shown and was investigated for comparison.

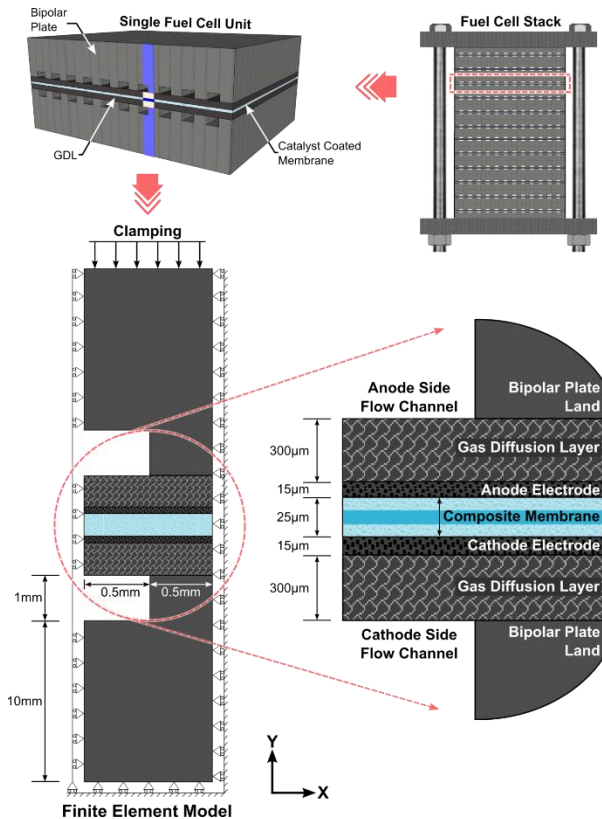


Fig. 4.1: Schematic of plane-strain the computational model domain used to simulate mechanical behavior of composite layered membranes.

Experimental study of the fatigue fracture behavior in membrane materials

Understanding the fatigue fracture behavior of the membrane electrode assembly (MEA) materials is critical to the development of more durable fuel cells. The fatigue properties and behaviors of the MEA materials are material specific and will depend on the environmental test conditions, and must therefore be evaluated experimentally. This section describes the research conducted to measure the fatigue fracture behavior of the membrane materials.

Establishing experimental protocol and parameters for tension fatigue tests

In order to produce meaningful fatigue fracture measurements, a set protocol and reasonable values and ranges for the various experimental parameters needed to be determined. As a starting point, Nafion[®] 211 membrane with a nominal sample size of 50mm x 20mm was chosen and the specimen was to be tested in cyclical tension. These choices were made to be able to use the existing test equipment and to produce fatigue measurements that can be compared with the previous material test results.

Specimen geometry

In traditional fatigue fracture tests, the specimen is cracked and then pre-fatigued in such a way as to produce a “sharp” initial crack tip. For the membrane materials and environmental conditions considered here this would be extremely difficult, if not impossible, to do in a reproducible manner from specimen to specimen. Therefore, a pre-existing flaw of a set size and location was introduced into the specimens. Given the overall specimen dimensions, an appropriate size and location for the pre-existing flaw needed to be determined so that the stress field around the tip of the flaw was not overly sensitive to the configuration.

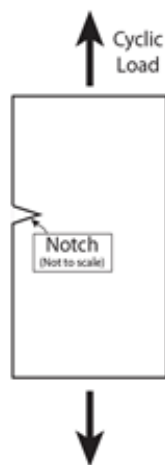


Fig. 5.1: Sketch of specimen configuration

To study the effects of flaw configuration, a 2D plane stress, finite element model of a membrane test sample (Fig. 5.1) was developed in the commercial software ABAQUS 6.10. The parameters and assumptions of the simulation are listed as follows.

1. A displacement loading of 10mm is applied on the top of the membrane while the bottom is fixed, which is in accordance with the experiment setup.
2. The viscoelastic properties (determined in previous sections) are taken into consideration. The temperature and humidity are taken as constant and uniformly distributed.
3. The flaw length is kept constant during loading.

In the simulations, two flaw sizes, 4mm x 2mm and 2mm x 1mm respectively, and two membrane lengths, 50mm and 60mm were studied. The width of the membrane is set as 20mm. The results show that when the flaw size is smaller, the stress field is less sensitive to the location. Specifically, when the flaw is 4mm x 2mm changing the location by 5mm (10% of the total length) affects the stress field significantly. However, if the size is 2mm x 1mm, the same change in the location has little effects on the stress field (Fig. 5.2). Increasing the sample length reduces the sensitivity to the configuration and location, but a length of 50mm was determined to suffice for the smaller flaw size. To conclude, it was determined that the pre-existing flaw should be small relative to the sample dimensions and should be located near the middle of the specimen but need not be exactly at the middle.

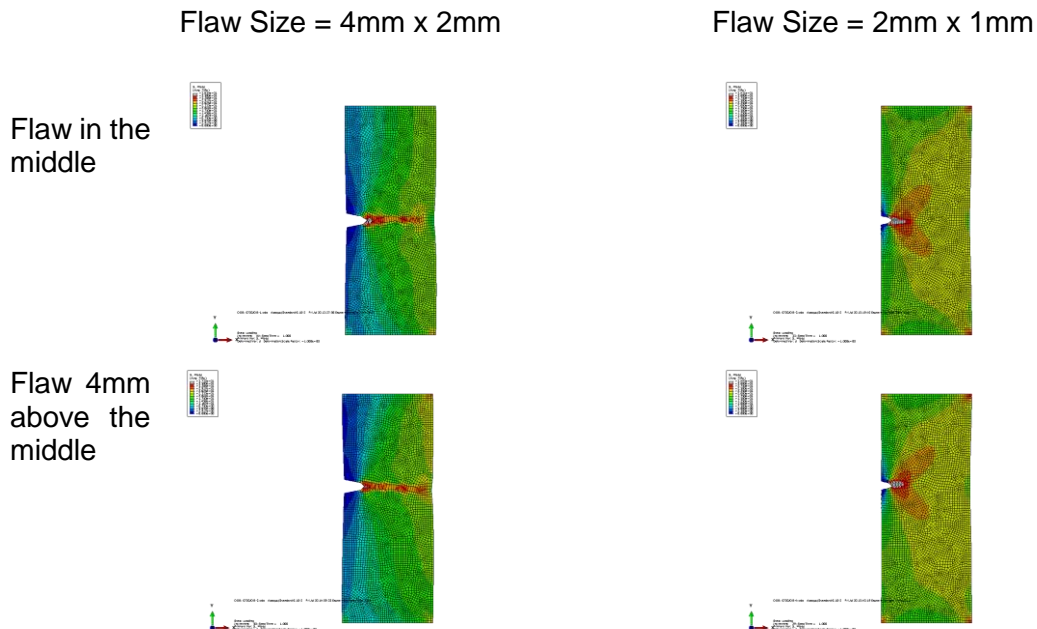


Fig. 5.2: Study of the sensitivity of stress field to the flaw size and location

Loading frequency

Since the mechanical response of membrane materials is time and rate dependent, fatigue tests need to be conducted under a suitable loading frequency, which should be small enough to ensure the membrane has time to relax, but large enough to make it possible to run several thousand cycles. The appearance of a 'phase shift' between the load and displacement indicates that dynamic test is too fast for the membrane to relax during the test. A number of preliminary tests were run to determine appropriate frequencies for fatigue testing of Nafion® 211 membrane materials. A sample result for a test conducted at 0.1Hz is shown in Fig. 5.3 and it can be observed that at this frequency, the phase shift is relatively small.

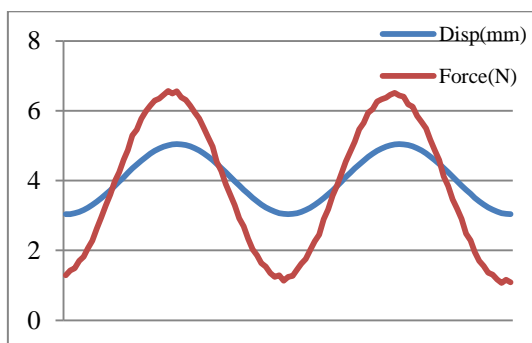


Fig. 5.3: Phase shift for Nafion® 211 membrane at frequency=0.1Hz

Control mode

There are two control modes available for use in the hydraulic fatigue testing machine, the displacement and force control mode. Preliminary tests were conducted under both these two method and results compared.

Fig. 5.4 shows the results of several cycles of displacement-controlled testing conducted on unflawed membrane specimens. It can be seen from the figure that under the same uniform cyclic displacement loading (Amplitude=0.5mm-1.5mm), the nominal stress decreases with increasing number of cycles.

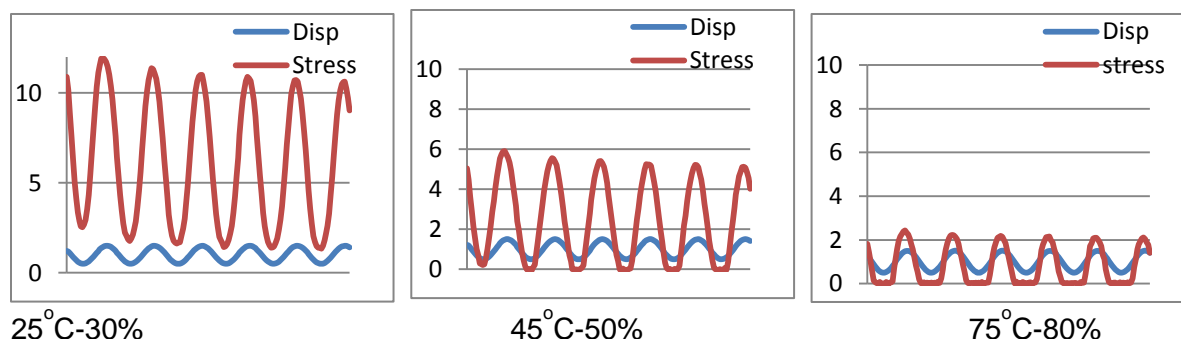


Fig. 5.4: Force and displacement as functions of time for displacement-controlled fatigue loading of Nafion 211 membrane at several temp-RH combinations

In addition, Fig. 5.4 shows that the membrane goes slack (zero tensile stress) for part of the cycle, especially for the high temperature and humidity cases. While the membrane is slack, it will buckle out-of-plane. The resulting stresses and deformations will be uncontrolled and unknown, resulting in an uncontrolled fatigue loading. To avoid this slacking behavior, force controlled testing is proposed.

From previous studies, the maximum tensile stress in the membrane during fuel operation is around 8 MPa, which corresponds to 4.5N load for the test specimen of Nafion® 211 membrane.

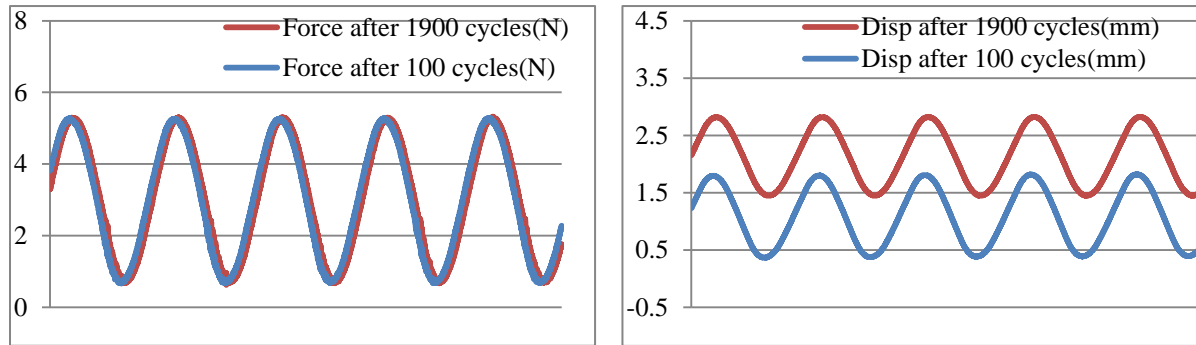


Fig. 5.5: Force and displacement as functions of time for displacement-controlled fatigue loading of Nafion® 211 membrane at 100 and 1900 cycles

A test result for the force control mode is shown in Fig. 5.5. It can be seen that the membrane deforms significantly during the test. However, under the force-control, the membrane is in tension during the entire test (both force and displacement are larger than zero). Compared with the displacement control mode, the force level is stable and the displacement increases due to plastic and/or creep deformation during test. As a result, the force control mode is selected as control method for the following fatigue tests.

Force Level

In force control, the maximum and minimum input forces are kept constant and the force is cycled between them. The force level is generally characterized by two parameters; mean force and force amplitude (shown in Fig. 5.6). To determine a reasonable force level for testing, a series of preliminary tests were run on pre-flawed Nafion® 211 specimens at intermediate temperature (T) and relative humidity (RH). The results are summarized in Table 17.

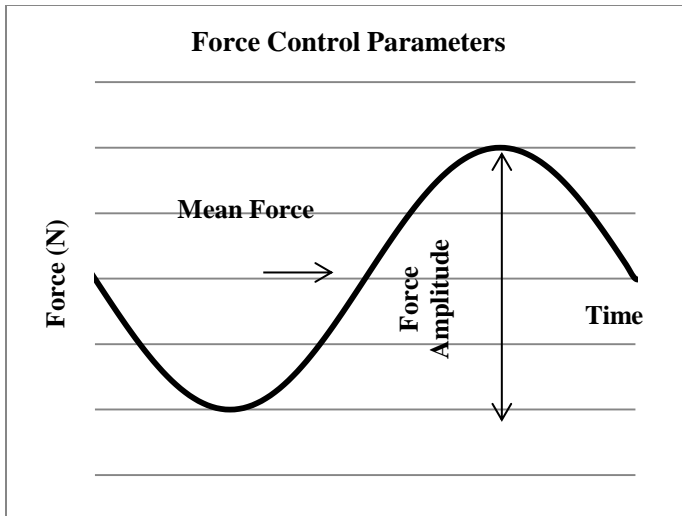


Fig. 5.6: Schematic of Force-control parameters

From a practical standpoint, a force level should be chosen so that the effects of temperature and humidity can be clearly seen within a reasonable time frame. (previous studies showed that the fatigue tests could be run at 0.1 Hz.) From Table 17, it is observed that the force level corresponding to a mean nominal stress of 4.76 MPa and nominal stress amplitude of 2.38 MPa allows for this. In the following tests, a nominal stress amplitude of approximately 2.38 MPa and a mean nominal stress of approximately 4.76 MPa were used to study the effect of temperature, relative humidity and applied load.

Table 17: Preliminary data used to determine force level for fatigue tests

Min(N)	Max(N)	Width(mm)	Mean(MPa)	Amp(MPa)	Lifetime(Cycles)
1.2	3.6	20	4.76	2.38	>15000
1.25	3.65	20	4.86	2.38	833
1.3	3.7	20	4.96	2.38	633
1.4	3.8	20	5.16	2.38	253

Flaw initiation

As discussed earlier, it is impractical to create pre-cracks in the membrane materials, so pre-existing flaws of a set size and location were used. However, after a number of fatigue tests were conducted, it was observed that the 'sharpness' of the initial flaw, had a significant effect on the test results, with the sharper flaws producing the most reproducible fatigue lives. Further investigation, showed that an initial flaw made with a razor blade has a relatively blunt tip (Fig. 5.7a) while that made with a scalpel has relatively sharper tip (Fig. 5.7b). In addition, it was found that super-cooling the scalpel before cutting the sample made for even sharper tips (Fig. 5.7c).

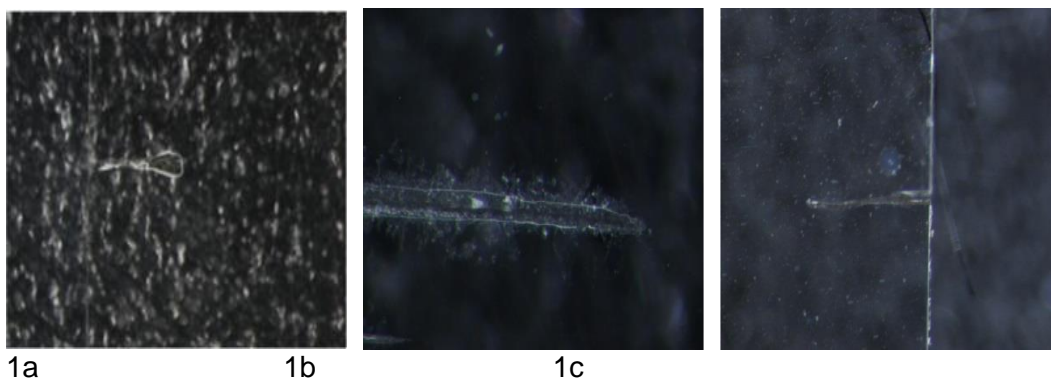


Fig. 5.7: Micrographs of flaws produced using different initiation methods

Therefore, in the tests reported in the following, the initial 1mm flaw was cut using a scalpel that was immersed in liquid nitrogen (-196°C) for 30s and a new scalpel blade is used after every 20 cuts. In addition, through trial and error it was found that the most repeatable results can be achieved when one cover sheet is left on the membrane, and the cut is made from the uncovered side.

Fatigue life measurements for Nafion[®] 211 membrane

A series of fatigue experiments was conducted using the testing protocols and parameters established in section 5.1; Nafion[®] 211 membrane cut into nominally 50mm x 20mm specimens with a 1mm initial flaw (initiated following the protocol described in section 5.1.5) cycled under a tensile force control with a force level corresponding to a nominal stress amplitude of approximately 2.38 MPa and a mean nominal stress of approximately 4.76 MPa.

Table 18 and Fig. 5.8 show the effect of relative humidity at fixed temperature ($T=45^{\circ}\text{C}$). Two or three tests were performed for each condition to verify reproducibility. It is observed that with increasing relative humidity, the lifetime of the membrane decreases significantly. At high humidity (70%), the lifetime is only a few cycles.

Table 18: Cycles to Failure for Nafion[®] 211 membrane for $T=45^{\circ}\text{C}$ and various RH

Min(N)	Max(N)	Width(mm)	Mean(MPa)	Amp(MPa)	Lifetime(Cycles)	RH(%)
1	3.4	20	4.37	2.38	8225	30%
1	3.5	20.4	4.38	2.43	6195	
1	3.4	20.5	4.26	2.32	560	
1.05	3.35	20	4.37	2.28	749	40%
1	3.4	20.6	4.24	2.31	622	
1	3.3	20	4.27	2.28	390	
1.1	3.4	20	4.46	2.28	300	50%
1	3.4	20.5	4.26	2.32	329	
1	3.35	20	4.32	2.33	250	
1	3.5	20.2	4.42	2.46	5	60%
1	3.4	20	4.37	2.38	16	

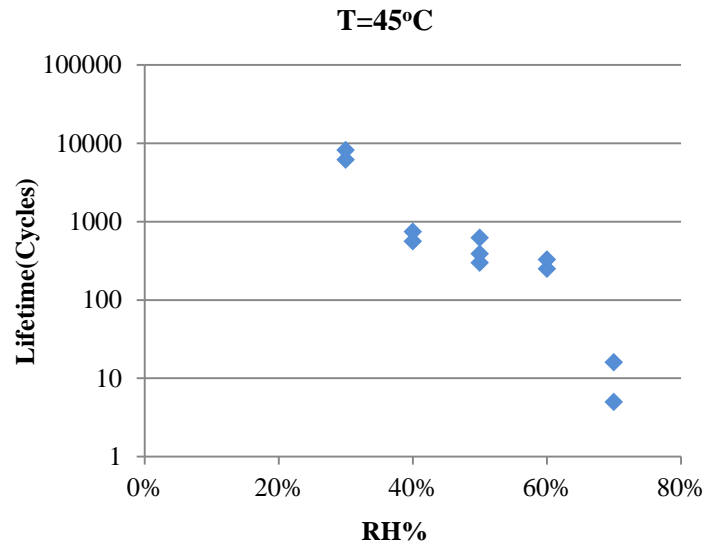


Fig. 5.8: Cycles to Failure for Nafion® 211 membrane as a function of RH for T=45°C with Nominal Mean Stress of 4.76 MPa and Nominal Stress amplitude of 2.38 MPa

The effect of temperature on the fatigue life was also studied by setting a constant relative humidity (RH=50%) and varying the temperature. In addition, various force levels were studied with constant force amplitude but different mean force values to investigate the effect of force level (nominal stress level). The results in Fig. 5.9 show that with increasing temperature, the lifetime decreases logarithmically and this trend is observed for all the three force levels studied. Therefore, at a fixed temperature and humidity, increasing the mean force while keeping force amplitude constant, results in a decrease in cycles to failure.

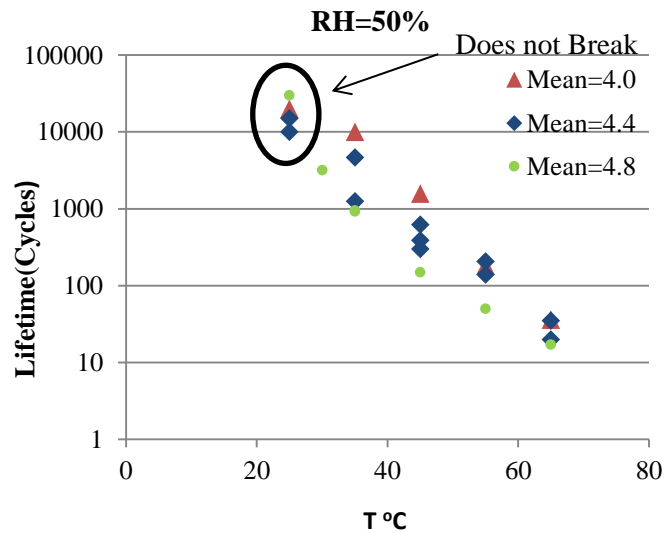


Figure 5.9: Cycles to Failure for Nafion® 211 membrane as a function of T and Nominal Mean stress for RH=50%

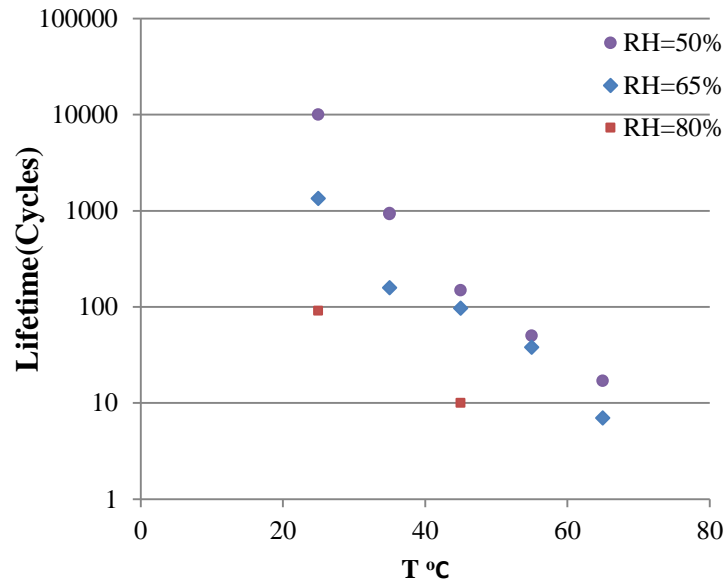


Fig. 5.10: Cycles to Failure for Nafion® 211 membrane as a function of T for various RH with Nominal Mean Stress of 4.76 MPa and Nominal Stress amplitude of 2.38 MPa

Additional tests were conducted at higher relative humidity. For those tests, the applied force level is set to correspond to: Nominal Mean Stress=4.76 MPa, Nominal Stress Amplitude=2.38MPa. Fig. 5.10 shows that with an increase in relative humidity, the lifetime of Nafion membrane decreases significantly. Also, at very high humidity, the lifetime is very low even when the temperature is relatively low.

Design of a four point bending experiment

Due to the buckling and wrinkling behavior of thin membranes, they cannot be loaded in direct compression as in the traditional material tests. In order to load membrane specimens in alternating tension and compression, the development of a 4-point bending-type testing procedure, the concept of which is shown schematically in Fig. 5.11, is explored.

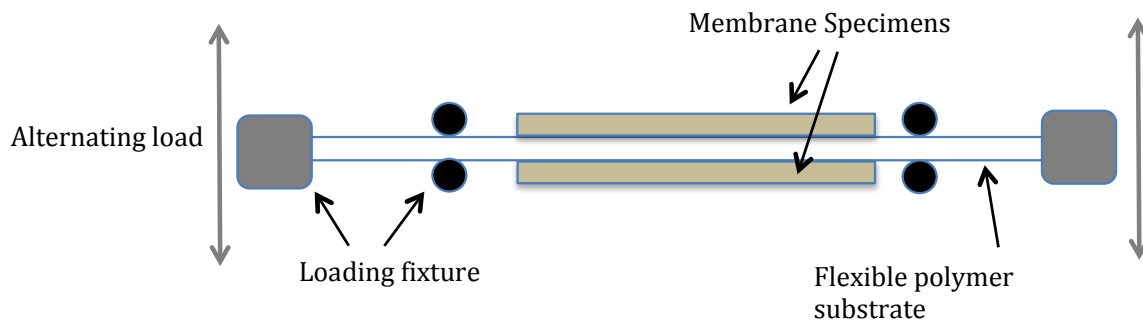


Fig. 5.11: Schematic of bending test configuration

Analysis of four-point bending experiment

From former simulation results, the peak stress that the membrane experiences during fuel cell operation is on the order of 10 MPa. In the following, preliminary analyses are conducted to determine the design parameters needed to load the membrane to this stress level.

To calculate the stress in the membrane in the first design analysis, several assumptions are made:

1. Classical beam theory is applied.
2. Compared with the substrate, the membrane is so thin and flexible that the membrane doesn't affect the response of the substrate.
3. The membrane is mounted perfectly onto the substrate, so the curvature and deflection of the membrane is the same as the outer-most surface of the substrate.
4. In order to calculate the stress in the membrane, classical composite beam theory is applied.

The test configuration can be simplified as shown in Fig. 5.12.

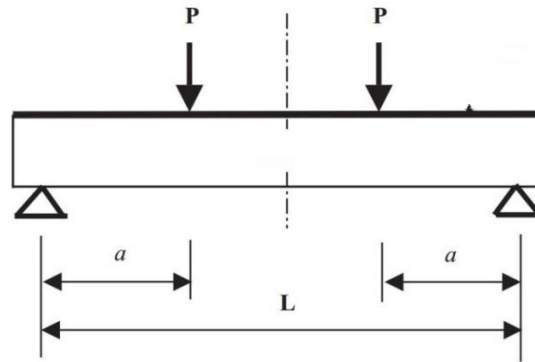


Fig. 5.12: Four point bending configuration

Under assumptions 1, 2 and 3, the deflection of the beam is

$$w = \frac{Pa}{6EI} (3Lx - 3x^2 - a^2) \quad \text{for } a < x < \frac{L}{2} \quad (1)$$

And the maximum deflection is

$$w_{\max} = \frac{Pa}{24EI} (3L^2 - 4a^2) \quad \text{at } x = L/2 \quad (2)$$

Using assumption 4, the stress at the membrane is

$$\sigma_m = E_m \kappa_x \frac{h}{2} \quad (3)$$

Where E_m is the elastic modulus of the membrane, κ_x is the curvature of the membrane and h is the height of the substrate. Therefore with assumption 1 and 3,

$$\kappa_x = -\frac{d^2 w}{dx^2} \quad (4)$$

$$\sigma_m = -E_m \frac{h}{2} \frac{d^2 w}{dx^2} = \frac{E_m}{E} \frac{h}{2} \frac{Pa}{I} \quad (5)$$

Where E is elastic modulus of the substrate and $I = \frac{1}{12}bh^3$ is the second moment of area of the beam's cross-section, where b is the width of the beam.

As is stated before, the desired maximum stress in the membrane is around 10 MPa, so σ_m can be taken as a known parameter and the other parameters such as the applied force and the maximum deflection can be written in terms of this parameter as follows.

$$P = \frac{E}{E_m} \frac{bh^2}{6a} \sigma_m \quad (6)$$

$$w_{\max} = \frac{\sigma_m}{E_m} \frac{3L^2 - 4a^2}{12h} \quad (7)$$

Based on the equations derived above, a sample calculation is conducted choosing the following design parameters: $L=20\text{cm}$, $b=1\text{cm}$, $h=1\text{cm}$, $a=5\text{cm}$ and selecting PTFE (Teflon) as the substrate with elastic modulus of 500MPa. Under this configuration, the force P needed to generate 10MPa in the membrane (elastic modulus of membrane is assumed as 210MPa) is about 80N while the maximum deflection is about 4.5cm.

While this force is possible with standard laboratory equipment, the maximum deflection, if a polymer substrate is chosen, is quite large. In fact a deflection of this magnitude violates the classical beam theory. Therefore, four point bending with large deformation is considered next for the preliminary design. The problem of large deformation in four-point bending is illustrated in Fig. 5.13 [5.1] and modeled in Fig. 5.14 [5.2]. The reference shows a monotonic test but the problem is similar in low-speed cyclic loading.

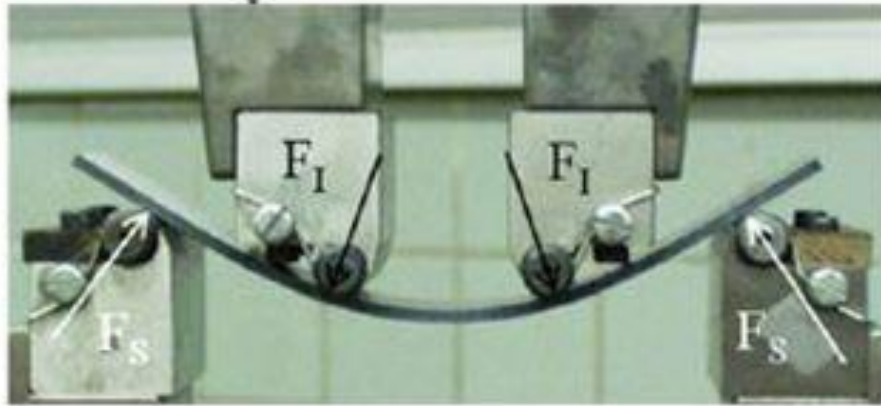


Fig. 5.13: Illustration of four-point bending with large deformation

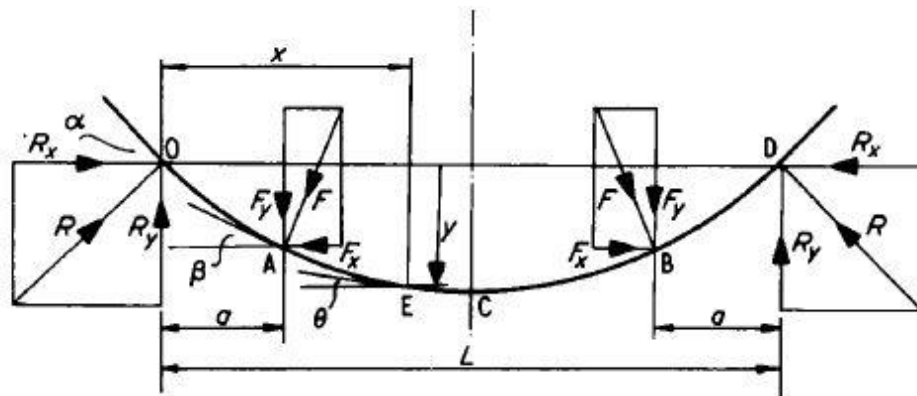


Fig. 5.14: Diagrammatic representation of four-point bending with large deformation

Usually the load points and the simply supported ends use rollers for contact as shown in Fig. 5.13. Due to large deformation, there will be a shift in the point of tangency, relative to the center of the rollers, from the distances between the centers measured before test. This problem is illustrated in Fig. 5.15 [5.3].

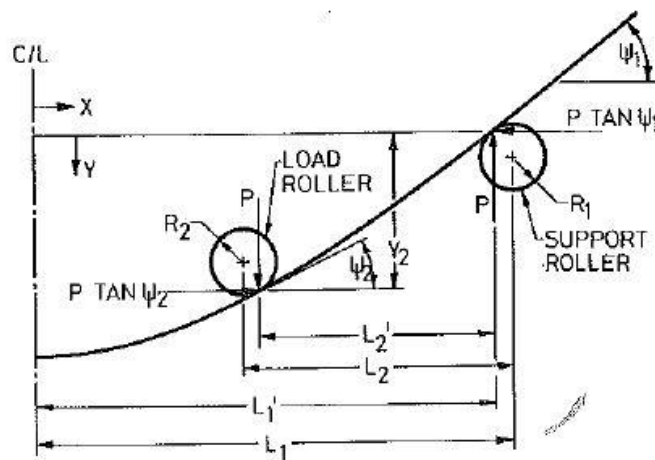


Fig. 5.15: Shifted position of one-half a four-point bending beam

The basic governing equations under large deformation are as follows (assumptions 2-4 still apply):

$$\frac{d^2 y}{dx^2} = \frac{1}{EI} \left[1 + \left(\frac{dy}{dx} \right)^2 \right]^{3/2} P [y \tan \psi_1 - R_1 \sin \psi_1 + L_2 - R_2 \sin \psi_2 - (y - y_2) \tan \psi_2]$$

$$0 \leq x \leq L_1' - L_2', \quad (8)$$

$$\frac{d^2 y}{dx^2} = \frac{1}{EI} \left[1 + \left(\frac{dy}{dx} \right)^2 \right]^{3/2} P [L_1 - R_1 \sin \psi_1 - x + y \tan \psi_1]$$

$$L_1' - L_2' \leq x \leq L_1' \quad (9)$$

where $L_1' = L_1 - R_1 \sin \psi_1$ and $L_2' = L_2 - R_1 \sin \psi_1 - R_2 \sin \psi_2$, and the boundary conditions are $\frac{dy}{dx} = 0 @ x = 0$ and $y = 0 @ x = L_1'$.

The nonlinear differential equations (8) and (9) can be solved numerically and the stress at the membrane can be calculated as

$$\sigma_m = E_m \frac{h}{2} \frac{d^2 y}{dx^2} \quad (10)$$

Therefore, with the analysis above, under certain choices of experiment design, the tension-compression cyclical stress values in the membrane can be controlled and the fatigue life of the membrane under that stress state can be investigated.

Preliminary four-point bend testing

Preliminary tests were conducted to gain more insight into the four point bending test discussed in the previous sub-section. An adhesive-ready PTFE rectangular bar purchased from *mcmaster.com* was used as the substrate beam. The size of the beam is 15 cm long, 1.3 cm wide and 1 cm high as shown in the Fig. 5.16 with the adhesive-ready brown side showing. Hysol® 5 minute epoxy adhesive is used as the bonding adhesive. With careful 'taping', the bonding between the beam and the membrane was determined to be strong enough to last through a number of testing cycles.



Fig. 5.16: Substrate test beams

Due to the lack of a fixture that allows alternating tension-compression cyclic bending on the top and bottom of the beam (see conceptual design of fixture in Fig. 5.11), this preliminary four point bending test was conducted with a regular four point bending fixture that produces tension on the bottom and compression on the top of the substrate beam, as shown in Fig. 5.17. The supporting span is 10 cm and the loading span is 4 cm. Since the stress developed is directly related to the curvature of the beam, displacement control is used. The displacement applied is 1 cm in a sinusoidal wave shape. From a finite element (ABAQUS) simulation, the maximum stress developed in the attached membrane is about 8 MPa (assuming that the membrane is elastic with a modulus of 210 MPa). With this fixture, if the membrane is attached to the bottom surface of the beam it is loaded in tension while if the membrane is attached to the top, it is loaded in compression. For a perfectly elastic beam, the displacement and consequently the stress in the membrane, from this set up would look like the graph shown in Fig. 5.18a. However, due to plastic deformation of the substrate beam the displacement is as shown in Fig. 5.18b.

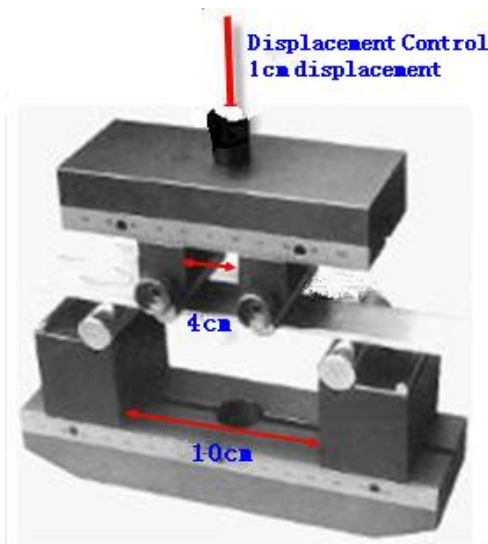


Fig. 5.17: Four point bending fixture

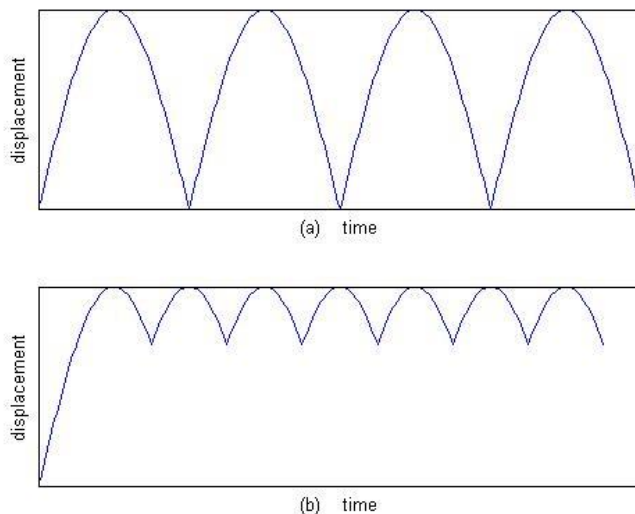


Fig. 5.18: Theoretical and real displacement loading cycles

To develop a method of testing and attaching the membrane to the substrate beam, three separate preliminary tests were conducted:

1) The first test is shown schematically in Fig. 5.19a.

- First a pre-existing crack was created in the membrane and then the membrane was mounted onto the beam with the adhesive.
- The beam was tested for 5000 cycles in total.
 - a) The membrane was loaded in tension for 1200 cycles.
 - b) Then the membrane was loaded in compression for 1200 cycles.
 - c) Then every 200 cycles, the membrane was switched between in tension and compression for a total of 2400 cycles.
 - d) Then the membrane was loaded in tension for 100 cycles
 - e) Then the membrane was loaded in compression for 100 cycles.

After the test, the substrate beam was still intact and the crack in the membrane did not grow, showing that the strength and flexibility of substrate beam may be adequate for the tests, but that the test as conducted may not lead to fatigue failure of the membrane.

2) The second test is shown schematically in Fig. 5.19b.

- First a pre-existing crack was created in membrane and then the membrane was mounted onto the beam with the same adhesive. As shown in the Figure, in the middle of the membrane there is no adhesive.
- For two of these specimens, the membrane breaks in a few cycles in tension.

This attachment method however, was very difficult to implement and does not allow direct compression loading in the membrane sample, since the gauge span “buckles” and deforms away from the substrate beam.

3) The third test was similar to the first test (Fig. 5.19a), but this time the membrane was first mounted onto the beam and then the crack was created with a knife.

- The beam was tested for 4600 cycles in total.
 - a) First the membrane was loaded in tension for 400 cycles and followed by 100 cycles in compression. (Twice)
 - b) Then the membrane was loaded in tension for 800 cycles and followed by 100 cycles in compression. (Four times)

After the test the substrate beam is still intact, but the crack does not grow.

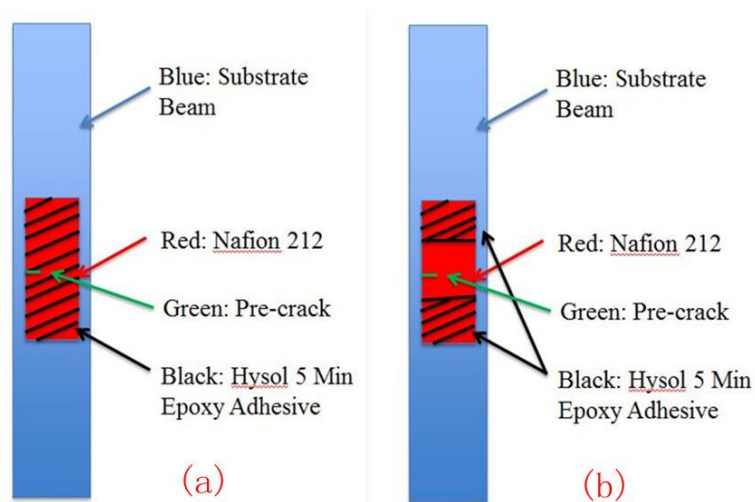


Fig. 5.19: Schematic of attachment of membrane to substrate beam

Since the displacement loading is the same in all three tests, the curvature of the beam is the approximately the same and thus the stress developed in the membrane will be approximately the same. Test 2 indicates that the stress developed is actually large enough to break the membrane. Adhesive may have filled the crack in Tests 1, and 2 and influenced the stresses or the overall behavior of the membrane. Based on the three set of preliminary test, some conclusions and future test ideas were drawn.

Preliminary conclusions for four-point bend testing

From the preliminary design, analysis and testing of the four point bending test, some preliminary conclusions can be drawn.

- The PTFE beam is durable enough and may be a good candidate for use as the substrate beam.
- With a 1 cm displacement control mode, the stress developed can be large enough to break the membrane if the test section is not directly attached to the substrate beam.
- The adhesive seems to have an influence on the behavior of the membrane at the crack and the membrane may have to be loaded through many thousands of cycles to break if the attachment method in Fig. 5.19a is used.
- In the specimens prepared, the thickness of the membrane and adhesive layer were of the same order (about 50 μm). A membrane that is much thicker than the adhesive layer may allow the membrane break sooner.
- A method to observe the crack in the membrane directly must be developed to use this method effectively inside an environmental chamber.
- The design issue of alternating loads, which requires both the loading ends and supporting ends need upper and lower roller needs to be solved.

Numerical model for the fatigue fracture behavior in membrane materials

The previous section discussed preliminary experimental research that has been conducted toward developing an understanding the fatigue fracture behavior of PFSA membrane materials. However, to gain a deeper understanding of the process, and the ability to predict behaviors of untested materials or operating conditions, requires the development of a comprehensive numerical model.

Traditional fracture mechanics approaches

As a starting point, this sub-section discusses traditional fracture mechanics approaches and their applicability to the fatigue fracture of the fuel cell membrane. In the next sub-section, preliminary research into the application of a dissipated plastic energy criterion is discussed.

J-Integral

The widely-used and well-accepted J-integral was originally considered in this study as an appropriate choice for the crack driving force parameter. The J-integral was suggested by J.R. Rice [6.1] and has enjoyed great success as a fracture characterizing parameter. It is analogous to strain energy release rate (and reduces to it, in the case of elastic behavior) but is applicable for cases of non-elastic deformation as well. The J-integral can be calculated directly in ABAQUS and has been used in preliminary simulations. For the region around 2D crack tip, as in Fig. 6.1, the J integral is defined in Equation (1)

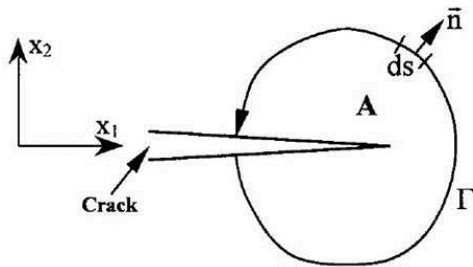


Fig. 6.1: Crack tip in a two-dimensional cracked body

$$J = \int_{\Gamma} \left(W n_1 - \sigma_{ij} n_i \frac{\partial u_j}{\partial x_1} \right) dC \quad (1)$$

However, the traditional J integral as written, can only be applied to homogeneous material domains without thermal and moisture stress and strain. During fuel cell operation, the membrane is hydrated and dehydrated, so moisture and thermal stress and strain have to be considered. In addition, the properties of the membrane depend on RH and temperature. During fuel cell operation, there is often a water content profile through membrane, resulting in a property gradient so the membrane must be also considered to be a non-homogeneous domain (functionally graded material (FGM)) under these conditions.

Therefore, the traditional J integral has to be modified to include the influence of the thermal and moisture strain and the material inhomogeneity due to the material dependence on temperature and RH. Walter et al. [6.2] derived an expression for the modified J integral and it is defined as equation (2) and numerically J can be calculated as equation (3)

$$J = \int_A \left(\sigma_{ij} u_{j,1} - W \delta_{1i} \right) q_{1,i} dA + \int_A \left(\sigma_{ij} \varepsilon_{ij,1}^{total} - W_{,1} \right) q_1 dA \quad (2)$$

$$J = \sum_{elem} \sum_p \left\{ \left[\left(\sigma_{ij} u_{j,1} - W \delta_{1i} \right) q_{1,i} + \left(\sigma_{ij} \varepsilon_{ij,1}^{total} - W_{,1} \right) q \right] \det \left(\frac{\partial X_k}{\partial \eta_l} \right) \right\} w_p \quad (3)$$

The following example shows a simplified FE model of an MEA as illustrated in Fig. 6.2 to simulate a dehydration cycle.

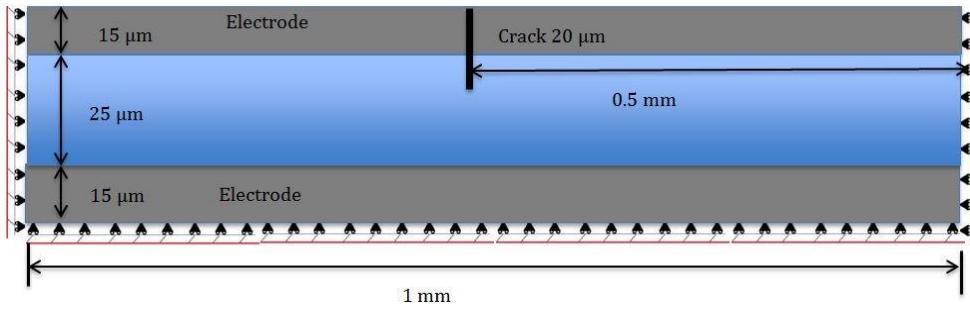


Fig. 6.2: Simplified MEA model under dehydration cycle

Initially the water volume is 0.32 and the temperature is 80 °C throughout the MEA, and two dehydration cases are explored. In one case, the top and bottom edge are dehydrated to 0.06 in 1s, while the temperature is decreased to 25 °C in 1s and held for 10s, to simulate a severe dehydration cycle. In the other case, the MEA is only dehydrated at the top edge. In this preliminary study both the membrane and the electrode are assumed to be linear elastic and the electrode has the same expansion properties as the membrane.

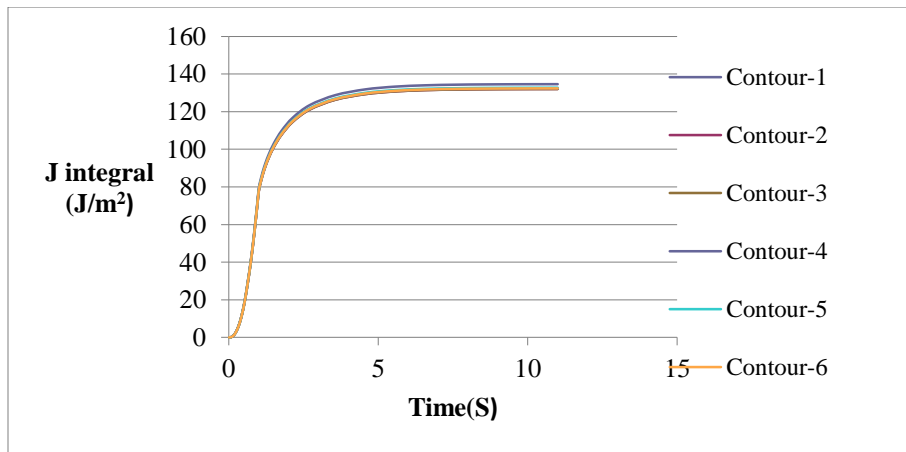


Fig. 6.3: Change of J integral during dehydration when only the top side is dehydrated

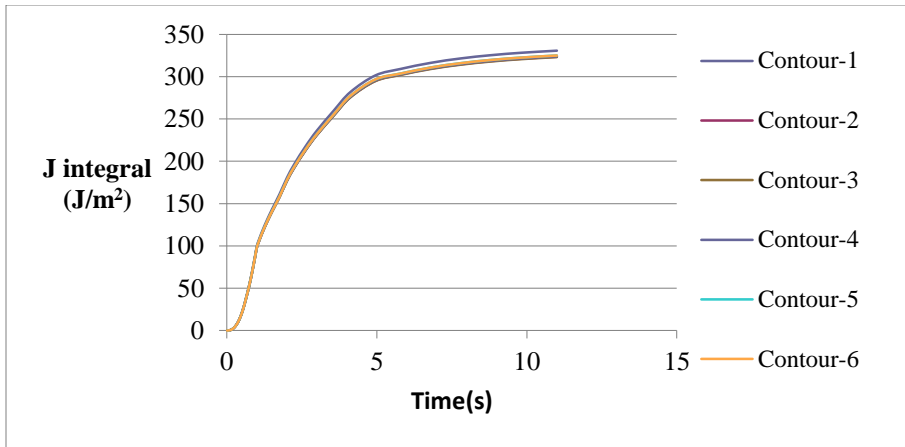


Fig. 6.4: Change of J integral during dehydration when both sides are dehydrated

Fig. 6.3 and 6.4 show that with the method proposed by Walter, the J integral is path independent which makes the J integral a valid crack driving force parameter under these conditions. In addition, the preliminary results show that whether the MEA is dehydrated from one side or from both sides has significant influence on the crack driving force.

These results were obtained for a simplified membrane material response and a simplified fuel cell geometry and loading. However, when the method is applied to calculate the J integral response of a more representative membrane material, in a more representative fuel cell configuration and loading condition, the path independence of the results is seriously violated, which renders the result invalid. By carefully studying the problem, the following conclusions were drawn:

1. The stress developed during hydration generally causes the large regions of the membrane to yield. The large-scale yielding of the membrane violates the assumption of finite-sized yield zone, required for the validity and application of the J integral.
2. While deriving the path independence of the J integral, a small strain condition is assumed. However, due to the relatively large strains developed in the membrane in general, and near the crack tip in particular, the small strain assumption is violated rendering the path independence of the J integral invalid.

Other analytical/numerical methods for fatigue and fracture

There are some other analytical/numerical methods for simulating fatigue and fracture available in literature such as the virtual crack closure technique and the cohesive element. However, unfortunately, due to the special loading conditions and material properties, these traditional numerical methods for fracture are also not applicable in the fuel cell membrane case.

1. Virtual crack closure technique (VCCT)

The virtual crack closure technique states that the work required to extend a crack by an infinitesimal distance is equal to the work required to close the crack to its original length. The virtual crack closure technique has been successfully used to obtain the total strain energy release rate and the mode mixity for cracks in homogeneous materials. It is also extremely useful for cracks along the interface. Wide application of the virtual crack closure can be found in the delamination in laminated composite materials.

However, the virtual crack closure technique is actually based on linear elastic fracture mechanics and therefore requires a small plastic zone to remain valid. As explained above, during the fuel cell operation, large regions of the membrane yield and therefore, the virtual crack closure technique breaks down.

2. Cohesive zone method

The overall yielding of the membrane and the large strain zone around the crack tip are the major obstacles to applying fracture mechanics concepts. However, the cohesive zone method or cohesive element is based on a damage mechanics point of view instead of fracture mechanics. Therefore, the problem associated with the overall yielding and the large strain zone around the crack tip can be avoided. At the core of the cohesive zone method is the traction-separation law, an example of which is shown in Fig. 6.5. The cohesive zone method is usually applied under monotonic loading and in order to handle cyclic loading, unloading-reloading relationship, degradation of the traction-separation law under cyclic subcritical loading and contact under compression need to be added into the cohesive zone mode. The cohesive zone method has been applied to the study the crazing of polymers under model I loading.

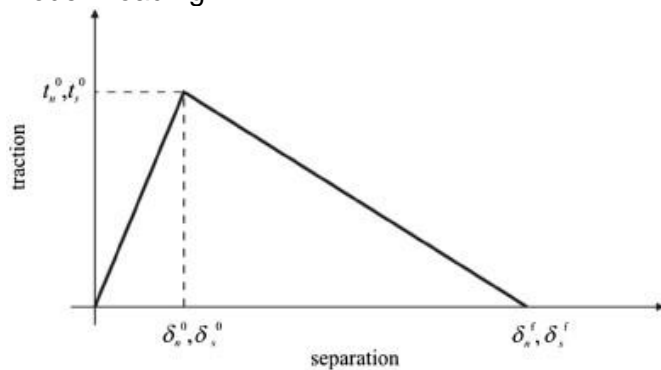


Fig. 6.5: Schematic of traction-separation law for cohesive zone model

However, even though it seems promising, the cohesive zone model is a phenomenological model and contains several parameters that can only be determined from experiments. For Nafion membrane or the PTFE reinforced membrane, currently there is no information regarding these parameters. Consequently another approach to analyzing the fatigue fracture behavior of membrane materials was pursued.

Plastic energy dissipation criteria

The idea of applying the concept of plastically dissipated energy to study fatigue problems dates back to the work of Rice in 1967 [6.3]. Since then, numerous analytical, experimental and numerical investigations have focused on this topic. The plastic energy dissipation is directly linked the accumulation of plastic strain. In metals for example, dislocation motion leads to plastic strain and is directly associated with fatigue. Based on experiments conducted on metals, Ranganathan et al. [6.4] showed that the plastically dissipated criterion energy can be used to determine crack propagation rates under both constant amplitude and variable amplitude cyclic loading. For metals, there is very little time dependency and the plastically dissipated energy can be considered to be the total dissipated energy. However, for polymers, energy is dissipated both viscously and plastically. Lesser [6.5] conducted experiments on two engineering thermoplastics (polyacetal and nylon) and the tensile fatigue behaviors were studied by measuring changes in potential energy density, strain energy density and irreversible work. A subtle but noticeable change in the irreversible work under lower stress levels was observed and based on this it was assumed that the material continually dissipated less energy as it approached failure.

Based on these previous studies, it might be possible to use some form of dissipated energy as a fatigue criteria for PFSA materials. However, further study is needed to investigate what kind of energy dissipation plays the dominant role in the fatigue failure of the membrane.

Plastic energy dissipation behavior at the crack tip

A simplified fuel cell model (Fig. 6.6) is adapted from Dr. Khattri's dissertation [6.6] and the material properties of Nafion® 211 membrane and electrode are assumed to be time dependent. Four, open circuit, hydration-dehydration cycles are applied and the change in plastic energy dissipation for certain selected elements during hydration and dehydration is monitored.

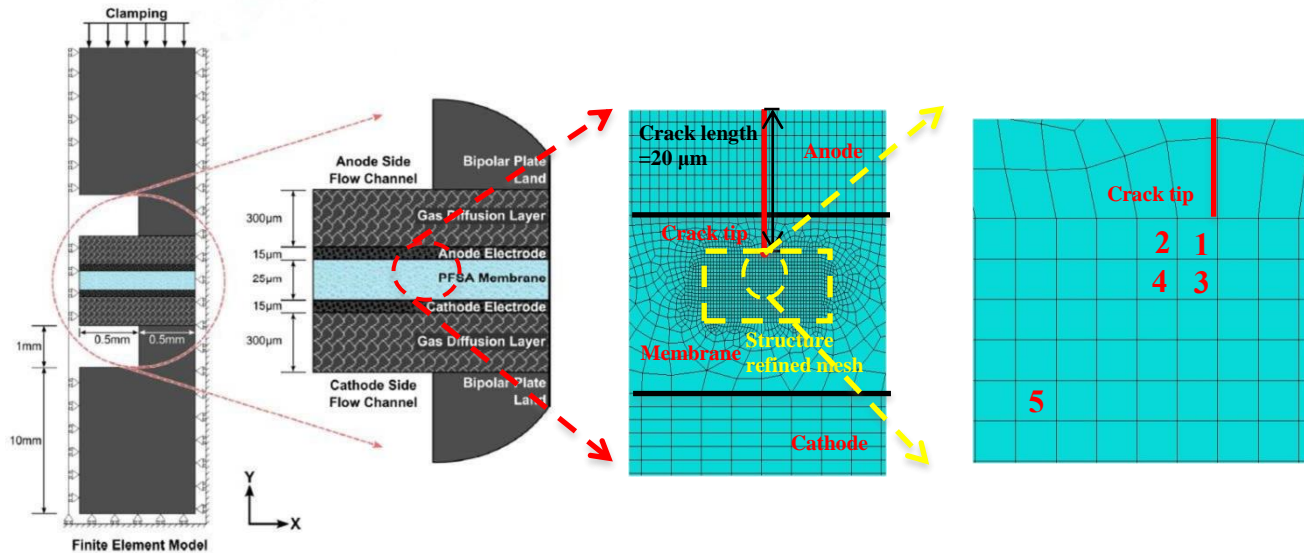


Fig. 6.6: Schematic illustration of the fuel cell model and the element of interest

Fig. 6.7a shows the plastic energy dissipation during the hydration and dehydration cycles in an element that is far away from the crack tip and Fig. 6.7b shows the plastic energy dissipation in several elements near the crack tip.

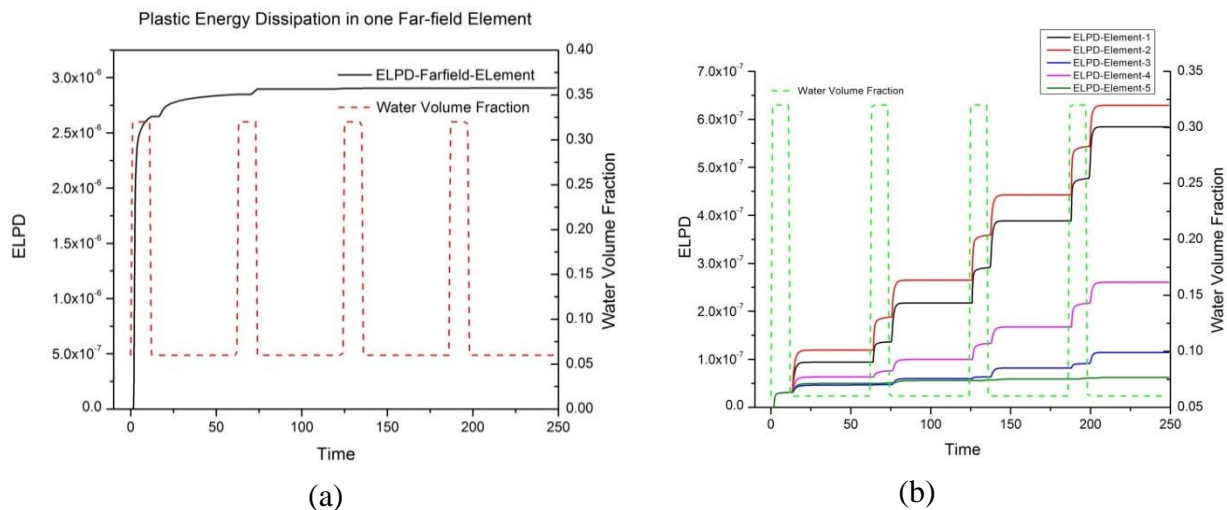


Fig. 6.7: Plastic energy dissipation at different elements during hydration-dehydration cycles

From Fig. 6.7, it can be seen that after the initial cycle, the change of the plastic energy dissipation in the far field is negligible, while at the crack tip there is significant accumulation of plastic energy dissipation during each hydration and dehydration cycle. This indicates that outside of a certain region around crack tip, the accumulation of plastic energy dissipation is quite small and contributes little to the overall change of plastic energy dissipation. Therefore, the plastic energy dissipation might serve as a criterion to assess the fatigue damage accumulation for this kind of material. However, a suitable calculation domain needs to be determined. In the next sub-session the plastic energy dissipation calculation domain around a stationary crack is investigated.

Plastic energy dissipation domain

To effectively use the plastic energy dissipation criterion a calculation domain around the crack tip needs to be established which satisfies several requirements:

1. The domain must be small enough to be sensitive to changes in plastic energy dissipation associated with the crack tip and not capture effects remote to the crack tip.
2. The domain must be large enough to capture most of the plastic energy dissipation associated with the crack.
3. The domain must provide convergence. That is, with a small increase in the size of calculation domain the change in the plastic dissipation within the domain should be small.

The calculation domain can be characterized by domain length, which is the number of elements in the direction perpendicular to the crack, and domain width, which consists of the number of elements in front of the tip and the number of elements behind the tip, as is shown in Fig. 6.8.

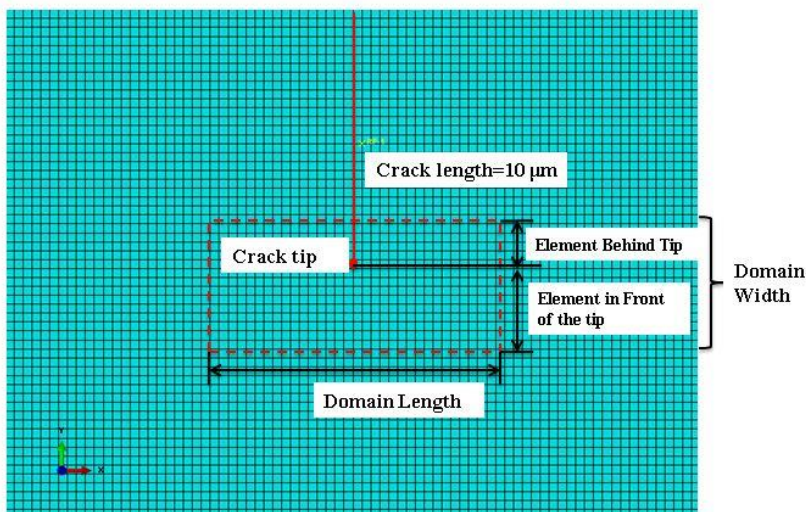


Fig. 6.8: Illustration of energy dissipation calculation domain parameters

To investigate the number of elements needed behind the tip, the length of the calculation domain and the number of elements in front of the tip are fixed. Then, by varying the number of elements behind the crack tip, different calculation domains are established and the change of plastic energy dissipation in the domain during a hydration-dehydration cycle can be calculated. Fig. 6.9a shows the influence of the number of elements behind the tip on domains of length of 40 elements and 20 elements in front of the crack tip and Fig. 6.9b shows the influence on domains with length of 80 elements and 20 elements in front of the crack

tip. From these examples, it can be seen that the number of elements behind the tip has little influence on the plastic energy dissipation in the domains especially in later cycles. Therefore, in the studies to follow, the number of elements behind the tip is chosen to be two.

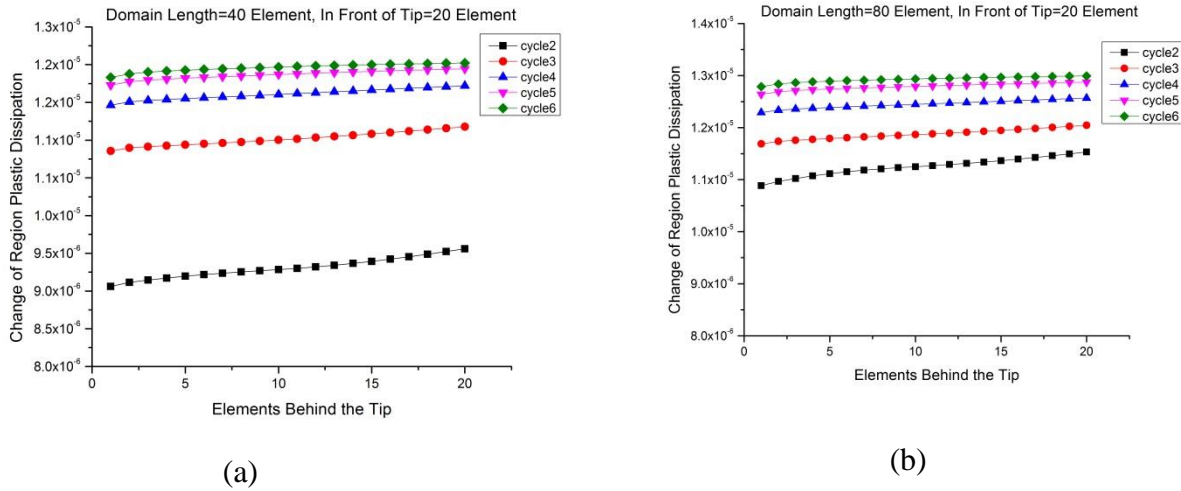


Fig. 6.9: Influence of the number of elements behind the tip on the change of plastic energy dissipation in calculation domain

Next domain convergence was considered. From linear elastic fracture mechanic analysis, the plastic zone shapes in plane stress and plane strain are known to extend much further in the direction perpendicular to the crack than in the direction parallel to the crack. Therefore, in this study the length over width ratio for the calculation domain is chosen to be 2. As has been mentioned above, the domain contains two layers of elements behind the tip. For this study, the initial size of the domain was chosen to be 6 by 3 elements and is increased by one layer of element in width each time (while keeping the length to width ratio of 2). The results are shown in Fig.6.10 for two different crack lengths.

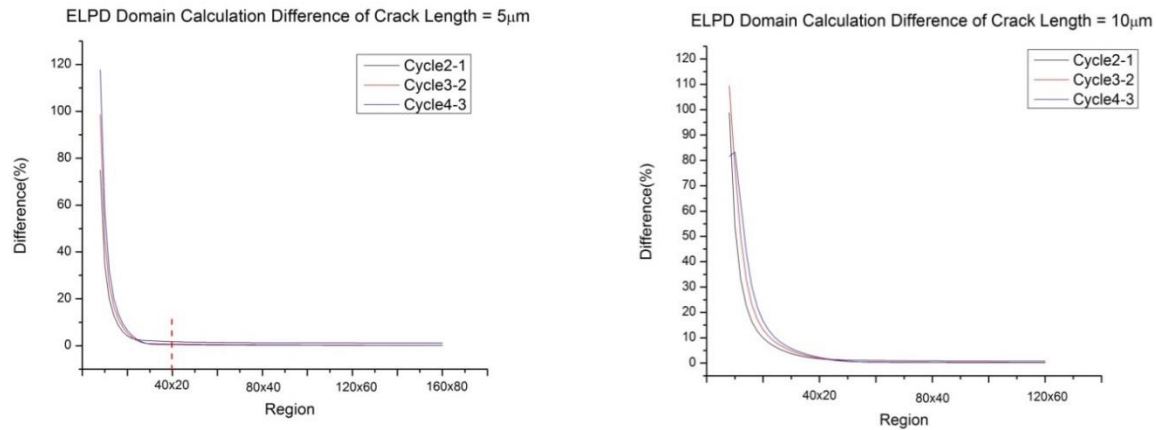


Fig. 6.10: Convergence of plastic energy calculation domain

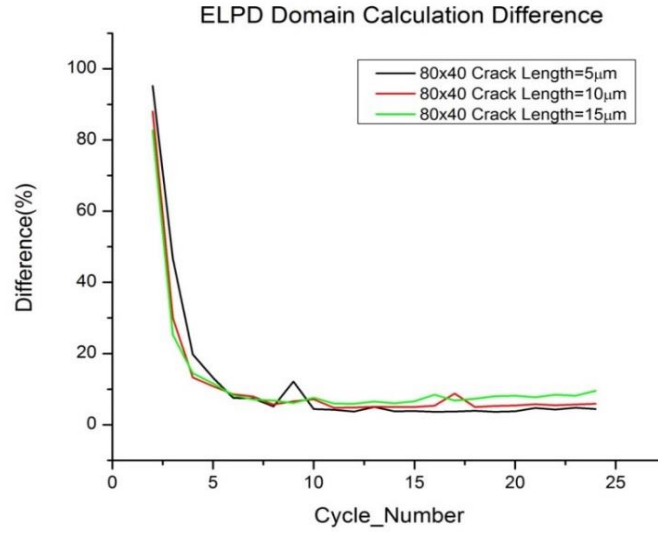


Fig. 6.11: Difference of change in plastic energy dissipation between the whole membrane and the calculation domain

Finally whether the calculation domain is able to capture the total change of plastic energy dissipation in the whole membrane is studied. The difference between the energy dissipation in the calculation domain and the whole membrane is calculated with Equation (5) and the results are shown in Fig. 6.11. With a region of 80 by 40 elements, the calculation domain captures over 90% of the overall plastic energy dissipation in the whole membrane.

$$Difference = 1 - \frac{\text{Change of plastic dissipation in calculation domain}}{\text{Change of plastic dissipation in the whole membrane}} \quad (5)$$

Based on the analysis above, it can be concluded that a suitable calculation domain can be found that is domain-converging and captures most of the plastic energy dissipation in the whole membrane. However, when the crack is long, the size of the calculation will be limited by the number of the elements available in front of the crack tip. In addition, when the crack is long, the influence of the interface between the membrane and the electrode increases. Therefore, future research is required to overcome these barriers.

Conclusion of Mechanical Modeling/Experimentation of Alternative Structures

The modeling work was used to (i) determine the local stresses developing in the materials when subjected to relative humidity and temperature cycling, and (ii) determine crack and damage resistance of proposed MEA designs. The model results were used to guide the preparation of new prototypes (subtask 6.1). Mechanical characterization of reinforced MEAs provided inputs to the mechanical model.

Specifically, tests were conducted to determine the time-dependent mechanical responses of MEA materials; Nafion® 211 membrane, experimental ePTFE-reinforced membrane and MEAs based on Nafion® 211 membranes. The results of these tests were used to develop time, temperature and humidity-dependent constitutive models for the unreinforced and reinforced membranes and the electrodes. In the case of the electrodes, a reverse analysis technique was developed and implemented due to the difficulty in directly testing electrode materials. With the constitutive models in hand, a representative unit volume of an operating fuel cell was numerically simulated to calculate the effect of membrane microstructure (layering) on stresses developed during cyclical loading. Additionally, experimental procedures were developed for fatigue fracture testing of membrane materials, and a series of measurements were made using these procedures. Finally, various fracture techniques were explored for use in modeling the fatigue fracture behavior and the plastic energy dissipation criterion was selected for final evaluation.

Final Project Conclusions

Significant improvements in cost, break-in time, and durability for the key component of fuel cell stacks, membrane electrode assemblies (MEAs) were achieved in this project. Advanced modeling was used to guide design of the new MEA to maximize performance and durability. A new, innovative process and manufacturing approach utilizing direct in-line coating using scalable, cost-competitive, continuous high volume 3-layer rolled-good manufacturing processes was developed and validated by single cell and short stack testing. In addition, the direct coating methods employed were shown to reduce the cost for sacrificial films. Furthermore, Gore has demonstrated a 10 μm reinforced membrane that is used in the new low-cost process and can meet automotive power density and durability targets. Across a wide range of operating conditions, the direct-coated MEA outperformed the commercial baseline MEA, and did so through a process that delivers MEAs at \$92.35 $\$/\text{m}^2$ at a volume of 500,000 systems per year, according to SA estimates. Additionally, the results of this project satisfied the following End of Project Milestones:

- A fuel cell stack was built and tested using Gore's new 3-layer MEA manufacturing process. These MEAs are not only be scalable to potential fuel cell industry MEA volumes in 2015 (estimate 100,000 m^2 / year), but they will also meet or exceed Gore's current power density (950 mA @ 0.6 V under the following conditions: H_2/Air , 1.3/2.0 stoich, 80°C dew points and cell temperature, 0 psig) and durability (Fluoride Release Rate < 1×10^{-7} g/cm 2 *hr, VCD < 50% @ E0.4, HS conditions) standards.
- Cost modeling of the process used to manufacture the MEA indicates >25% cost reduction in high-volume manufacturing of 3-layer MEAs and the process is consistent with achieving DOE's \$9/kW DOE 2017 automotive MEA cost target.

References

- [2.1] Kichenin, J., Van, K. D., and Boytard, K., 1996, "Finite-element simulation of a new two-dissipative mechanisms model for bulk medium-density polyethylene," *Journal of Materials Science*, 31(6), pp. 1653-1661
- [2.2] ABAQUS, 2009, "ABAQUS 6.9 Documentation and User's Manual," ABAQUS Inc.
- [3.1] Z. Lu, M. Lugo, M.H. Santare, A.M. Karlsson, F.C. Busby, P. Walsh, *Journal of Power Sources* 214 (2012) 130-136.
- [3.2] H.P. Yin, A. Ehrlacher, *Mechanics of Materials* 23 (1996) 287-294
- [3.3] W. Ramberg, W.R. Osgood, Description of stress-strain curves by three parameters, Technical Note No. 902, National Advisory Committee For Aeronautics (1943), Washington DC.
- [3.4] N.S. Khattra, A.M. Karlsson, M.H. Santare, P. Walsh, F.C. Busby, *Journal of Power Sources* 214 (2012) 365-376.
- [4.1] Y.L. Tang, M.H. Santare, A.M. Karlsson, S. Cleghorn, W.B. Johnson, *Journal of Fuel Cell Science and Technology*, 3 (2006) 119-124.
- [4.2] M. Griffith, T. Schmiedel, in: ECS Meeting, Honolulu, 2008.
- [4.3] W. Liu, S. Cleghorn, in: ECS Trans., 2006, pp. 263-273.
- [4.4] F.N. Buchi, G.G. Scherer, *Journal of the Electrochemical Society*, 148 (2001) A183-A188.
- [4.5] A. Kusoglu, M.H. Santare, A.M. Karlsson, S. Cleghorn, W.B. Johnson, *Journal of the Electrochemical Society*, 157 (2010) B705-B713.
- [5.1] De Baere I., Van Paepegem W., Degrieck J., Comparison of different setups for fatigue testing of thin composite laminates in bending, *Int J Fatigue*. 2009; 31(6): 1095-101
- [5.2] Paolinelis, S. I., and Ogorkiewicz, R. M., Large deflections of beams in four-point bending, *The Journal of Strain Analysis for Engineering Design*, 1976; 11:144-149
- [5.3] Ritter J.E., Static fatigue of acid-etched, soda-limesilica glass rods [dissertation]. School of Engineering, University of Massachusetts Amherst; 1969
- [6.1] JR Rice, A path independent integral and the approximate analysis of strain concentration by notches and cracks, *Journal of Applied Mechanics*, 35 (1968) 379-386
- [6.2] MC Walters, GH Paulino, RH Dodds Jr., Stress-intensity factors for surface cracks in functionally graded materials under mode-I thermomechanical loading, *Int.J.Solids Structures*. 41 (2004) 1081-1118

- [6.3] JR Rice, Mechanics of crack tip deformation and extension by fatigue, Symposium on fatigue crack growth, ASTM-STP, (1967) 247-311
- [6.4] N. Ranganathan, F Chalon, S Meo, Some aspects of the energy based approach to fatigue crack propagation, Int.J.Fatigue, 30 (2008) 1921-1929
- [6.5] AJ Lesser, Changes in mechanical behavior during fatigue of semicrystalline thermoplastics, Journal of Applied Polymer Science, 58 (1995) 869-879
- [6.6] N. Khattra, University of Delaware Department of Mechanical Engineering, Dissertation 2012

Appendix A: Publications and Patent Applications

2010 Hydrogen Program Annual Merit Review: mn004_busby_2010_o.pdf

2011 Hydrogen Program Annual Merit Review: mn004_busby_2011_o.pdf

2012 Hydrogen Program Annual Merit Review: mn004_busby_2012_o.pdf

2013 Hydrogen Program Annual Merit Review: mn004_busby_2013_o.pdf

2014 Hydrogen Program Annual Merit Review: mn004_busby_2014_o.pdf

Khattra, N.S., Lu, Z., Karlsson, A.M., Santare, M.H., Busby, F.C., Schmiedel, T., "Time-Dependent Mechanical Response of a Composite PFSA Membrane," Journal of Power Sources, v. 228, p. 256-69, 2013

Lu, Z., Lugo, M., Santare, M.H., Karlsson, A.M., Busby, F.C., Walsh, P., "An experimental Investigation of Strain Rate, Temperature and Humidity Effects on the Mechanical Behavior of a PFSA Membrane," Journal of Power Sources, v. 214, p. 130-36, 2012

Khattra, N.S., Karlsson, A.M., Santare, M.H., Walsh, P., Busby, F.C., "Effect of Time-Dependent Material Properties on the Mechanical Behavior of PFSA Membranes Subjected to Humidity Cycling," Journal of Power Sources, v. 214, p. 365-76, 2012

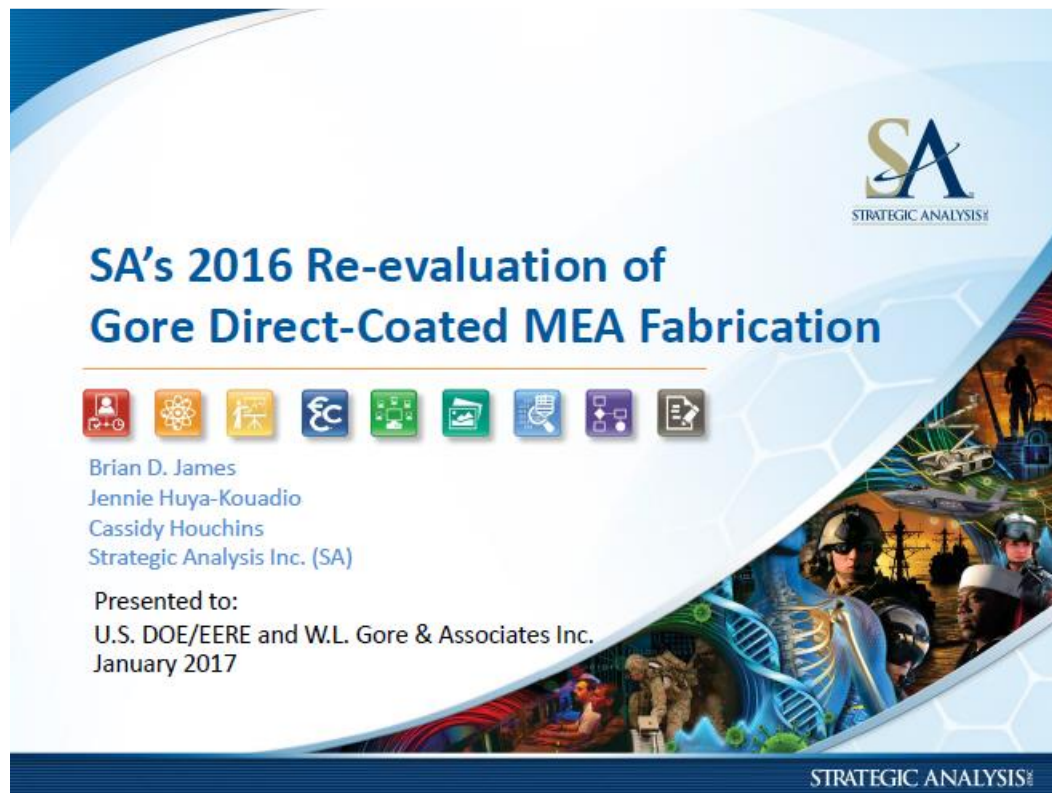
"Time-Dependent Mechanical Behavior of Proton Exchange Membrane Fuel Cell Electrodes" Z. Lu, M. H. Santare, A. M. Karlsson, F. C. Busby, P. Walsh, J. Power Sources, 245, p. 543-552 (2014).

Yasser Ashraf Gandomi, M. D. Edmundson, F. C. Busby, M. M. Mench, "Water Management in Polymer Electrolyte Fuel Cells through Asymmetric Thermal and Mass Transport Engineering of the Micro-Porous Layers", Journal of Electrochemical Society, 163(8), F933-F944 (2016)

Patent application: Membrane Electrode Assembly Manufacturing Process, Colin F. Busby, Donald T. Freese, 10045376-14-0001

Patent application: Membrane Electrode Assembly Manufacturing Process, Colin F. Busby, Mark D. Edmundson, 10045376-16-0001

Appendix B: SA's 2016 Re-evaluation of Gore Direct-Coated MEA Fabrication



The cover features a blue and white hexagonal pattern background. In the top right corner is the Strategic Analysis logo, consisting of the letters 'SA' in a stylized font with 'STRATEGIC ANALYSIS' written below it. The title 'SA's 2016 Re-evaluation of Gore Direct-Coated MEA Fabrication' is prominently displayed in the center. Below the title is a row of ten small, colorful icons representing various fields: a person, a flower, a lightbulb, a gear, a leaf, a book, a magnifying glass, a person in a hard hat, a person in a lab coat, and a person in a military uniform. To the right of these icons is a vertical strip of images showing a person in a hard hat, a person in a lab coat, and a person in a military uniform. At the bottom right, there is a collage of images including a DNA helix, a person in a hard hat, a person in a lab coat, and a person in a military uniform. The Strategic Analysis logo is also present in the bottom right corner.

**SA's 2016 Re-evaluation of
Gore Direct-Coated MEA Fabrication**

Brian D. James
Jennie Huya-Kouadio
Cassidy Houchins
Strategic Analysis Inc. (SA)

Presented to:
U.S. DOE/EERE and W.L. Gore & Associates Inc.
January 2017

STRATEGIC ANALYSIS®

Overview of Changes since 2013 SA Analysis

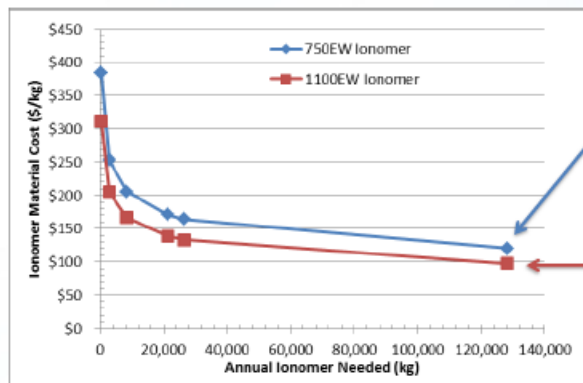
- SA conducted a 2013 analysis of the Gore direct-coated MEA fabrication process. A re-examination was conducted in 2016 to incorporate process improvements.
- Updates to equipment capital cost to reflect recent slot die coating quotations and to model membrane formation as two separately slot die-cast and dried ionomer layers.*
- Changed from 2 workers for 3 lines to 1 worker per line.
- Addition of XRF to coating line QC.
- Updated clean room costs for ISO 5.
- Addition of d-PtNi catalyst processing cost built into catalyst price. (Previously only the catalyst raw material costs had been included.)
- Adjustment of markup to include building costs and to include costs for security and safety protocols in handling catalyst material.
- Re-evaluated material and processing losses, incorporating explicit estimation of fluid, edge, and startup/shutdown losses.
- Update to Ionomer cost to account for lower equivalent weight (as more commonly used in current systems).

* Gore's Recent Patent Application: US 2016 233532 A1

Remaining Issues/Concerns

- Gore notes that SA estimated ionomer costs are based on 6+ year old study and are significantly lower than current industry expectations. Industry specifications and manufacturing assumptions have changed, and ionomer cost could vary significantly as a result.
 - Current ionomers typically have lower equivalent weight (EW) (700-850 EW vs. previously modeled 1,100 EW).
 - With lower EW, the HFPO content within the ionomer is higher and HFPO now makes up a majority of the raw material cost within the ionomer.
 - Gore cannot share ionomer prices with SA.
 - In the interim, SA is using a cost factor of 1.23 to adjust ionomer cost for lower EW (see next slide).
- Gore suggests lower costs can be achieved by coating the electrodes and membrane directly onto the GDL (instead of coating onto a backing layer and then combining with the GDLs). However, coating defects from GDL particulation are a concern/uncertainty. Thus, SA does not currently model coating on a GDL substrate.
- Plate frame (ionomer) membrane humidifiers may not be feasible for fuel cell systems due to membrane degradation caused by air-borne ammonia. Typical ammonia levels (found in highway air, particularly behind trucks) will cause unacceptable rates of membrane performance degradation, forcing the membrane to be replaced or regenerated regularly. Some auto industry leaders are moving away from external humidifiers. This affects the amount and cost of ionomer production.

Change in Ionomer Material Cost



Updated curve
fit for 750 EW
ionomer

SA curve fit to
cost from GM's
2010 report for
1,100 EW

Assumed Ionomer Cost in Model (Updated)
\$120 - \$383/kg (depending of production rate)

Applied 1.23 factor to Ionomer cost for a simplified scaling of equivalent weight:

$$\text{Cost(EW)} = \text{Cost}(1,100 \text{ EW}) * 0.5 * \left[1 + \left(\frac{1,100}{\text{EW}} \right) \right]$$

- At 750EW, $\text{Cost}(750\text{EW}) = \text{Cost}(1100\text{EW}) * 1.23$
- Does not yet take into account additional processes required in current ionomers.

4

STRATEGIC ANALYSIS®

Key Assumptions/Caveats for 2016 Gore Direct-Coated MEA Fabrication Cost Analysis

- Based on:
 - SA interpretation of Gore direct-coat MEA fabrication methods
 - Publicly available, non-proprietary information
 - Gore Patents (US 2016 233532 A1, USRE37307)
- Simple integration into SA 80kW fuel cell cost model
 - Replaces previously modeled membrane:
 - Membrane fabrication: Multiple dip coatings of ionomer on ePTFE, infrared drying in between, boiling water hydration bath, and air dry
 - Catalyst application: dispersed d-PtNi catalyst
 - Based on 749 mW/cm² at newly optimized 2016 stack conditions
 - 2.5 atm (stack operation)
 - 0.134 mgPt/cm² (0.0182 on anode and 0.116 on cathode)
 - 1.4 air stoichiometry
- SA's estimate assumes coating the first electrode layer onto a re-useable backer material rather than a GDL material.

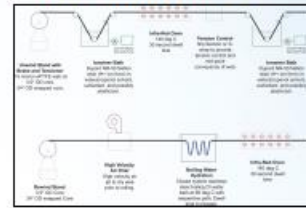
5

STRATEGIC ANALYSIS®

SA Baseline Membrane Electrode Assembly (MEA) Process (for comparison to Gore Direct-Coated MEA process)

- **Membrane Fabrication**
 - Roll-to-Roll process
 - Dip-coating to occlude pores of ePTFE substrate
- **MEA Formation**
 - Dual-sided Slot Die Coating (Horizontal) onto membrane
 - Anode and cathode coated on single line
 - GDL attachment as part of sub-gasket process

2016 Baseline Membrane Fab.



2016 Baseline MEA Fab.



6

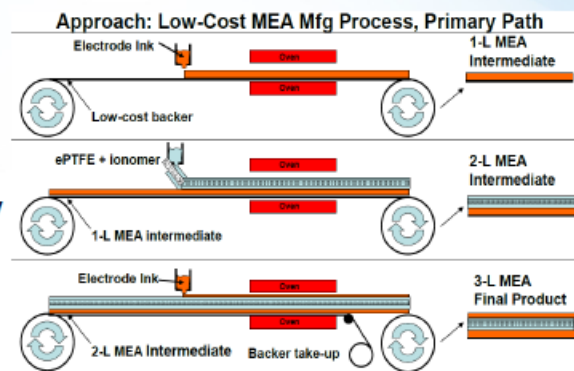
STRATEGIC ANALYSIS®

Gore Direct-Coated MEA Manufacturing Process Description

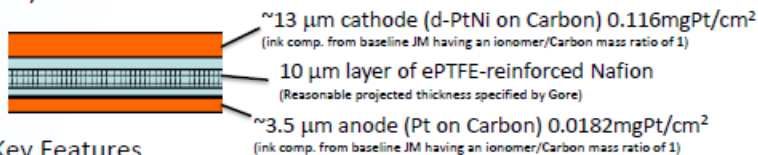
Station 1: Anode Application

Station 2: Membrane Applied to Anode (two separately dried ionomer layers)

Station 3: Cathode Application



• 3-Layer MEA Finished Product



• Key Features

- Rapid, Roll-to-Roll based deposition (10+ meters/min web speed)
- No vacuum processes

7

STRATEGIC ANALYSIS®

Width of R2R Machinery Changes with Production Volume (width optimized to return lowest MEA cost)

Production Volume (sys/yr)	1,000	10,000	30,000	80,000	100,000	500,000
Production Volume (m ² active area/yr)	11,706	117,059	351,178	936,475	1,170,594	5,852,968
Coating Machine	Lab Coater	Pilot Coater	Pilot Coater	Production Coater	Production Coater	Production Coater
Process Width (cm)	25.5	45.5	45.5	90.5	90.5	90.5
Process line design rate (m/min)	3 (elect.) 0.8 (mem.)	16.5 (elect.) 2 (mem.)	16.5 (elect.) 4 (mem.)	25 (elect.) 4 (mem.)	25 (elect.) 6 (mem.)	25 (elect.) 19 (mem.)
Number of Simultaneous Lines Needed for stated prod. volume	1	1	1	1	1	1

page 8

STRATEGIC ANALYSIS®

Direct-Coated MEA Key Parameters (at 500k/yr)

**All Values at 500k sys/yr		Anode Fabrication (Station 1)	Membrane Fabrication (Station 2)	Cathode Fabrication (Station 3)
Oven Residence Time (oven length)	Minutes (meters)	0.3 (7.5)	1 st Oven: 3 (19) 2 nd Oven: 2.7 (72)	0.6 (15)
Line Capital Cost (w/o XRF)	\$M	3.4	12	4.1
Line Power (elect.)	kW	204	549	375
System Lifetime	years	11	14	11
Line speed	meters/min	25	19	25
Web Width	cm	91	91	91
Labor	workers/line	1	1	1
Type of Quality Control		Infrared/Direct Current (IR/DC), XRF, ultrasonic thickness gauge	Optical Detection System (20µm resolution)	IR/DC, XRF, ultrasonic thickness gauge
Material Prices				
ePTFE	\$/m2	NA	6	NA
ePTFE-like backer	\$/m2	1.50	NA	NA
Nafion	\$/kg	120	120	120
Catalyst (Pt/C - anode and D-PtNi - cathode)	\$/kg	10,875	NA	15,167
Solvent (25% methanol /75% DI water)	\$/kg	1.45	NA	1.45

9 5/8/2017

STRATEGIC ANALYSIS®

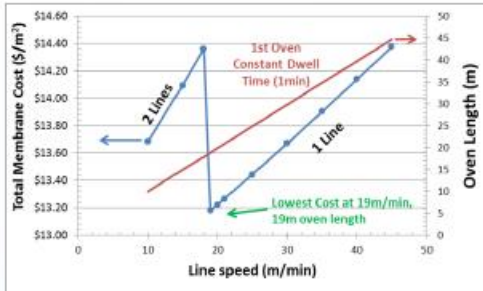
Parametric Study to Minimize Station Cost

Trade-off of speed, length, and # of lines

Membrane Fabrication at 500k systems/year

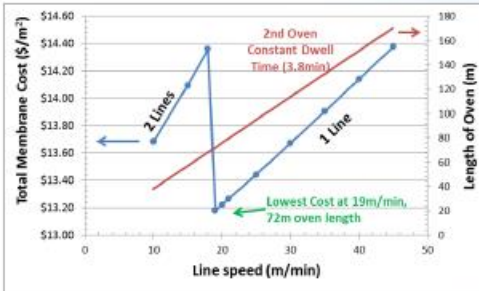
Given constant oven dwell time, find lowest cost of membrane line

Example: 1st Dryer of Station 2



- 19m/min line speed
- 22m oven length
- \$1.65M oven cost

Example: 2nd Dryer of Station 2



- 19m/min line speed
- 72m oven length
- \$4.8M oven cost

page
10

STRATEGIC ANALYSIS®

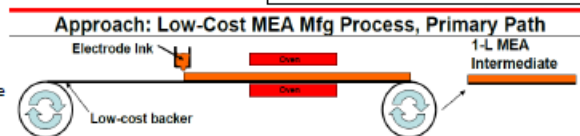
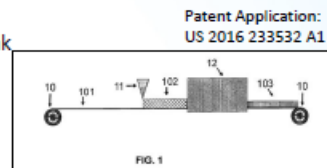
Changes to Capital Cost Assumptions

	Anode Fabrication (Station 1)	Electrolyte Fabrication (Station 2)	Cathode Fabrication (Station 3)	Total
2013 Capital Costs	\$1.4M	\$2.1M	\$1.4M	\$4.9M
List of Components	\$700k Slot Die Coater (10m/min) -1m width -7m long oven -ultrasonic mixer \$210k IR/DC QC system \$55k Clean Room 367ft ² \$482k (50% cost margin)	\$700k Slot Die Coater (10m/min) -1m width -7m long oven -ultrasonic mixer \$47k for additional oven 33m length oven / 5 turns =33m/5 x \$7k/m \$60k ePTFE unwind stand and tensioner \$51k for additional slot die \$25k Ionomer Pump Cart \$392k ODS QC system \$126k Clean Room 845ft ² \$700k (50% margin)	(Same as Anode) \$700k Slot Die Coater (10m/min) -1m width -7m long oven -ultrasonic mixer \$210k IR/DC QC system \$55k Clean Room 367ft ² \$482k (50% cost margin)	
2016 Capital Cost (w/out XRF)	\$3.4M	\$12M	\$4.1M	\$19.5M
List of Components	\$2.4M Slot Die Coater (25m/min) -0.9m width -7.5m oven length \$11k High shear mixer \$210 IR/DC QC System \$762k Clean Room 1,451ft ²	\$2.4M for 2x Slot Die Coaters (19m/min) (excludes ovens) -0.9m width \$50k for 2x Ionomer Pump Carts \$1.2M 1 st Ionomer Coat Oven (19m) \$4.8M 2 nd Ionomer Coat Oven (72m) \$189k ODS QC System \$3.4M Clean Room 6,504ft ²	\$2.9M Slot Die Coater (25m/min) -0.9m width -15m oven length \$15k High shear mixer \$210 IR/DC QC \$985k Clean Room 1,876ft ²	
Changes Highlighted	2013 slot die cost may not have been for FC specs, single sided oven 5x the area (membrane/cathode) and twice as fast (twice as long), clean room sizing (added 1.5 multiplier onto machine area to allow space around machine) and cost per ft ² increased to \$525/ft ² to reflect ISO 5.			

page 11

Station 1: Anode Application

- Line Capital (at High Production Volume, 0.9m web width)
 - \$11k Silverson Benchtop High Shear Mixer L5MA (\$6k for machine +\$5k for clean equip.)
 - \$1.5M Web Handling (unwind, tension control, rewind)
 - \$400k Coating Station (frame, backing roll, slot die & fluid delivery)
 - \$500k Dryer (3 zone, supply & exhaust fans, 7.5m long, 0.9m width, 25m/min, 18sec dwell time)
 - \$210k IR/DC QC
 - \$762k Clean Room (~135m², ISO 5 @\$5.6k/m²)
 - \$3.4M Total
 - Plus XRF for QC (cost is proprietary)
- Catalyst Ink Composition (from Baseline – JM, ionomer/Carbon ratio of 1)
 - Pt/C catalyst powder (Pt 20wt%, carbon 80wt%), 15wt% of catalyst ink
 - Nafion, 12wt% of catalyst ink
 - Solvent (25% methanol, 75% DI water), 73wt% of catalyst ink
- ePTFE-like Low-Cost Composite Backer (25 µm thick)
 - \$1.50/m² (\$1-2/m² provided by Gore)*
 - Backer width: 0.9 m
 - Backer length: 500 meters
 - Reused 5 times



* Busby, C., "Manufacturing of Low-Cost, durable Membrane Electrode Assemblies Engineered for Rapid conditioning", FCTO Annual Merit Review Presentation, 2012.

12

STRATEGIC ANALYSIS®

Station 1: Anode Application (continued)

Quality Control Equipment

- IR/DC Quality Control System
 - Based on Mike Ulsh/NREL work
 - Infrared/Direct-Current (IR/DC) detection system
 - Detects anomalies in electrical conductivity of electrode layer
 - Demonstrated at NREL at 20m/min with ~2mm defect resolution
- XRF (X-ray Fluorescence)
 - Observation of composition of catalyst and Pt loading
- Ultrasonic Thickness Gauge

Installation Cost

- 40% of total capital cost assumed
 - Includes physical equipment installation
 - Includes \$300k Installation "Labor" Services provided by coating machine supplier: 35-77man days (travel + time)
 - installation supervision, start-up, training, Not installation of equip.

page
13

STRATEGIC ANALYSIS®

Station 2: Membrane Fabrication

Line Capital (modeled as single continuous line of two coating stations)

- 1st Coating Line
 - \$750k Web Handling (unwind, tension control)
 - \$25k for Ionomer Pump cart (& Ultrasonic Mixer)
 - \$400k for Coating Station (frame, backing roll, slot die, fluid delivery)
 - \$1.2M 1st Ionomer Coat Dryer (\$66.6k/m, 19m long, 19m/min, 1 min dwell)
 - 2nd Coating Line
 - \$750k Web Handling (tension control, rewind)
 - \$25k for Ionomer Pump cart (& Ultrasonic Mixer)
 - \$50k laydown roll for ePTFE
 - \$400k for Coating Station (frame, backing roll, slot die, fluid delivery)
 - \$4.8M 2nd Ionomer Coat Dryer (\$66.6k/m, 72m long, 19m/min, 3.8 min dwell)
 - \$189k Optical Detection System
 - \$3.4M Clean Room
 - \$12M Total
- 1st Ionomer Coat, then dry (1 μ m), followed by 2nd Ionomer Coat and lay down of ePTFE (fully submerged in Ionomer), then dry (9 μ m)
- ePTFE Substrate: 7 μ m thick @ 95% porosity (assume 1 μ m Ionomer below and 2 μ m of Ionomer above ePTFE get a total of 10 μ m thickness)

Ionomer Solution Composition

1st protective Ionomer solution:

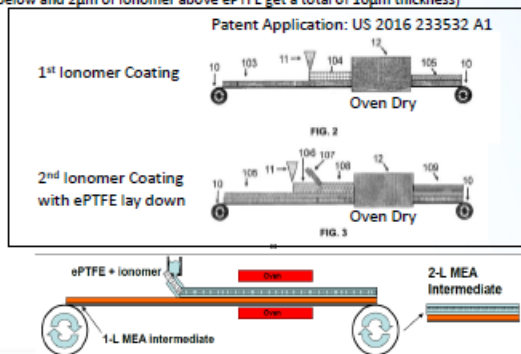
- 5wt% Nafion
- 90wt% water
- 5% mixture of hexanol and isopropanol

2nd Ionomer solution:

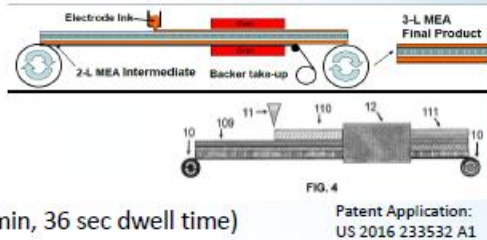
- 5wt% Nafion
- 47.5wt% isopropanol
- 47.5wt% methanol

Cost model drying times

- 1min (1st coat) + 3.8min (2nd coat) = 4.8 minutes total
- @ 140°C (Gore patent application)



Station 3: Cathode Application



- Same equipment as Station 1 (Anode)

Exceptions:

- \$15k Silverson In-Line mixer (1 gal/min)
- \$1M Dryer (15m long, 0.9m wide, 25m/min, 36 sec dwell time)

- Catalyst ink loading: 0.116 mgPt/cm²

- d-PtNi catalyst powder (29wt%Pt, 67wt% carbon, 5% Nickel), 15wt% of catalyst ink
- Nafion, 10wt% of catalyst ink
- Solvent (25wt% methanol and 75wt% DI water), 75wt% of catalyst ink

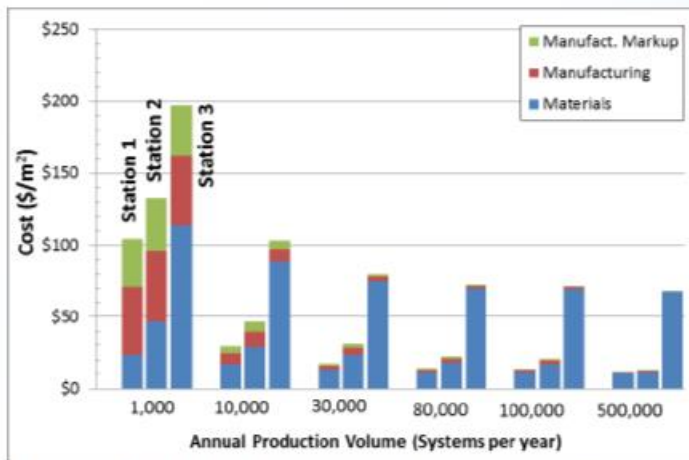
Additional Assumptions for Gore Direct-Coated MEA Stations

- Cell sizes
 - Automatically calculates orientation of cells to provide maximum usage of web width
 - Active area: ~14cm x 21cm
- Labor Rate: \$48/hr @ 1 laborer per station

15

STRATEGIC ANALYSIS®

Cost Results for Gore Direct-Coated MEAs



- Station 3 materials higher than Station 1 materials due to higher Pt loading.
- Stations 1 & 3 material cost change across manuf. rates (because of catalyst markup)
- Ionomer material costs are high at low manuf. rates due to low yields.
- Material cost much higher than manufacturing costs.

16

STRATEGIC ANALYSIS®

2016 Tabular Cost Results for Gore Direct-Coated MEAs (10µm thick membrane)

Cost Results, \$/m²

	Cost of Gore Direct-Coat MEA (\$/m ²)					
System per Year	1,000	10,000	30,000	80,000	100,000	500,000
Areal Production (m ² active area/year)	11,706	117,059	351,178	936,475	1,170,594	5,852,968
Station 1 Materials	\$23.39	\$16.70	\$12.91	\$11.64	\$11.50	\$11.05
Station 2 Materials	\$46.43	\$28.94	\$23.28	\$18.15	\$17.10	\$11.74
Station 3 Materials	\$113.32	\$88.56	\$74.88	\$69.28	\$68.98	\$67.09
Subtotal Materials	\$183.14	\$134.19	\$111.07	\$99.06	\$97.58	\$89.88
Station 1 Manufact.	\$0.00	\$0.00	\$0.00	\$0.00	\$0.00	\$0.00
Station 2 Manufact.	\$47.22	\$7.64	\$2.83	\$1.85	\$1.35	\$0.40
Station 3 Manufact.	\$49.33	\$10.71	\$4.97	\$2.77	\$2.49	\$0.98
Subtotal Manufact.	\$145.08	\$27.12	\$10.92	\$6.21	\$5.29	\$1.73
Station 1 Markup	\$0.00	\$0.00	\$0.00	\$0.00	\$0.00	\$0.00
Station 2 Markup	\$33.47	\$4.80	\$1.57	\$0.83	\$0.66	\$0.13
Station 3 Markup	\$36.27	\$6.86	\$2.92	\$1.49	\$1.33	\$0.45
Subtotal Markup	\$104.38	\$17.34	\$6.33	\$3.31	\$2.77	\$0.74
Station 1 Total	\$104.08	\$29.14	\$17.31	\$14.12	\$13.51	\$11.58
Station 2 Total	\$132.03	\$46.51	\$31.17	\$22.40	\$20.92	\$13.17
Station 3 Total	\$196.49	\$103.00	\$79.84	\$72.06	\$71.21	\$67.60
Total	\$432.61	\$178.65	\$128.32	\$108.58	\$105.64	\$92.35

11.7m²_{active_area} per 80kW_{net} system.

Based on 749 mW/cm² stack power density.

Total
processing
cost

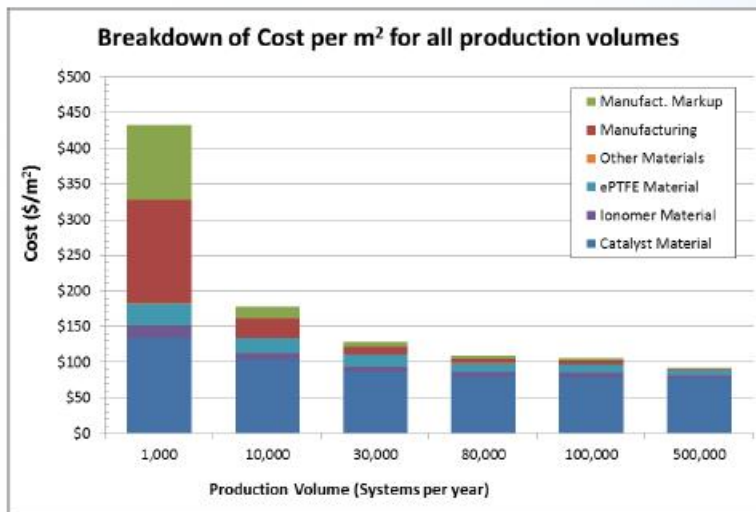
Total
membrane
cost

Total 3-layer
MEA cost
(including
catalyst)

17

STRATEGIC ANALYSIS®

2016 Cost Results for Gore Direct-Coated MEAs



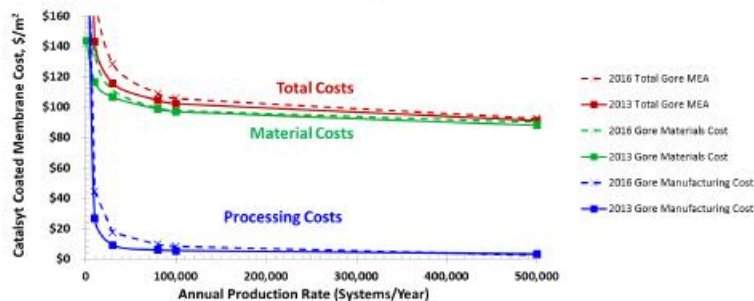
- Catalyst material costs dominate total cost.
- ePTFE cost is greater than the ionomer cost
- Manufacturing cost only \$1.73/m² (at 500k/yr)

18

STRATEGIC ANALYSIS®

Comparison to 2013 Gore Direct-Coat MEA Analysis

SA's 2013 vs. 2016 Analysis of Gore Direct-Coat MEA



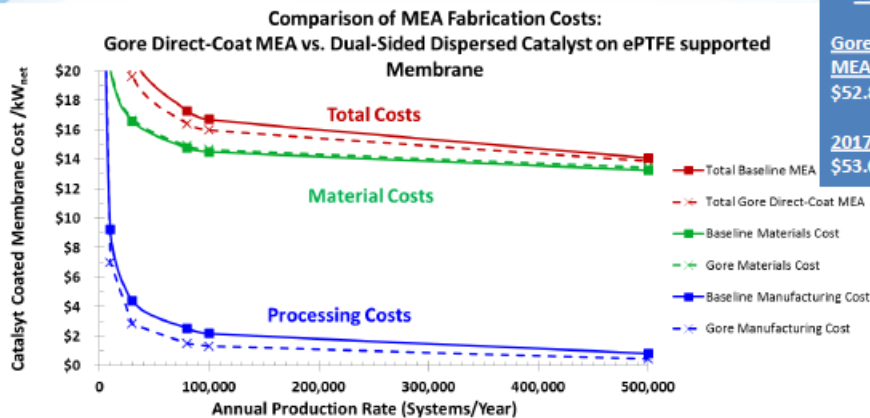
Differing Parameters	2013 Analysis	2016 Analysis	Effect on 2016 Cost
Membrane Area per Stack	12.93m²	11.71m²	Material Cost ↑ Processing Cost ↑
Membrane Thickness	15 microns	10 microns	Material Cost ↓
Ionomer EW & Cost (500k sys/yr)	EW Not specified (\$85/kg)	750EW (\$120/kg)	Material Cost ↑
Catalyst Processing Cost	Not Accounted For	\$1.20/m²	Material Cost ↑
Capital Cost of Equipment	\$5M	\$20M	Processing Cost ↑
Line Speed	10m/min	19-25m/min	Processing Cost ↓
Overall Cost at 500k sys/yr	\$91.07/m²	\$92.35/m²	

Although there are many parameters that changed between 2013 and 2016 analyses, the overall cost did not change more than 2% at 500k sys/yr. The small increase for 2016 reflects more accurate ionomer and capital costs, and reflects a better representation of the Gore Direct-Coat MEA process based on their patent application.

page 19

STRATEGIC ANALYSIS®

Gore Direct-Coat MEAs and Baseline Catalyst Coated Membrane are expected to have similar costs



Total System Cost

Gore Direct-Coated
MEA system:
\$52.80/kW_{net}

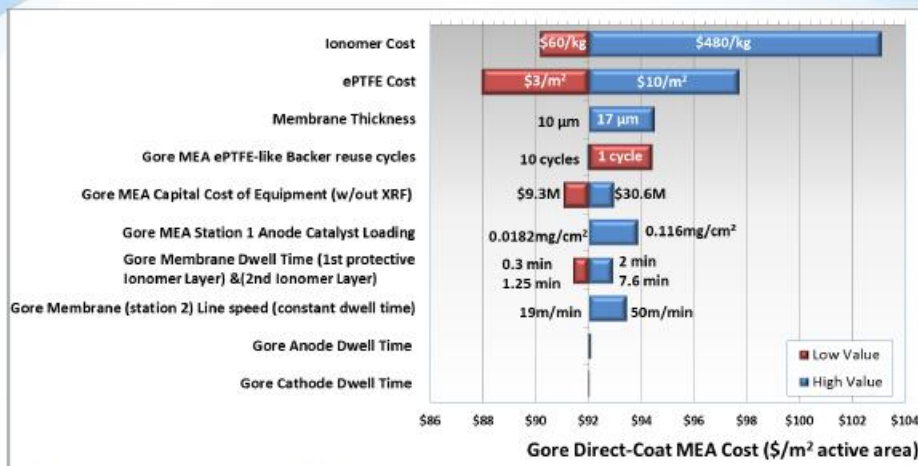
2017 Baseline System:
\$53.01/kW_{net}

- Material costs are about the same (since both are dominated by Pt cost)
- Both membranes are normalized to 17microns thickness, 750EW ionomer (for this slide and the next slide only)
- Gore processing costs are expected to be lower due to simpler membrane manufacturing
- Total costs differ by \$0.21/kW (at 500k/year)
- Assumes identical power density for both systems. Differences in polarization performance will change costs relative to each other.

20

STRATEGIC ANALYSIS®

MEA Sensitivity (at 500k sys/yr)



- Top three cost uncertainties:
 - Ionomer cost
 - ePTFE cost
 - Membrane Thickness
- None the less, MEA uncertainty is still only ~+6%, -4% for each variable.
- Caveat: MEA performance assumed to equal that of Baseline model

21

STRATEGIC ANALYSIS®

Tornado Chart Bounds

Gore Direct-Coat MEA Sensitivity Limits for Tornado Chart					Rationale
Parameter	Units	Low Value	Base Value	High Value	
Ionomer Cost	Multiplier (\$/kg)	0.5 (\$60)	1 (\$120)	4 (\$480)	Membrane material costs vary significantly.
ePTFE Cost	\$/m²	3	6	10.2	Based on Cost range provided by industry quotes with min of half the cost and a max of 1.7x
Membrane Thickness	microns	-	10	17	
Gore MEA ePTFE-like Backer reuse cycles	cycles	1	5	10	Engineering judgement to capture range of potential reuse cycles.
Gore MEA Capital Cost of Equipment (w/out XRF)	Multiplier (\$)	0.5 (\$9.3M)	1 (\$20M)	1.5 (\$30.6M)	Base value based on summation of individual manufacturing equipment components, but w/out XRF.
Gore MEA Station 1 Anode Catalyst Loading	mg/cm²	0.182	0.0182	0.116	The "base value" of 0.0182 mgPt/cm² considers the Gore MEA station 1 to be the application of the anode, while the catalyst loading of 0.116 mgPt/cm² considers the Gore MEA station 1 to be the application of the cathode.
Gore Membrane Oven Dwell Time (1st protective Ionomer Layer) & (2nd Ionomer Layer)	Multiplier (min)	0.3 (0.3) 0.3 (1.25)	1 (1) 1 (3.8)	2 (2) 2 (7.6)	From DuPont Patent US 7,648,660 B2: oven drying times are between 1 and 3 minutes for each of the three heating zones for a hot air convection oven. At the "base value" the dwell times are ~5 minutes total.
Gore Membrane (station 2) Line speed (constant oven dwell time)	m/min	19	19	50	DuPont Patent US 7,648,660 B2 states 3 m/min to be the upper end of the most preferred line speed. 19m/min chosen as lowest cost. Anything above or below results in a higher cost. Gore thinks 50m/min is what is reasonable today.
Gore Anode Oven Dwell Time	Multiplier (min)	0.5 (0.15)	1 (0.3)	2 (0.6)	Oven drying times for anode were calculated based on the energy needed to remove a typical solvent composition. The "base value" corresponds to a dwell time of 0.3 min. Assumed constant speed, increased oven length.
Gore Cathode Oven Dwell Time	Multiplier (min)	0.5 (0.3)	1 (0.6)	2 (1.2)	Oven drying times for cathode were calculated based on the energy needed to remove a typical solvent composition. The "base value" corresponds to a dwell time of 0.6 min. Assumed constant speed, increased oven length.
2017 Gore Direct-Coat MEA Cost at 500,000 systems per year (\$/m²)				\$92.35	

page 22

STRATEGIC ANALYSIS®

